2nd of 3 files

Chapters 2 to 4

High Pressure Diffraction Studies of Gallosilicate Natrolite: Applications to Pressure-Induced Cation Trapping

By
Gemma Louise Hill
(nee Little)

A thesis submitted to
The University of Birmingham
For the degree of
DOCTOR OF PHILOSOPHY (PhD)

School of Chemistry
The University of Birmingham
2010

CHAPTER TWO

Experimental

2.1 Diffraction Theory

Diffraction is observed when a propagating wave encounters an obstacle. If the obstacle has an opening similar to the wavelength of the incident wave, then the wave passes through but spreads out once past this opening. Crystalline solids can cause diffraction of electromagnetic radiation. They are characterised by a regularly repeating structural unit (a unit cell). This repetition acts to supply an array of closely spaced 'small openings' for electromagnetic radiation to pass through and be diffracted; so a crystal will diffract radiation of a wavelength similar to that of the atomic separation/atomic planes. Generally this distance is equivalent to wavelengths in the range of X-rays, neutrons and electron radiation. The resulting diffraction pattern caused by interaction with a unit cell gives information about the spatial arrangement, the symmetry, atomic positions and atomic occupancy within the unit cell. It is this principle of diffraction that is used to characterise crystalline solids and is considered one of the most powerful tools in solid state chemistry.

Within a powder diffraction pattern there is both position/direction and intensity of radiation. The position of the diffracted wave depends upon several factors including the unit cell size, shape and symmetry. The intensity of diffracted radiation is relative to both the nature and occupancy of the atoms within the unit cell. Bragg's law is used to describe the direction of diffracted radiation caused by interaction with a crystalline solid.

2.1.1 Bragg's Law

Bragg's law models the unit cell in terms of a series of semi-transparent planes. The atoms within the unit cell occupy these planes and act to 'reflect' an incidence beam of radiation.[1]

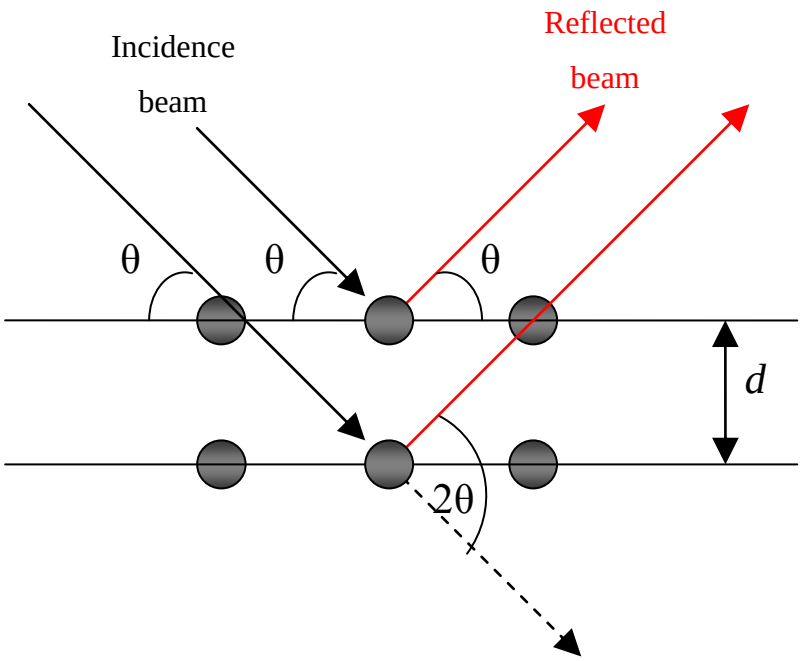

Figure 1: A schematic of the Bragg reflection of an incidence beam of radiation by crystal planes. d=the distance between crystal planes, θ=the angle of incidence. Atoms are shown as grey spheres.

Bragg's law describes the interference of waves of radiation reflected from these planes. Wave interference creates a diffraction pattern. The interference can be constructive or destructive. For the waves to be constructive they must be in phase, i.e. the path difference is equal to an integer value of the wavelength. This condition is described by Bragg's law, shown in Equation 1, which shows the dependence of diffraction upon plane separation, *d*. At an angle of incidence other than that described by the Bragg condition, destructive interference occurs.

$$n\lambda = 2d\sin\theta$$

Equation 1: Bragg's law, n=integer, λ=wavelength and θ=angle of incidence/reflection.[1]

2.1.2 Diffraction of X-rays and Neutrons

Diffraction techniques are used throughout this thesis as a method of structure elucidation. Both X-ray and neutron diffraction experiments were performed in order to gain detailed complementary structural information. The following sections describe the production and diffraction of both X-ray and neutron radiation, used to give a powder diffraction pattern. There are a number of excellent publications and reviews (relevant to this work), providing a comprehensive introduction to X-ray[2,3,4] and neutron diffraction.[5] In particular, Cheetham[6] gives a well summarised overview of powder diffraction techniques as does Langford and Louër in their more detailed review.[7]

2.1.2.1 X-ray Use in Diffraction

X-rays interaction with the electron clouds of the atoms within a solid. Typically, X-rays used in diffraction experiments are produced in two ways: via an X-ray tube or a synchrotron.

Synchrotron X-rays are generated when charged particles are forced to move in a circular path at ultra-relativistic speeds (near the speed of light). The moving particles emit high energy photons in a forward tangent to the circular path of travel, typically in the range of 0.1-150 KeV. The emitted photons are of variable wavelength ranging from infra-red to X-ray radiation. The brightness of the radiation allows for detailed structural information to be collected in short exposure times. Synchrotron X-rays are both highly collimated and highly polarised. These factors combined give a powerful technique for crystallographic study. This technique is excellent for structure elucidation but is very costly and requires trips to a synchrotron facility.

X-rays can also be produced via an X-ray tube. These X-rays do not have the brightness of synchrotron radiation, but offer a method of X-ray diffraction which can be used in a standard laboratory. X-rays are produced by collision of thermionically emitted electrons from a cathode tube, with target anode metals (copper, molybdenum or tungsten). The diffractometer used in this thesis emits X-rays via collision with a copper target. The electrons travel through a vacuum and collide with copper, causing ionisation of the metal. An electron from an outer orbital of the copper atom will decrease in energy to fill the vacancy created by ionisation. The difference in energy levels of this transition is emitted as X-ray radiation. For copper, movement from the 2*p* orbital to fill the vacancy in the 1s orbital is the transition responsible for X-ray production. Two wavelengths of X-ray radiation are emitted (due to the two spin states of the 2*p* orbital). These two emissions are $K\alpha_1$ and $K\alpha_2$. One wavelength ($K\alpha_2$) is directed away from the sample via a monochrometer to give X-ray radiation of a single wavelength (monochromatic).

In this thesis, powder (rather than single crystal) diffraction is used to resolve sample structure. This technique involves a monochromatic beam of X-rays striking a powdered sample. The powdered sample contains particles which are randomly orientated so that there is always orientation at the Bragg angle (with respect to the incidence beam). Diffraction of the X-rays by a randomly orientated sample produces cones of diffracted X-ray radiation, one cone for each lattice plane. These cones are collected on an image plate or by a position sensitive detector. An image of these cones appears as a series of concentric circles about a central beam stop point. The diameter of this series of rings corresponds to a diffraction angle of 4θ, so that a cross section from the centre to the outer ring corresponds to 2θ.

The diffraction pattern resulting from interaction with a powdered sample gives information about the lattice size, symmetry, space-group, atomic positions and atomic occupancies. The position of the observed diffraction rings is dependant upon lattice size, symmetry and space-group. The intensity of radiation of each diffraction ring (I_x) is dependant upon a series of factors, as shown in Equation 2.

$$I_x = K_x F_x^{\,2} m_x A_x L_x P_x$$

$\boldsymbol{I_x}$=Intensity of the diffracted X-ray.

$\boldsymbol{K_x}$=Proportionality constant.

$\boldsymbol{F_x}$=Structure factor (Sum of scattering from atoms within the cell).

$\boldsymbol{m_x}$=multiplicity of lattice planes within the cell.

$\boldsymbol{A_x}$=absorption factor (absorption of X-rays by the sample).

$\boldsymbol{L_x}$=Lorentz factor (variation in Bragg reflection at a given angle).

$\boldsymbol{P_x}$=Polarisation factor (polarity of the incidence beam).

Equation 2: Formula to describe the factors affecting the intensity of diffracted X-rays by a powdered sample.[4]

2.2.2.2 Neutron Use in Diffraction

Neutrons can also be diffracted by crystalline solids to give structural information. Neutrons interact with the nuclei of the atoms rather than the electron clouds. Typically, neutrons used in diffraction experiments are produced via a spallation or reactor source. In this work, only the spallation source at the ISIS neutron source, Oxfordshire was used.

Neutrons from a spallation source are created by accelerating protons in a synchrotron by the use of a manipulated magnetic field. H^- ions enter the synchrotron; thin alumina foil strips away the electrons leaving a beam of protons which collide with a heavy tungsten metal target. The tungsten atoms slough off neutrons (spallation). The neutrons are slowed to speeds useful for condensed matter research by an array of hydrogenous moderators around the target.[8]

In Time-of-Flight (TOF) neutron diffraction, the neutrons travel at different velocities with different wavelengths. The Bragg angle is fixed and the wavelength varies. The

neutron time-of-flight (from creation to the detector) is measured and from these velocities and hence wavelengths are calculated (Equation 3).

$$\lambda = \frac{h}{mv}$$

λ=wavelength

h=Planck's constant

m=mass

v=velocity

Equation 3: De Broglie relationship.

The intensity of diffracted neutrons can be given as I_n (Equation 4). I_n has contributing factors analogous to those for X-rays. However, polarisation factors are not needed for neutron diffraction as the radiation is polarised. Scattering factors become particularly significant in neutron scattering as the scattering is not dependant upon atomic number, but varies for each atom as a consequence of the differing atomic nuclei.

$$I_n = K_n F_n^{\,2} m_n A_n L_n$$

$\boldsymbol{I_n}$=Intensity of the diffracted neutron radiation.

$\boldsymbol{K_n}$=Proportionality constant.

$\boldsymbol{F_n}$=Structure factor (Sum of scattering from atoms within the cell).

$\boldsymbol{M_n}$=multiplicity of lattice planes within the cell.

$\boldsymbol{A_n}$=absorption factor (absorption by the sample).

$\boldsymbol{L_n}$=Lorentz factor (variation in Bragg reflection at a given angle).

Equation 4: Formula to describe the factors affecting the intensity of diffracted neutrons by a powdered sample.[4]

Neutron diffraction is a form of elastic scattering. The neutrons exiting the experiment have the same energy as the incident neutrons. The technique is similar to X-ray diffraction, giving complementary information via a different type of radiation.

Neutron and X-ray diffraction differ in their interaction with the sample. In X-ray diffraction, interaction is with the electron cloud of the atoms within the sample. So, that X-ray diffraction intensity is proportional to atomic number. Neutrons interact directly with the nucleus of the atoms in the sample. Different atoms and isotopes interact differently i.e. have different scattering factors which are not proportional to atomic number. For example, Vanadium (large atomic number), will scatter X-rays strongly but shows very little scattering of neutrons. As a consequence of this vanadium is used as sample housing during neutron experiments.

Hydrogen Scattering

Because neutrons interact with the nucleus, neutron diffraction can be used to study atoms of low atomic weight (e.g. H), which would be unresolved in powder X-ray studies. Nuclei ^{1}H and ^{2}H=D are strongly neutron scattering. This means that the position of hydrogen in a crystal structure can be accurately determined. The scattering by H-nuclei has a large inelastic component and this creates a large continuous background. The elastic pattern typically consists of sharp peaks, but these are drowned out by the large inelastic background scattering. Consequently, hydrogen within the sample is replaced by deuterium. The positioning within the crystalline structure remains the same but the large background issue is negated via this substitution.

2.2 Synthesis, Preparation and Characterisation of Materials

2.2.1 Hydrothermal Synthesis

All zeolite synthesis reactions and some ion exchange reactions were carried out hydrothermally using stainless steel autoclaves lined with a Teflon™ reaction vessel. Due to the nature of hydrothermal synthesis a bursting disc is employed to allow release of extreme pressures by the controlled expansion of the Teflon™ liners (although Teflon™ lined auto claves can often withstand pressures of up to 150 bar and temperatures of up to 270°C). See Figure 2 for a schematic of the Teflon™ lined autoclave used.

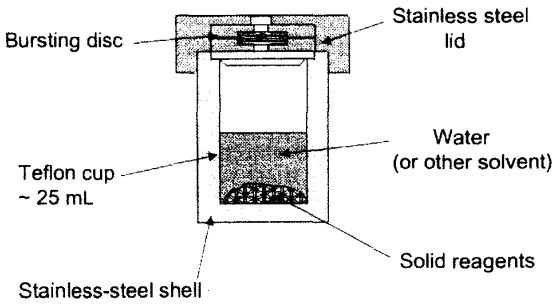

Figure 2: Schematic of a Teflon™ lined autoclave used in hydrothermal synthesis.[9]

Na-GaSi-NAT was synthesised hydrothermally from adaptations of the method reported by Hong.[10,11,12,13] A batch composition of 6.0 Na_2O : 1.0 Ga_2O_3 : 10.0 SiO_2 : 150 H_2O was used. Using this ratio Hong has reported the formation of both tetragonal and orthorhombic pure crystal systems. The temperature and length of heating dictate the identity of the crystal system.

2.2.1.1 Orthorhombic Na-Ga-Si-NAT

Synthesis of orthorhombic Ga-NAT was performed in 125 ml Teflon lined autoclaves. A mixture of 3.75g of $Ga_2O_{3(S)}$, 19.17g of NaOH(*aq)* (50wt% in H_2O) and 24.29g of deionised water was prepared. This clear and colourless solution was heated at 100°C for 24 hours, after which 29.99g of colloidal silica (*Ludox* AS 40) was added. The mixture (a gel of low viscosity), was stirred for 24 hours to give a clear colourless viscous solution. This solution was placed in a Teflon™ lined autoclave and heated at 150°C for 14 days. The product of this reaction was difficult to recover. The colourless, glass like solid, very firmly coated the Teflon™ liner. Consequently, a scalpel was needed to remove the sample. Although contaminating the sample with Teflon™ shavings, this procedure enabled most of the solid product to be recovered. The sample was ground under deionised water and the Teflon™ shavings removed manually to give ~4.5g of pure orthorhombic Na-GaSi-NAT. The product was filtered and washed with deionised water and dried in a vacuum desiccator for 48 hours.

2.2.1.2 Tetragonal Na-Ga-Si-NAT

Synthesis of tetragonal Ga-NAT was performed in 45 ml Teflon™ lined autoclaves. A mixture of 1.39g of Ga_2O_3, 7.11g of NaOH(*aq)* (50wt% in H_2O) and 8.98g of deionised water was prepared. This clear and colourless solution was heated at 100°C for 24 hours, after which 11.11g of colloidal silica (*Ludox* AS 40) was added. The mixture (a gel of low viscosity), was stirred for 24 hours to give a clear colourless viscous solution. This solution was placed in a Teflon™ lined autoclave and heated at 100°C for 3 days. The product was filtered and washed with deionised water and dried in a vacuum desiccator for 48 hours.

Characterisation of the two gallosilicate samples (following synthesis or ion exchange), was assessed via powder X-ray diffraction and SEM EDX micro-X-ray analysis. These two analytical techniques warrant in-depth discussion, and are therefore covered in independent sections within this chapter. More detailed crystallographic characterisation was performed via synchrotron X-ray and neutron diffraction experiments. Both of these methods are also discussed in independent sections within this chapter. The characterisation and preparation techniques discussed in this chapter also include: deuteration methods; Fourier transform infra-red spectroscopy; thermogravimetric analysis and Solid state NMR.

2.2.2 Deuteration

For neutron diffraction studies, sample deuteration is required to avoid adverse hydrogen scattering effects. Two deuteration techniques were employed: vacuum dehydration followed by exposure to D_2O and hydrothermal exchange in a D_2O medium. In each case the deuterated sample was collected using suction filtration and washed with D_2O (analytical grade, Aldrich). Measurement of the crystallinity and the deuteration level of the sample were performed using powder XRD and FTIR spectroscopy respectively.

2.2.2.1 Vacuum Deuteration

Using a vacuum line the sample (~1g), was heated to between 170-250°C over 1-5 hours to ensure dehydration. The dehydrated sample was then exposed to a D_2O (analytical grade, Aldrich) atmosphere for 12 hours. The sample, sealed from the atmosphere while handling, was analysed via FTIR spectroscopy.

2.2.2.2 Hydrothermal Deuteration

The sample (~0.1-1g) was placed in a Teflon^{TM} lined autoclave, 10ml of D_2O (analytical grade, Aldrich) was added and the suspension heated to 100°C over 24 hours. The autoclave was allowed to cool to room temperature while still sealed. Recovery of the sample was performed in a glove bag under an argon atmosphere to prevent exposure to atmospheric moisture. The sample was filtered, washed with D_2O and allowed to dry via suction filtration. The recovered sample was sealed in a glass tube under a stream of argon. All sample recovery steps were performed within the argon atmosphere. The extent of deuteration was monitored using FTIR spectroscopy and Mass spectroscopy. Hydrothermally deuterated samples were used in powder neutron diffraction experiments.

2.2.3 FTIR Spectroscopy

Assessment of the D_2O/H_2O content of samples following deuteration was performed using FTIR spectroscopy. Samples were initially ground together with KBr to form a disc, or latterly used directly in a diamond reflectance insert. In each case spectra in the region of $4000cm^{-1}$-$1000cm^{-1}$ were recorded. FTIR spectroscopy can be used to measure H_2O and D_2O content by comparison of the relative heights of the peaks at ~$3500cm^{-1}$ and ~$2500cm^{-1}$ for the O-H and O-D stretches, respectively.

When initially preparing the samples for FTIR spectroscopy, KBr disks were used but caused inaccurate results. Rapid atmospheric back-exchange occurs during grinding and handling. The hydroscopic nature of KBr also increases this atmospheric exchange. To improve accuracy, various adaptations to sample preparation were applied. These include: heating of KBr to remove trace amounts of water, addition of a vacuum pump to the dye press to remove trace water and transportation of equipment and substances in drying desiccators to reduce atmospheric moisture contamination. By employing these adaptations the H_2O/D_2O ratio decreased, but there was still more H_2O measured than expected.

Using an FTIR spectrometer with a diamond reflectance insert made it possible to record the relative D_2O and H_2O peaks but without the need for preparing KBr disks. A *Shimadzu* FTIR attenuated total reflectance (ATR) spectrometer was used. The sample was placed between the diamond prism contacts and the spectra collected within a matter of seconds. Therefore, the atmospheric exposure time was dramatically reduced when compared to the previous KBr disc method. Figure 3 shows the rapid exchange which occurs when deuterated samples are exposed to atmospheric moisture, an indication of the necessity of careful sample handling.

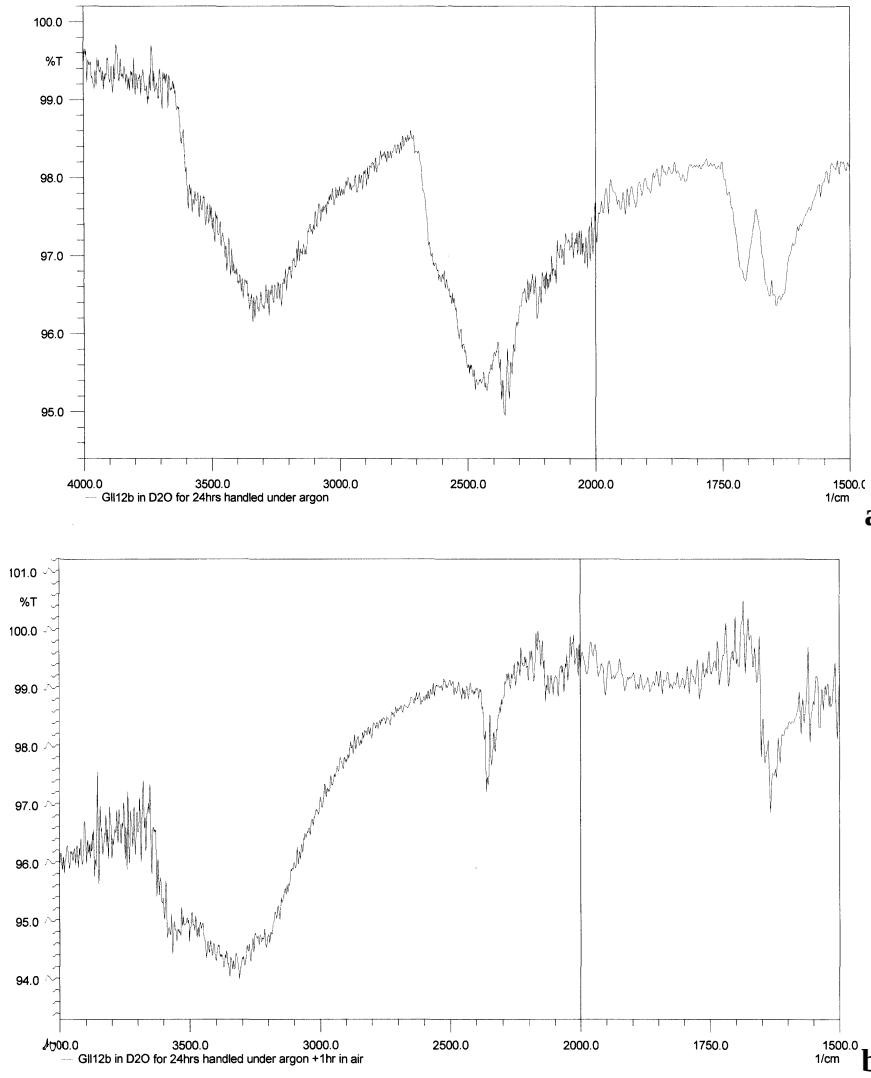

Figure 3: a) Na-Ga-NAT heated in D_2O at 100°C for 24 hrs, handled under argon b) Na-Ga-NAT heated in D_2O at 100°C for 24 hrs, handled under argon then exposed to atmospheric moisture for 1hr.

2.2.4 NMR

All NMR experiments (^{29}Si and ^{71}Ga) were performed by Professor Mark Smith[14] at the University of Warwick. ^{29}Si magic angle spinning (MAS) NMR spectra were collected on a Varian/Chemagnetics InfinityPlus, capable of 8.45 Tesla; using a 9.5mm rotor probe at 4 kHz. ^{71}Ga spin echo MAS NMR spectra were collected with a 9.5mm rotor probe at 20 kHz.

2.2.5 TGA

Thermogravimetric analysis of the gallosilicate natrolite samples allowed quantitative study of the mass loss in air as temperature is increased. A starting mass of sample (typically 15 mg), was accurately recorded before the application of temperature. The sample (within a small alumina boat), was loaded onto a fine balance within a *Rheometric Scientific STA 1500 Thermogravimetric analyser* (TGA). Temperature was increased from ambient to 1000°C at 5°C min^{-1}. Temperature and weight in air were recorded throughout. Thermogravimetric experiments were performed on both the orthorhombic and tetragonal gallosilicate materials. These experiments were performed in order to assess the water content (specifically the inner-pore water content), of the samples.

2.3 Diffraction Instrumentation and Equipment

2.3.1 Bruker D5000

A *Bruker D5000* X-ray diffractometer was used for general sample measurements. Following synthesis or ion exchange, the resultant structures were monitored using these instruments. All measurements were at ambient temperature and pressure. Samples were ground using a pestle and mortar, mounted on Scotch^{TM} 'Magic Tape', fixed to an aluminium X-ray diffraction disc and positioned within the sample housing so that the X-ray beam passes through the sample. The mounting 'magic tape' gives negligible scattering that only becomes visible if the sample size or crystallinity is extremely low. The mounting Aluminium disc rotates about a fixed position throughout data collection.

The diffractometer produces Cu radiation ($K\alpha_1$ and $K\alpha_2$). $K\alpha_2$ is directed away from the sample and the beam focused via a monochrometer to give a monochromatic incidence beam of $K\alpha_1$ X-rays. The wavelength of emitted radiation for the *Bruker D5000 is* Cu $K\alpha_1$ λ=1.5406Å.

Data were collected via a PSD (position sensitive detector). The detector rotates about the sample and produces a diffraction pattern electronically in increments of ~0.02°. A 1-dimesional data 'slice' through the diffraction rings produces a powder X-ray diffraction pattern. Powder patterns are formatted, translated, indexed and manipulated using *Bruker EVA* software. Crystal structures were matched to reports from the *Inorganic Crystal Structure Database* (ICSD), accessed via the *EVA* software.

2.3.2 High Pressure Diffraction

High pressure diffraction experiments fall into two categories: neutron diffraction and synchrotron X-ray diffraction. For each method a different form of preparation and sample housing is required.

2.3.2.1 Synchrotron X-ray Diffraction

For all high pressure synchrotron X-ray diffraction experiments, samples were prepared and loaded into a diamond anvil cell (DAC) as described below. Ambient pressure experiments were performed using mounting tape or a rotating glass capillary tube. Synchrotron X-ray diffraction experiments were performed at two laboratories: beamline X7a, NSLS, Brookhaven NY and beamline 9.5HPT, Daresbury Laboratory, UK.

Diamond Anvil Cell (DAC)

High pressure experiments were performed using a diamond anvil cell (DAC) as seen in Figure 4. The hard, stable diamond surface and the nature of the DAC apparatus enable the safe generation of pressures up to 40-50 GPa.[15,16] In these synchrotron X-ray diffraction experiments pressures up to 6 GPa were used.

Diamond anvil cells are being used in an increasing amount of high pressure diffraction studies as they offer a method which requires little modification to the diffractometer/beamline apparatus. Jayaraman's review provides a detailed look at the DAC and the modifications needed for its application in a variety of other techniques including high temperature experiments, solid-state synthesis and optical measurements.[17]

Stainless steel cell clamped around diamond-gasket complex.

Sample loaded diamond-gasket complex

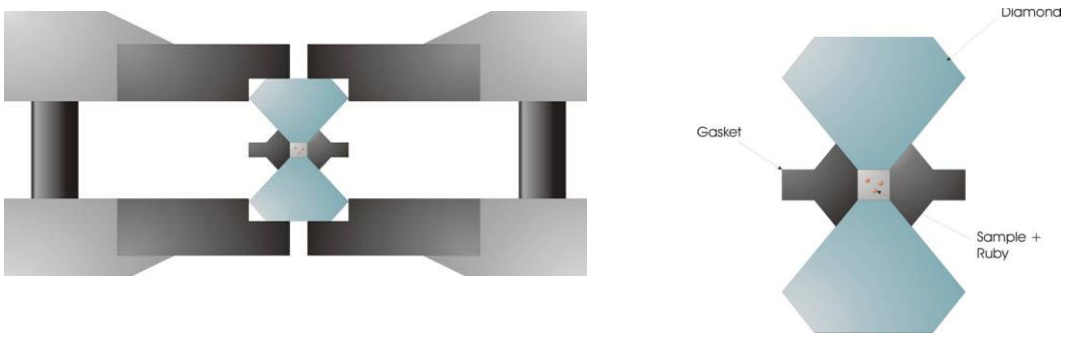

Figure 4: Schematic of a diamond anvil cell (DAC). Manual tightening of the cell generates measurable pressure between the two diamond surfaces.

The DAC used in these experiments is a modified version of the Merril-Bassett design.[18] The DAC comprises a stainless steel body with the diamonds glued onto a beryllium base and held with the flat tops parallel within the body. Diamonds are ideal because of their hardness and optical transparency. Beryllium is used for its X-ray transparency. The anvil can be manually tightened to generate pressures between the two diamond faces. Between the diamond faces, a gasket (stainless steel or beryllium) contains the sample, pressure medium and a few ruby chips. Gaskets are indented by the diamond faces then a hole is burnt out via spark erosion. A typical gasket aperture is 200μm, this allows for approximately $3x10^{-6}cm^3$ of sample. This is considerably less than that used in neutron diffraction experiments as the high flux beam does not require as much sample as neutron work. Since P=F/A, a smaller sample means we require less force to generate the desired pressures. Hence, a small DAC apparatus can generate the required pressure via manual tightening as opposed to the much larger forces required when using a Paris-Edinburgh cell in neutron diffraction work. With a small, easy to handle, load and pressurise apparatus we can prepare samples much quicker. This factor, as well as the short data collection times (typically 5 min), means that a greater number of data points with finer pressure increments can be collected. As a consequence, the use of the DAC in synchrotron X-ray diffraction experiments allowed for a more detailed study of the superhydration region of the gallosilicate natrolites.

The DAC was loaded under a microscope, with a small amount of powdered sample (typically ~1 mg), a few small ruby chips (used as a pressure marker) and a drop of

pressure medium MeOH:EtOH:H_2O (16:3:1). The anvil was tightened manually to generate internal pressure. The pressure exerted upon the sample was measured using laser-induced ruby fluorescence. The wavelength of the emitted ruby fluorescence is directly proportional to pressure. The R_1 emission line appears at 14,400cm^{-1} at ambient pressure with a shift of -7.57cm^{-1} GPa^{-1} upon pressure application. So, by measuring this wavelength it is possible to accurately determine the pressure within the cell, making ruby an ideal pressure marker. Fluorescence was induced by an argon-yttrium laser. The emission shift was detected via a laser spectrometer and the pressure calculated using the shift stated above.

X7a

The X7a beamline at NSLS Brookhaven, NY is set up to enable high pressure synchrotron X-ray diffraction experiments by the use of a diamond anvil cell (DAC). The primary white beam is focused in the horizontal plane via an asymmetrically cut Si monochrometer. This gives micro-focused monochromatic radiation (~200μm, ~0.7Å).[19,20] Slits were used to further tailor the beam size in the vertical (100-200 μm), dependant upon the DAC gasket culet size. The DAC was positioned (following a 10 minute pressure equilibration interval), using a telescope and mounting plate, both of which were position adjustable in 3 planes. A gas-proportional position sensitive detector[21] was used in data acquisition. The PSD was stepped at 0.25° steps in the angular range 5-30° with counting times of 60-120 seconds per step. The wavelength used in the gallosilicate experiments was 0.647390 Å

9.5HPT

The 9.5HPT beamline (Daresbury Laboratory, UK) also allows for high pressure synchrotron X-ray diffraction experiments via use of a DAC. The primary white beam is focused in the horizontal plane via a cleaved Si (110) monochromator crystal. This gives a focused monochromatic X-ray beam of ~0.5 Å.[22] The DAC was positioned, following a 10 minute pressure equilibration interval. Accurate positioning was achieved by lining up the mounting plate (position adjustable in 3 planes), with a burn spot from the incidence beam (performed upon optically sensitive paper). Data was collected upon a MAR345 image plate. Fit2d software was available to integrate data

ready for Rietveld analysis. Data acquisition time was 300 seconds. The wavelength used for the gallosilicate experiments was 0.44397 Å.

Prior to integration, the software allows a full view of the image plate showing the diffraction rings. A unique application within Fit2d allows for selective 'masking' of areas anywhere on the imaging plate. This technique improves the quality of data collected by careful elimination of diamond reflections, ruby peaks and unwanted pattern spotting. In this way more accurate peak intensities are produced than the standard PSD collection and integration method. Chapter 5 details the improvements in data as a result of this method.

The loading of the DAC is unchanged from that described in the previous section. However a new method of sample preparation prior to loading was implemented during these experiments. Previously the dry sample was extensively ground using a pestle and mortar. A new method was implemented to reduce particle size in order to gain better structural averaging during powder diffraction. Samples were extensively ground under the pressure-medium (MeOH:EtOH:H_2O (16:3:1), the resulting suspension of very fine particles was removed from the bulk sample using a pipette, the suspension was allowed to dry for several hours and then loaded into the DAC. Consequently a much finer powder was achieved which was otherwise unobtainable, even with hours of dry pestle and mortar grinding.

2.3.2.2 Neutron Diffraction

Pearl

Neutron diffraction data was collected using the high pressure facility HiPr on the PEARL beam line at the ISIS facility (Rutherford Appleton Laboratory, Didcot, UK). Pearl uses a high-flux, medium-resolution diffractometer and is optimised for use with the Paris-Edinburgh cell, which is described in the following section. Until a decade ago, high-pressure neutron diffraction studies were confined to the pressure range 0-3 GPa. Use of the Paris-Edinburgh cell has extended this range by almost a full order of magnitude up to ~25 GPa.[23]

Ambient pressure patterns were collected by loading the sample into a sealed vanadium can (6mm can, sample loaded under a stream of nitrogen). Data were collected over 30 minutes. High pressure experiments required the use of a V3 Paris-Edinburgh cell, as described in the next section. External pressure was applied via a piston. Applied pressures were 7, 12, 22 and 26 tonnes, respectively. The internal pressure was calculated using a lead pressure marker. The lattice parameters of lead were refined during Rietveld analysis and the pressure calculated from a known equation of state. Data acquisition time for high pressure runs were 10 hours for each pressure increment.

Refinements of the data included a vanadium phase (for ambient pressure experiments), or Ni, WC and Pb phases for (high pressure experiments).

Paris-Edinburgh Cell

The Paris-Edinburgh cell is a relatively large, strong tungsten carbide anvil which is capable of generating high pressures while still retaining the large sample sizes needed when using a low flux neutron spallation source. The low flux beam used in neutron diffraction experiments on the PEARL beamline, means that sample sizes need to be in the region of 0.55 cm^3 (considerably larger than in a DAC ($3x10^{-6}cm^3$)). As a result of the larger sample size, a greater force is required to generate high pressures. Use of the Paris-Edinburgh cell allows for these large forces by employing a large tungsten carbide anvil. Figure 5 shows a photograph which clearly shows how large the anvil is when compared with the people standing in the background.

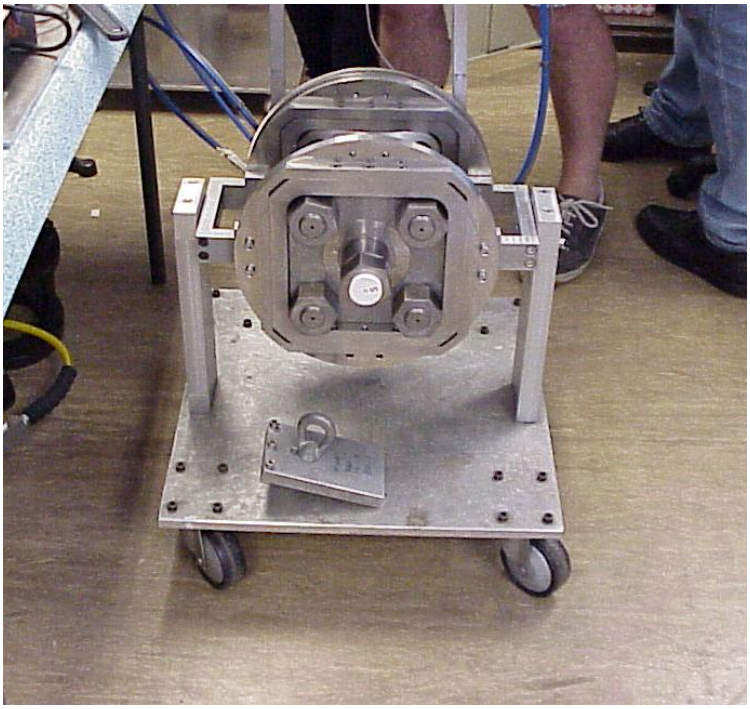

Figure 5: Photograph of the fully assembled Paris-Edinburgh cell, showing the tungsten carbide anvil resting horizontally on support brackets.

The ground, deuterated sample was loaded into the V3 Paris-Edinburgh cell (a single tungsten carbide (Ni binder) anvil, with capsule gasket). Sample loading was performed under a stream of nitrogen (needed to prevent exposure to atmospheric moisture). Figure 6 shows loading of the sample into the gasket sample chamber. A small piece of lead was added as a pressure marker. A few drops of pressure transmitting fluid (deuterated MeOD/D_2O 1:1) were added to the cell which was then immediately sealed. A schematic of the fully assembled sealed cell is shown in Figure 7. Pressure was generated via an external, calibrated piston pump once the cell has been fully assembled.

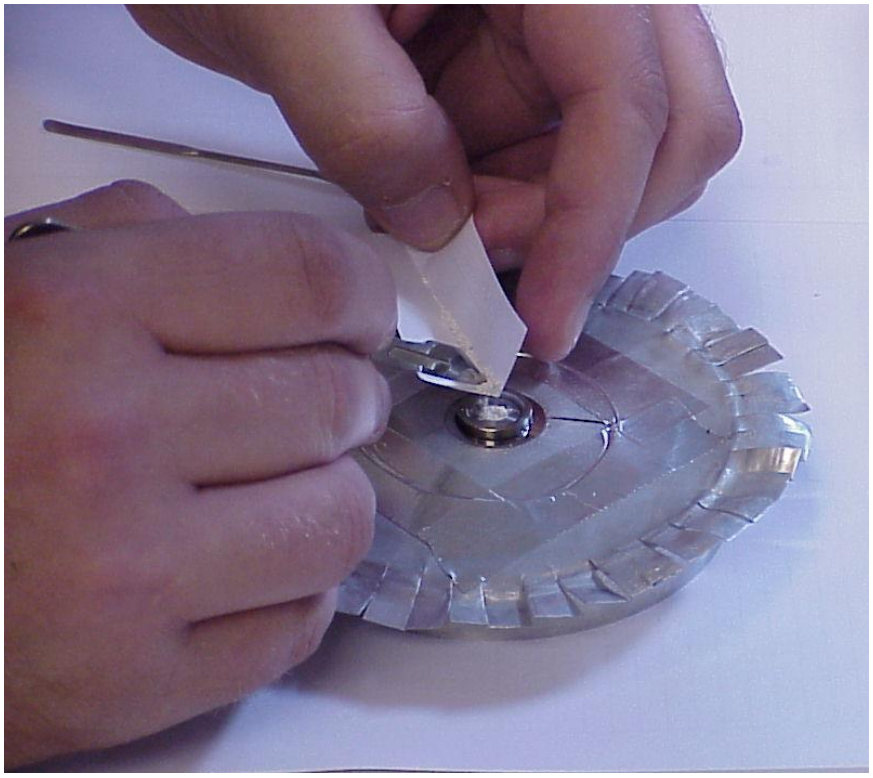

Figure 6: Loading of the sample into the capsule gasket aperture ready for assembly within the V3 Paris-Edinburgh cell.

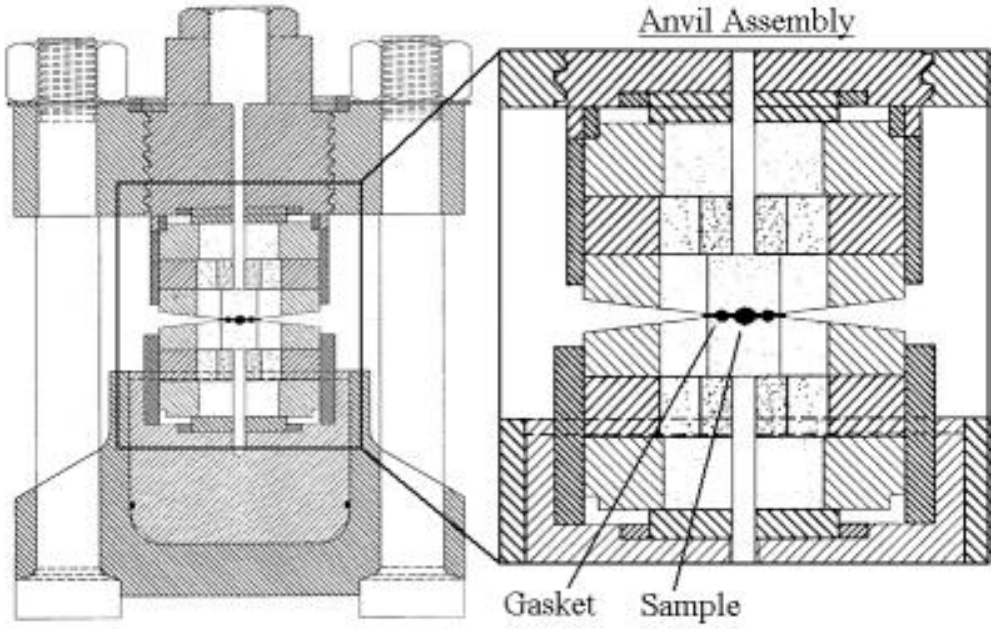

Figure 7: Cross-sectional schematic of a fully assembled V3 Paris-Edinburgh Cell.[24]

2.3.3 Ambient Pressure High Resolution Neutron Diffraction, HRPD.

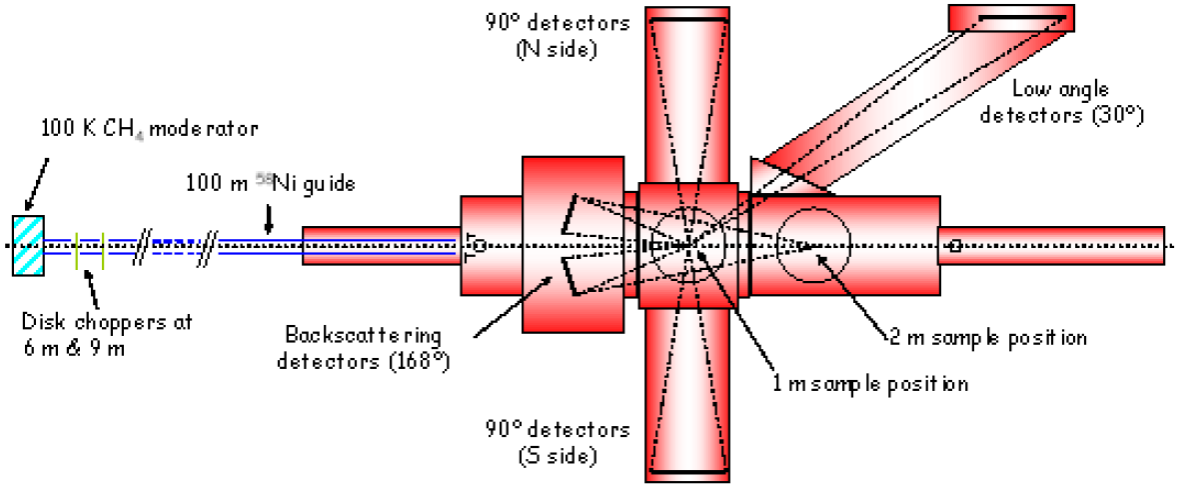

Figure 8: Schematic of the ISIS HRPD detector configuration.[25]

The HRPD beamline is almost 100m from the ISIS target. The time of flight of the neutrons is increased by increasing the flight path, so that the timing uncertainty ΔT and the flight path uncertainty ΔL, is decreased (both contribute to increasing the resolution). The resolution of a diffractometer (Δd/d) is given by Equation 5.25

$$\Delta d/d = \left[\Delta\theta^2 \cot^2\theta + \left(\Delta t/t\right)^2 + \left(\Delta L/L\right)^2 \right]^{1/2}$$

Equation 5: The resolution of a diffractometer (Δd/d), showing the dependence of timing uncertainty and flight path uncertainty (Δt and ΔL respectively).

The HRPD station has three detector banks, 168°, 90° and 30°. Scattering at low angles allows for long *d*-spacing, but has the lowest resolution. The backscattering bank (168°), has the highest resolution at $\Delta d/d$=4-5 x 10^{-4}. Each bank has its own

merits, as summarised in Table 1. Dependent upon sample positioning, it is possible to collect data from all three banks simultaneously, thereby creating the best possible crystallographic picture of the studied sample.

Table 1: HRPD detector bank details.[25]

	Backscattering (168°)	**90°**	**Low Angle (30°)**
Fixed scattering angle	160<2θ<176	87<2θ<93	28<2θ<32
d-spacing range (30-230 ms)	~0.6-4.6Å	~0.9 6-6 Å	~2.2-16.5 Å
$\Delta d/d$	4-5 x 10^{-4}	2 x 10^{-3}	2 x 10^{-2}

In the experiments performed in this thesis, data were collected from all three banks simultaneously for each of the gallosilicate natrolites. The deuterated samples were loaded into a vanadium can (sealed with indium wire). Data acquisition times were ~3-6 hours. All experiments were performed at ambient pressure. Data points were collected over a range of temperatures from 290 K to 20 K.

2.4 Data Analysis

The data collected throughout this thesis typically required structural and compositional analysis. The structure of studied samples was resolved using the Rietveld refinement method (explained in the next section). For the high pressure data only, the refined values were used in an equation of state fitting, via EoSFIT5.2 software. Compositional analysis, primarily performed upon ion exchanged samples, was carried out via electron dispersive X-ray scanning electron microscopy (EDX SEM). The Rietveld method, equation of state calculations and scanning electron microscopy methods are discussed in detail in the sections which follow.

2.4.1 Rietveld

The Rietveld refinement method[26,27] is an incredibly useful technique in resolving crystal structures from diffraction data. The method refines parameters of a specified crystallographic model to fit the observed data. From this a 'real' model for observed data can be gathered form an estimated model. The Rietveld refinement calculations act to minimise the difference between the observed and the calculated pattern. The function which is minimised in a refinement is S_y, the sum of which is over all data points.

$$S_y = \sum_i w_i \left(y_i - y_{ci} \right)^2$$

Equation 6: The function (S_y), minimised in Rietveld refinement. y_i=Observed intensity (ith step), y_{ci}=calculated intensity (ith step), w_i=1/y_i.[28]

Bragg reflections from the sample produce peaks spread over several data points, with the measured intensity at any given position, y_i, the sum of contributions from Bragg peaks and background. The intensities of the calculated model, y_{ci}, are calculated based upon the structure factor $|F_K|^2$ and a background contribution, y_{bi}. The formula for y_{ci} calculation is given below in Equation 7.

$$y_{ci} = s \sum_K L_K \left| F_K \right|^2 \phi \left(2\theta_i - 2\theta_K \right) P_K A + y_{bi}$$

s is the scale factor.

K represents the miller indices, (*hkl*) for a Bragg reflection.

$\boldsymbol{L_K}$ is the Lorentz, polarisation and multiplicity factors.

Φ is the reflection profile function.

$\boldsymbol{P_K}$ is the preferred orientation function.

A is the absorption factor.

$\boldsymbol{F_K}$ is the structure factor for the kth Bragg reflection.

$\boldsymbol{y_{bi}}$ is the background intensity at the ith step.

Equation 7: Formula for the calculation of y_{ci}, the calculated intensities of the Rietveld model.[28]

The least squares minimisation procedure acts to reduce the difference in the observed pattern and the calculated pattern by minimizing the difference between y_i and y_{ci} by a simultaneous refinement of a number of parameters which contribute to y_{ci}. Some of the refinement factors are specific to the sample e.g. lattice parameter, atomic coordinates, fractional site occupancy and temperature factors. Other parameters are dependent upon experimental factors including zero-point corrections, adsorption and background. Due to the complexity of the refinement calculation, having a large number of contributing factors which are not linearly related to the intensities; a starting model must be as accurate as possible. If the starting model significantly differs from the actual model, refinement of the given parameters can cause divergence in the least squares calculation or can lead to a false minimum. In more complex structures (like the gallosilicates studied in this thesis), it becomes necessary to constrain/restrain certain parameters in the hope of avoiding a false minimum.

In the experiments described in this thesis, the stating models were based upon aluminosilicate natrolite[29] for the orthorhombic gallosilicate and tetranatrolite[30] for the tetragonal gallosilicate. For tetragonal gallosilicate, an additional hydrogen position (associated with inner-pore water), was located via a Fourier search and added to the model. For all samples, bond restraints were applied, so that Si-O was restrained at 1.6 Å and Ga-O at 1.8 Å. Where appropriate, H-H and H-O bonds/distances associated with the inner-pore water were restrained at 1.63 Å and 1.0 Å, respectively. The error or weight allocated to the bond constraints was 0.02 Å. Typically, the atomic positions and the temperature factors were constrained so that T atoms, framework oxygen and intrapore species were refined in these groups. Without these restraints/constraints Rietveld refinement of the gallosilicates gave a false minimum with a chemically unsound model.

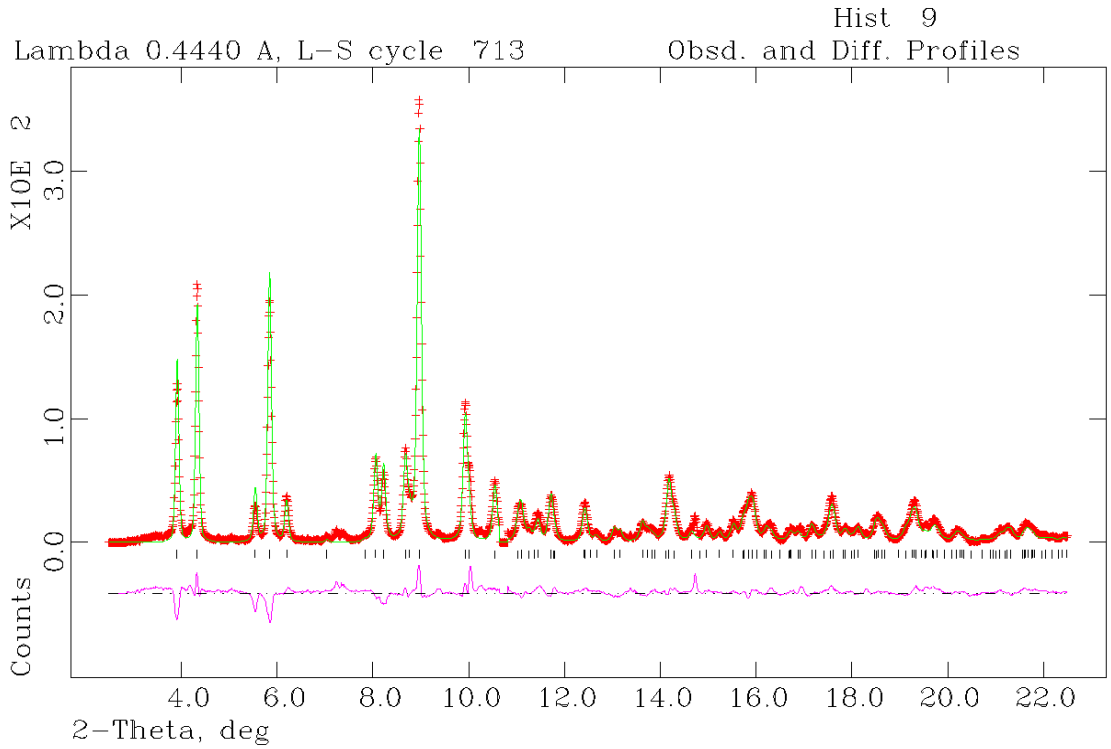

Figure 9: An example of a Rietveld refinement profile plot. The profile plot shows the observed intensity (red), calculated intensity (green), difference curve (purple) and the peaks associated with the phase (back ticks).

Following Rietveld refinement of the model, success of the refinement can be assessed via examination of the difference plots (shown in Figure 9). A minimised, linear (except for noise) difference curve indicates 'a good fit'. A good mathematical indicator is represented in the value, χ^2, where 1 is an exact fit. Certain other numerical values (as described by Young[28]), can be employed to assess the progress of the refinement. These values are known as criteria of fit. The most commonly used are: R_F (often quoted as R_F^2), R_{wp}, and R_p.

$$R_F = \frac{\sum \left| \left(I_K('obs')\right)^{\frac{1}{2}} - \left(I_K(calc)^{\frac{1}{2}} \right) \right|}{\sum \left(I_K('obs')\right)^{\frac{1}{2}}}$$

$$R_{wp} = \left(\frac{\sum w_i \left(y_i(obs) - y_i(calc)\right)^2}{\sum w_i \left(y_i(obs)\right)^2} \right)^{\frac{1}{2}}$$

$$R_p = \frac{\sum \left| y_i(obs) - y_i(calc) \right|}{\sum y_i(obs)}$$

$$\chi^2 = \left(\frac{R_{wp}}{R_e} \right)^2$$

$$R_e = \left(\frac{(N-P)}{\sum w_i y_i(obs)^2} \right)^{\frac{1}{2}}$$

$\boldsymbol{R_F}$ = 'R-structure factor'

$\boldsymbol{R_{wp}}$ = 'R-weighted pattern'

$\boldsymbol{R_p}$ = 'R-pattern'

$\boldsymbol{R_e}$ = 'R-expected'

$\boldsymbol{\chi^2}$ = 'goodness of fit' indicator

$\boldsymbol{I_K}$ = the intensity assigned to the K^{th} Bragg reflection

$\boldsymbol{y_i}$ = Intensity at the i^{th} step

$\boldsymbol{N}$ = number of observables

$\boldsymbol{P}$ = number of refined parameters

Equation 8: The common numerical criteria of fit for Rietveld refinement.

Interpretation of the criteria of fit values should be approached with some caution. It is important to use common sense in their interpretation. It is also important to monitor the visual refinement profile to examine the difference curve.

Experiments performed using different diffraction methods have given significant differences in these criteria of fit. Generally, for the refined neutron diffraction data discussed in chapter 4, the χ^2, R_F^2, R_{wp}, and R_p values are within acceptable range for a good refinement fit. When we look at the refined synchrotron X-ray data from 9.5HPT (discussed in chapter 5), only the R_{wp}, and R_p values are considered reliable indicators. For the 9.5HPT data, the χ^2 values are immediately discounted as the integration using the Fit2d software produces weak peaks on a very large background and no accurate esd's for the intensities. Use of this software affects the value of χ^2, so that values lower than 1 are obtained as R_e is incorrectly calculated. Refinement of the data gave a good visual fit, good R_{wp} and R_p values but higher R_F^2 values (when compared to the values associated with neutron diffraction refinements). For the samples studied in this thesis, there are many broad and overlapping weak peaks at high angle, especially given the medium resolution data produced at 9.5HPT. This means that the integrated intensities can be unreliable and would affect the criteria of fit R_F^2. This is demonstrated in the formula for R_F shown in Equation 8, where the 'observed' Bragg intensity (I_K) is given in quotation marks because it is not observed directly. The I_K values are given by a programmatic allocation of the total observed intensities from both overlapping and individual reflections.[28] So, the value of R_F can be a less reliable indicator of fit due to the assumptions. The R_p and R_{wp} values do not depend upon I_K and so negate this program assumption and are considered a more reliable indicator for the work in this thesis.

Throughout all refinements, Rietveld calculations were performed using the EXPGUI GSAS software suite.[31,32]

2.4.2 EoS

The pressure and volume data obtained from the compression of the gallosilicates and the superhydrated gallosilicates can be used to fit an equation of state (EoS) to each phase. From this the bulk modulus (K) and an extrapolated 'V_0' can be obtained. This is particularly valuable as a value for V_0 of the superhydrated phases cannot be measured experimentally due to the reversibility of the pressure-induced hydration step. The bulk modulus calculated from this fit gives an idea of the compressibility of the sample; which in these works is strongly linked to framework expansion and flexibility.

Equations of state were calculated for all in-situ high pressure diffraction data sequences. These include: powder neutron diffraction (PEARL, ISIS laboratory); synchrotron X-ray diffraction (X7a, NSLS and 9.5HPT, Daresbury). The equations of state were calculated using EoSFIT version 5.2.[33,34] which fits input data to a specified equation of state by least squares refinement. Rietveld refined lattice parameters at specific pressure and a V_0 value were used as input data in the calculation. The equations of state which are most commonly used (and have been used for these works), are the Murnaghan[35] and the Birch-Murnaghan[36] equation of state.

2.4.2.1 The Murnaghan Equation of State

The Murnaghan equation is based upon the assumption that the bulk modulus (K) varies linearly with pressure, so that K_0' is independent of pressure.[34]

$$K = K_0 + K_0' P$$

Integration gives a pressure-volume relationship:

$$V = V_0 \left(1 + \left(\frac{K_0' P}{K_0} \right) \right)^{\frac{-1}{K_0'}}$$

Rearrangement gives:

$$P = \frac{K_0}{K_0'} \left(\left(\frac{V_0}{V} \right)^{K_0'} - 1 \right)$$

This equation of state works well for compressions up to 10% (i.e. V/V_0>0.9). Above this range the Birch-Murnaghan[36] or the Vinet[37] equations of state should be employed. In the data analysed in this thesis, a Murnaghan equation, as well as a second order Burch-Murnaghan equation were used in EoSFIT calculations. Each equation gave the same results, so the mathematically more simplistic of the two equations (the Murnaghan) was employed throughout. Both V_0 and K_0 were treated as variables with K_0' fixed at 4 (similar to a 2nd order Birch equation) unless there was an obvious need for more curvature in the EoS, in that case K_0' was also refined. An example of the reproduced P-V data pattern of fit from an EoSFIT calculation is shown in Figure 10.

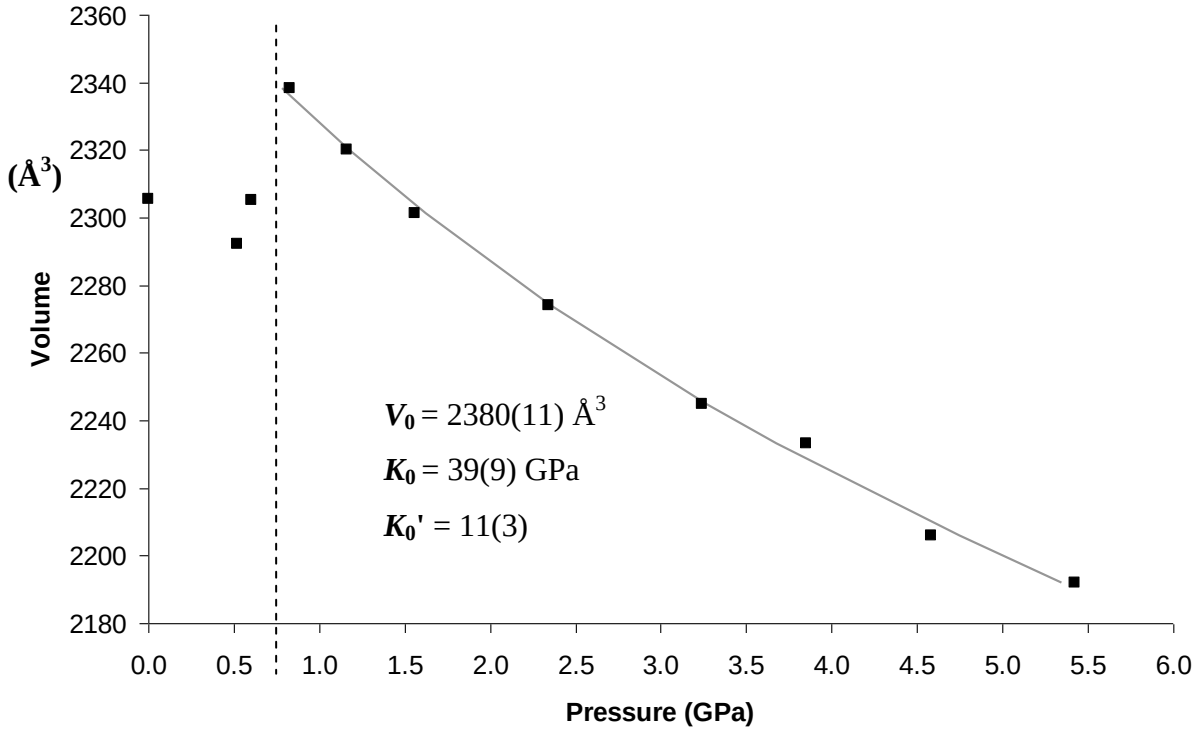

Figure 10: Pressure dependence of the unit cell volume of orthorhombic Ga-NAT (from X7a data collection), used in equation of state fitting. Data points (solid squares) were used to give an equation of state fit (solid grey line) for the high pressure, superhydrated form.

Units

Since equations of state can be re-written in terms of K_0/P and V/V_0, equations of state are presumed to be dimensionless by EoSFIT 5.2. Therefore input of the data requires the units of P and K_0 to be the same (GPa). K_0' is dimensionless and V and V_0 are in terms of $Å^3$, although any volumetric unit can be applied as long as it applies across both values.

2.4.3 SEM

Scanning Electron microscopy has much greater resolution than that gained from standard visible light microscopy. The radiation used is a beam of electrons rather than visible light. The electrons have a wavelength over 100,000 times smaller than that of visible light. This greatly increases the resolution so that magnifications of 1,000,000x can be achieved. In a scanning electron microscope (SEM), electrons are

thermionically emitted from an electron gun containing a tungsten filament cathode. The focused electron beam is deflected in the *x*,*y*-plane so that the surface of the sample is scanned in a raster fashion i.e. scanned in horizontal strips. The beam of electrons interacts energetically with the sample surface, so that there is a reflection of elastically scattered and inelastically scattered electrons and electromagnetic radiation. Detection of these reflections produces an image of the sample surface. Since the SEM has excellent depth of field resolution, a 3-dimensional picture of the sample morphology (surface) can be achieved.[38] An example of a SEM image of a powdered gallosilicate natrolite sample is shown in Figure 11.

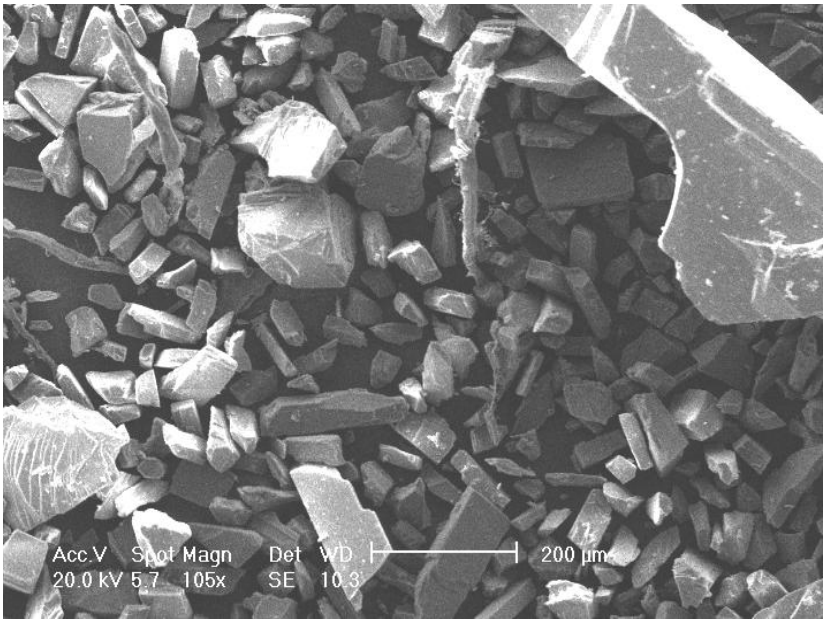

Figure 11: A scanning electron microscope image of gallosilicate natrolite showing well resolved sample morphology.

2.4.3.1 Electron Dispersive X-ray Analysis (EDX).

As well as image generation, an electron beam can be used to perform quantifiable elemental compositional analysis. As the high energy electron beam interacts with the surface atoms, electrons within that atom are excited. The energy difference between the ground state and the excited state can be emitted as X-ray radiation. Since the energy difference between these two states is characteristic

of the atomic structure, specific elements can be identified based upon this emission. This emission is displayed graphically, so that atomic content can be quantified relative to each other. An example of the EDX SEM graphical output and the subsequent compositional values of a Na/Cs ion exchanged aluminosilicate natrolite sample are shown in Figure 12.

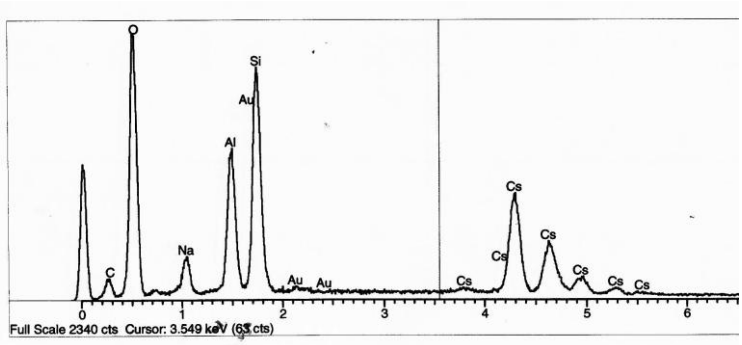

Average stoichiometery:

$Cs_{9.04}Na_{8.28}Al_{14.87}Si_{24.00}O_{77.75}$

Average Cs/Na=1.12

Average Si/Al=1.61

Figure 12: Example of enlarged EDX SEM results following high pressure ion exchange upon Al-NAT, using a saturated CsCl solution.

Figure 13: Image of the Philips XL30 EDX SEM used in sample compositional analysis.[39]

It is important to note that differences in the chemical composition of samples undergoing chemical analysis (e.g. SEM EDX analysis) can affect the quality of the results obtained. These effects are termed matrix effects, where the matrix refers to the components of the sample being studied. It is important to consider these effects where interpreting the quantitative data obtained from SEM EDX analysis. Matrix effects relevant to this work include atomic number and sample absorption. Both these factors affect the relative intensities of the recorded X-ray emissions. The probability of a given X-ray emission reaching the detector to show a recorded intensity is dependent upon atomic number and depth of X-ray emission within the matrix. The larger the atomic number, the more energetic the X-ray emission and the greater the probability of the emission reaching the detector to give a recorded intensity. Since X-ray emissions can occur below the sample surface, some absorption of the emission can occur before exiting the sample.

The results obtained from SEM EDX quantitative analysis (as shown in Figure 12) gave unit cell cation content values which may deviate slightly from expected/ideal composition. This discrepancy can be accounted for by matrix effects, as explained above. Specifically, the cation ratios of partially ion-exchanged samples are subject to matrix effects as a greater proportion of larger cations (i.e. higher atomic number cations) replace Na^+ in the sample.

A Philips SEM XL30 with ISIS EDS was used for each sample analysis, shown in Figure 13. Generally a sample area of 500μm^2-2mm^2 was used in EDX analysis. Samples were prepared by mounting a few grains of the powdered sample on an adhesive carbon pad. The sample was coated in a fine film of gold particles using a vacuum sputter coater. The gold film (nm thick), is required to stop the sample charging during analysis. Because of the insulating nature of zeolites, the sample would charge quickly upon exposure to the electron beam; this distorts the SEM image and gives unusable EDX results.

2.5 Ion Exchange

2.5.1 Ion Exchange at Ambient Pressure

Cadmium ion exchange, under ambient pressure, was performed as reported by Choudhary *et. al*.[40] Samples of Al-NAT and both Ga-NAT forms (~0.5g), were mixed with a saturated solution of $CdSO_4$ (5ml), at 60°C over a period of 50 days with continuous shaking. Each sample was collected using suction filtration and washed with deionised H_2O. Samples were analysed using powder X-ray diffraction and SEM EDX compositional micro X-ray analysis.

2.5.2 Hydrothermal Ion Exchange

A hydrothermal exchange route was also investigated using samples of Na-Ga-NAT and Na-Al-NAT (~1g). Saturated solutions of CsCl, $SrCl_2$, RbCl, and $BaCl_2$ were used in hydrothermal exchange reactions. The suspension was added to a Teflon™ lined autoclave and heated to 100°C over 24 hours. Although not strictly performed at ambient pressure (due to the autogeneous pressures generated when using this method), the low percentage fill of the Teflon™ vessels ensures only low pressures can be generated. This hydrothermal investigation acts as an initial assessment of the cation suitability for later high pressure cation-trapping experiments. Following hydrothermal treatment, the samples were filtered and washed with deionised water and allowed to dry. Samples were analysed using powder X-ray diffraction and SEM EDX compositional micro X-ray analysis.

2.5.3 High Pressure Ion Exchange

By exploitation of the high pressure behaviour of natrolite, high pressure ion exchange experiments were performed with the aim of trapping the exchanged material within the pore upon pressure release. The natrolite materials were brought to superhydration point and exposed to a saturated cation solution. Two techniques were employed: In-situ synchrotron X-ray diffraction using a DAC and a bulk piston-cylinder (Quickpress) high pressure treatment.

2.5.3.1 Ion Exchange Using a DAC

In-situ ion exchange at pressure was performed at the X7a beamline, NSLS Brookhaven, NY using a diamond anvil cell. The DAC (described in an earlier section within this chapter), was loaded with powdered sample and a saturated CsCl solution (rather than the standard pressure medium). A few small ruby chips were added as a pressure marker. The sample (Al-NAT) was exposed to Cs^+ under pressures of 0.41. 0.83, 0.98, 1.03, 1.19, 1.39 and 1.50 GPa. Diffraction patterns were collected at each pressure interval via a position sensitive detector. The Poudrix software was used to predict relative intensity shifts in the diffraction pattern upon ion exchange assuming the Cs sits in the same place as Na.

2.5.3.2 Quick Press Ion Exchange

The second method of high pressure ion exchange is using the Quickpress, a piston cylinder device. The Quickpress offers a method of generating high pressures upon a much larger sample than we could possible hope for when performing in-situ DAC experiments. By increasing the sample size during the ion exchange there is enough sample for back-exchange experiments (to test ion-leaching post-exchange). The method employed in these experiments is unique in its application of pressure upon a customised Teflon™ autoclave (standard practice is to use gold capsules). The use of a cylindrical Teflon™ capsule (6mm x 10mm) means that approximately 50 mg of sample can be used in high pressure exchange.

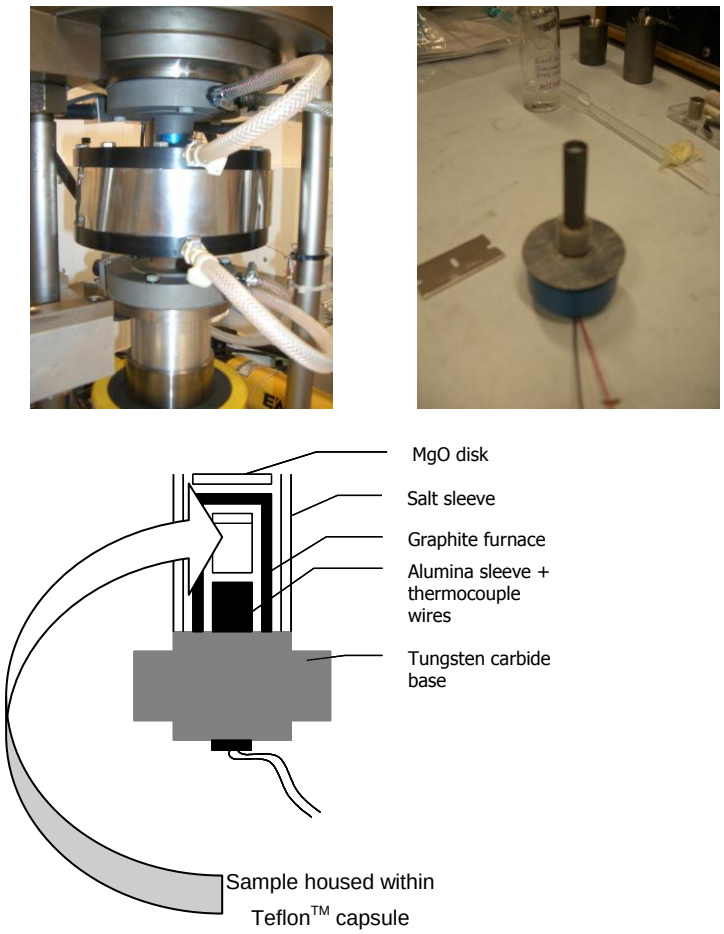

Figure 14: Quick press equipment a) piston press, b) graphite furnace sample holder and c) sample setup schematic showing Teflon™ capsule housing.

Samples of Al-NAT and both forms of Ga-NAT were used in exchange experiments (~50mg). Approximately 3-4 drops of saturated CsCl solution were added to the capsule before it was sealed with a Teflon™ lid. The sealed capsule was surrounded by a graphite furnace apparatus which allowed for temperature control during high-pressure experiments. The assembly of the sample housing and graphite furnace is shown in Figure 14. The sample housing was covered in a pressure transmitting salt sleeve (to protect the graphite furnace). Any free space within the sample housing was filled with MgO discs/powder. The sample holder is inserted into the piston press, where pressure is applied via a calibrated piston pump. The sample was brought to pressure before heating. Capsules were held at temperature and pressure for 0.5-4.5 hours followed by an isobaric quench. Samples were retrieved from the Teflon™ capsules, washed thoroughly in de-ionised water and dried in a desiccator for 48 hours. Analysis was by means of Powder X-ray diffraction (PXRD) using a Bruker D5000; and electron dispersive X-ray scanning electron microscope (EDX SEM), performed using a Philips XL30 microscope. The Quickpress ion exchange experiments performed are summarised in Table 2.

Table 2: Summary of the high-pressure, variable temperature Quickpress ion exchange experiments performed upon the three natrolite samples. Ion exchange medium was a saturated CsCl solution in each experiment.

		Sample	Pressure (GPa)	Temp (°C)	Time (hours)
Ideal Stoichiometery	**Al-Si-NAT** $Na_{16}Al_{16}Si_{24}O_{80}$	Temperature variation	1	60	1
			1	100	1
			1	150	1
		Reaction time variation	1	100	0.5
			1	100	1
			1	100	2.5
			1	100	4.5
	Ga-Si-NAT (orth) $Na_{16}Ga_{16}Si_{24}O_{80}$	Temperature variation	1	60	1
			1	100	1
			1	150	1
		Reaction time variation	1	100	0.5
			1	100	1
			1	100	2.5
			1	100	4.5
	Ga-Si-NAT (tet) $Na_8Ga_8Si_{12}O_{40}$	Temperature variation	1	60	1
			1	100	1
			1	150	1
		Reaction time variation	1	100	0.5
			1	100	1
			1	100	2.5
			1	100	4.5

2.5.4 Back-Exchange Reflux

Any samples which showed signs of ion exchange (following hydrothermal treatment or high pressure Quickpress treatment), were used in back-exchange experiments. The purpose of back-exchange reflux was to assess the ambient pressure reversibility of the ion exchange.

Back-exchange of samples was performed by reflux in a NaCl solution (5M, 250 ml), over 48 hours, with stirring. Samples were recovered, washed thoroughly in de-ionised water and dried in a desiccator for 48 hours. Analysis was by means of powder X-ray diffraction (PXRD) using a Bruker D5000; and electron dispersive X-ray scanning electron microscopy (EDX SEM), performed using a Philips XL30 microscope.

[1] Smart L. E.; Moore, E. A. 'Solid State Chemistry: An Introduction' **2005**. *Taylor & Francis.* 3rd Ed. Taylor & Francis.

[2] Snyder, J. 'Diffraction Theory, Introduction to X-ray Powder Diffraction' *Vol. 138,* Chapter 3, 47-95. ISBN 0-471-51339-3

[3] Cox D. E. 'Powder Diffraction' **1991** *Handbook of Synchrotron Radiation, Elsevier Science Publishers*. *Vol. 3*. Chapter 5, 155-200.

[4] Klug H. P.; Alexander L. E. 'X-ray diffraction procedures for polycrystalline and amorphous materials' **1972** *John Wiley and Sons*.

[5] Redfern S. A. T. 'Neutron powder diffraction of minerals at high pressure and temperatures: some recent developments and scientific applications' **2002**. *Eur. J. Mineral. 14* 251-261.

[6] Cheetham A. K.; Wilkinson A. P. 'Synchrotron X-ray and Neutron Diffraction Studies in Solid-State Chemistry' **1992**. *Angew. Chem. Int. Ed. Engl, 31*. 1557-1570.

[7] Langford J. I.; Louer D. 'Powder diffraction' **1996**. *Rep. Prog. Phys. 59*. 131-234.

[8] www.isis.stfc.ac.uk/about-isis/

[9] Walton R. **2002**. *Chem. Soc. Rev. 31*. 230-238.

[10] Hong S. B.; Kim S. H.; Kim Y. G.; Kim Y. C.; Barrett P. A.; Camblor M. A. 'Synthesis of microporous gallosilicates with the CGS topology' **1999**. *J. Mater. Chem. 9.* 2287.

[11] Hong S. B.; Lee S. H.; Shin C.-H.; Woo A. J.; Alvarez L. J.; Zicovich-Wilson C. M.; Camblor M. A. 'In Situ Disorder-Order Transformation in Synthetic Gallosilicate Zeolites with the NAT Topology' **2004.** *J. Am. Chem. Soc. 126(42).* 13742-13751.

[12] Paik W.C.; Camblor M.A.; Hong S.B. 'Microporous gallosilicate TNU materials and their implications for the synthesis of low-silica molecular sieves' **2001**. *Studies in Surface Science and Catalysis. 135.* 244.

[13] Cho H. H.; Kim S. H.; Kim Y. G.; Kim Y. C.; Koller H.; Camblor M. A.; Hong S. B. 'Synthesis and Characterization of Gallosilicate Molecular Sieves with High Gallium Contents: Examples of Structure Direction Exerted by Gallium' **2000**. *Chem. Mat. 12.* 2292 – 2300.

[14] Department of Physics, University of Warwick, Coventry, CV4 7AL.

[15] Eremets M. 'High Pressure Experimental Methods' **1996.** *Oxford University Press*.

[16] Holzapfel W. B.; Isaacs N. S. 'High Pressure Techniques in Chemistry and Physics-a Practical Approach'**1997**. *Oxford University Press*.

[17] Jayaraman A. 'Diamond anvil cell and high pressure physical investigations' **1983.** *Reviews of Modern Physics. 55, (1).* 65-107.

[18] Merril L.; Bassett W. A. **1974**. *Rev. Sci. Instrum. 45.* 290.

[19] Lemonnier M.; Fourme R.; Rosseaux F.; Kahn R. **1978**. *Nucl. Instrm. Methods*. *152.* 173-177.

[20] Lee Y.; Hriljac J. A.; Kim S. J.; Vogt T.; Parise J. B.; Artioli G. 'Pressure-induced volume expansion of zeolites in the Natrolite family' **2002.** *J. Am. Chem. Soc. 124.* 5466-5475.

[21] Smith G. C. *Synch.* **1991**. *Rad. News. 4.* 24-30.

[22] www.srs.ac.uk/srs/stations/station9.5hpt.htm

[23] www.isis.stfc.ac.uk/instruments/pearl/

[24] John Loveday, University of Edinburgh, School of Physics and Astronomy. http://www2.ph.ed.ac.uk/~jsl/

[25] HRPD User Manual, *ISIS facility*, Oxfordshire, UK.

[26] Rietveld, H. M. **1967**. *Acta. Cryst. 2.* 151.

[27] Rietveld, H. M. **1969.** *J. Appl. Cryst. 2.* 65-71.

[28] Young R. A. 'The Rietveld Method' **1996**. *Oxford University Press*, NY.

[29] Artioli G.; Smith J. V.; Kvick Å. 'Neutron diffraction study of natrolite, $Na_2Al_2Si_3O_{10}.2H_2O$, at 20 K.' **1984**. *Acta Cryst. C40*. 1658-1662.

[30] Evans Jr H. T.; Konnert J.A.; Ross M.. 'The crystal structure of tetranatrolite from Mont Saint-Hilaire, Quebec, and its chemical and structural relationship to paranatrolite and gonnardite' **2000**. *American Mineralogist. 85*. 1808-1815.

[31] Toby, B. H. 'EXPGUI, a graphical user interface for GSAS' **2001.** *J. App. Crystl. 34*. 210-213.

[32] Larson A. C. 'General Structure Analysis System (GSAS)' **2000**. *Los Alamos National Laboratory Report LAUR* 86-748.

[33] Angel, R. J. 'High pressure, high temperate crystal chemistry' **2001**. *Rev. Minerol. Geochem. 41*. 35-60.

[34] Angel R. J. **2001**. *Fit5.2 user manual.*

[35] Murnaghan F. D. 'Finite deformations of an elastic solid' **1937**. *Am. J. Math. 49.* 235-260.

[36] Birch F. 'Finite strain of cubic crystals' **1947**. *Phys. Rev. 71*. 809-824.

[37] Vinet P.; Ferranate J.; Smith J. R.; Rose J. H. 'A Universal Equation of State for Solids' **1986**. *J. Phys. C: Solid State. 19.* L467-L473.

[38] Lawes G. 'Scanning Electron Microscopy and X-ray Microanalysis' **1987** *John Wiley & Sons.*

[39] Centre for Electron Microscopy, University of Birmingham, Birmingham, UK.

[40] Choudhary A.; Banerjee S. 'Studies of natrolite type natural zeolite and its cation exchanged and adsorbed derivatives with cadmium (II) and NH_3 and H_2S' **2002**. *J. Indian. Chem. Soc. 79.* 580-582.

CHAPTER THREE

Synthesis, Characterisation and Preparation of Na-GaSi-NAT

As discussed in prior chapters, Na-GaSi-NAT can be synthesised in two forms: orthorhombic and tetragonal. These two forms were prepared via hydrothermal synthesis and a number of methods were used to characterise the samples, including: powder X-ray diffraction, thermogravimetric analysis, scanning electron microscope electron dispersive X-ray compositional analysis (SEM EDX), solid state NMR and high resolution powder neutron diffraction.

3.1 Synthesis and Optimisation

3.1.1 Orthorhombic Ga-Si-NAT

Phase pure batches of the orthorhombic form of gallosilicate natrolite were prepared using the method by Hong *et. al.*[1,2] and by Lee *et. al.*[3] See Table 1 for a summary of batch preparation and reaction conditions. Figure 1 shows the powder XRD pattern of phase pure orthorhombic Ga-Si-NAT with a match to the peaks searched in the JCPDS card number 79-1073. Full details of unit cell indexing and refinement is shown later within this chapter.

Table 1: Synthesis of orthorhombic Ga-Si-NAT as described by a) Hong *et. al.* [1] and b) Lee *et. al*[3].

Sample	Method	Batch Composition				Time/hrs	Temp/°C
		Na_2O	Ga_2O_3	SiO_2	H_2O		
GLL41	A	6.646	1	9.422	136.468	336	150
GLL09	B	3.086	1	4.992	196.814	120	150

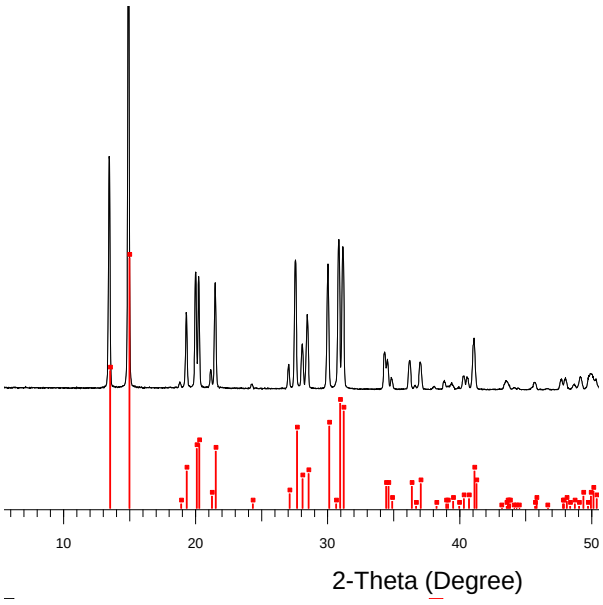

Figure 1: PXRD pattern of phase pure orthorhombic Na-GaSi-NAT (GLL41). Indexed peaks from card number 79-1073.

3.1.2 Tetragonal Ga-Si-NAT

The synthesis of tetragonal Na-GaSi-NAT has also been reported by Hong *et. al.*[1,2] In the tetragonal form, all T-sites are a mixture of Si and Ga. Hong described increased ordering when higher temperatures and/or longer reaction times are used. At the lower temperatures and reaction times used in the synthesis of the tetragonal form, Hong described disorder of the T atom sites with an increase of symmetry from Fdd2 (in orthorhombic), to *I-42d*.[1,2,4,5.]

In this report, tetragonal Na-GaSi-NAT was first synthesised according to Hong's method. A batch composition of $6Na_2O:Ga_2O_3:10SiO_2:144H_2O$ and a reaction time and temperature of 3 days and 100°C, was used; producing tetragonal Na-GaSi-NAT. The method includes heated mixing of gallium oxide in deionised water at 100°C for 24 hrs and ageing of the gel by stirring for a further 24 hrs at ambient temperature. Following these procedures, tetragonal Na-GaSi-NAT was hydrothermally synthesised, however there were some significant impurities (Table 2). An investigation into the effect of reaction time improved phase purity by substantially reducing the Ga-sodalite impurity

when reaction times were increased to 96 hours. The results of this study are summarised in Table 2 and shown in Figure 2.

Table 2: Summary of the results obtained by following Hong's[1] synthesis with variation in reaction time.

Sample ID	Time/hrs	XRD result
GLL10a	48	Ga-NAT_{tet} & Ga-sodalite
GLL10b	72	Ga-NAT_{tet} & trace amount of Ga-sodalite
GLL12b	76	Ga-NAT_{tet} & trace amount of Ga-sodalite
GLL52	96	Ga-NAT_{tet} & trace amount of Ga-sodalite

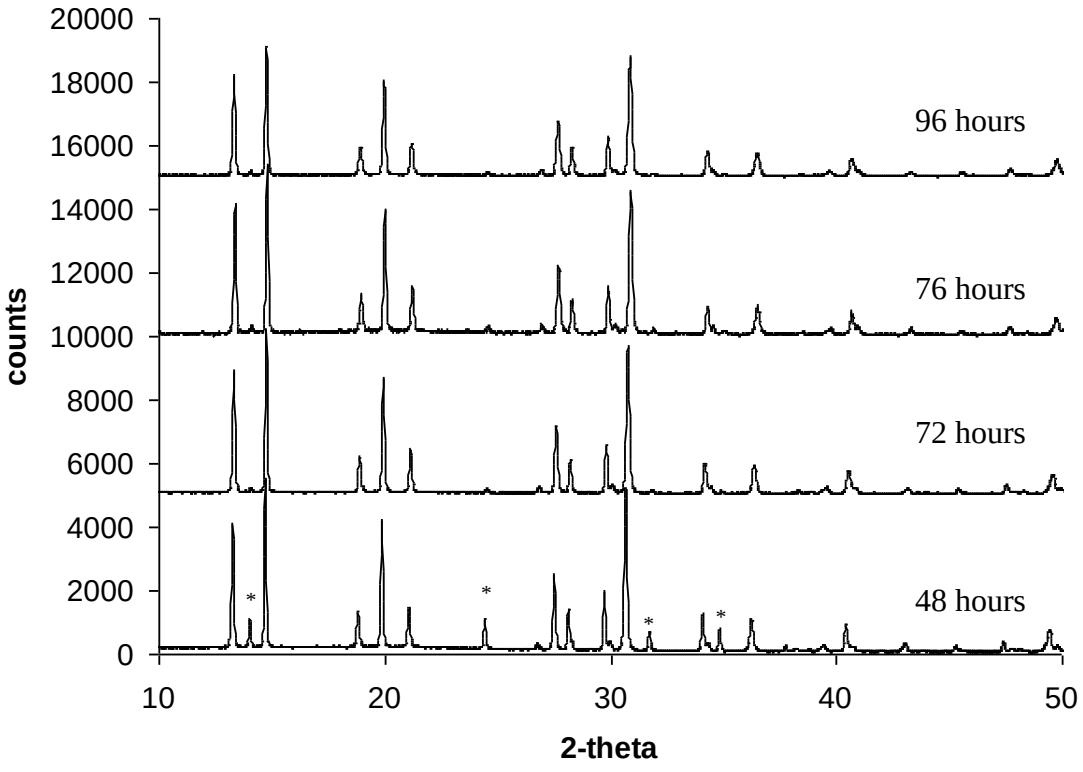

Figure 2: PXRD patterns for hydrothermally synthesised tetragonal Na-GaSi-NAT. Reaction time is varied from 48-96 hours, inclusive. Main Ga-sodalite peaks are indicated with an asterisk.

3.2 Indexing and Unit Cell Refinement

The Na-GaSi-NAT samples were indexed from overnight powder XRD patterns. ChekCell software was used to run refinements of the calculated pattern against the observed pattern. Calculated patterns were based on the reported unit cells of Na-Al-Si-NAT[6] and Tetranatrolite[7] for orthorhombic and tetragonal Na-GaSi-NAT, respectively. A summary of the indexed cells, PXRD patterns and selected refinement peaks are displayed for both gallosilicate samples in Table 3, Table 4 and Figure 3 to Figure 6. The final refinements are well matched to observed patterns, with some minor discrepancies due to poor peak resolution. In Figure 5, peaks 13, 14 and 18 in the orthorhombic pattern show splitting in the calculated cell which is unresolved in the observed data. Similarly some of the observed peaks in the tetragonal pattern (Figure 6), have unresolved peaks which have appeared as peak widening at the base or shoulders.

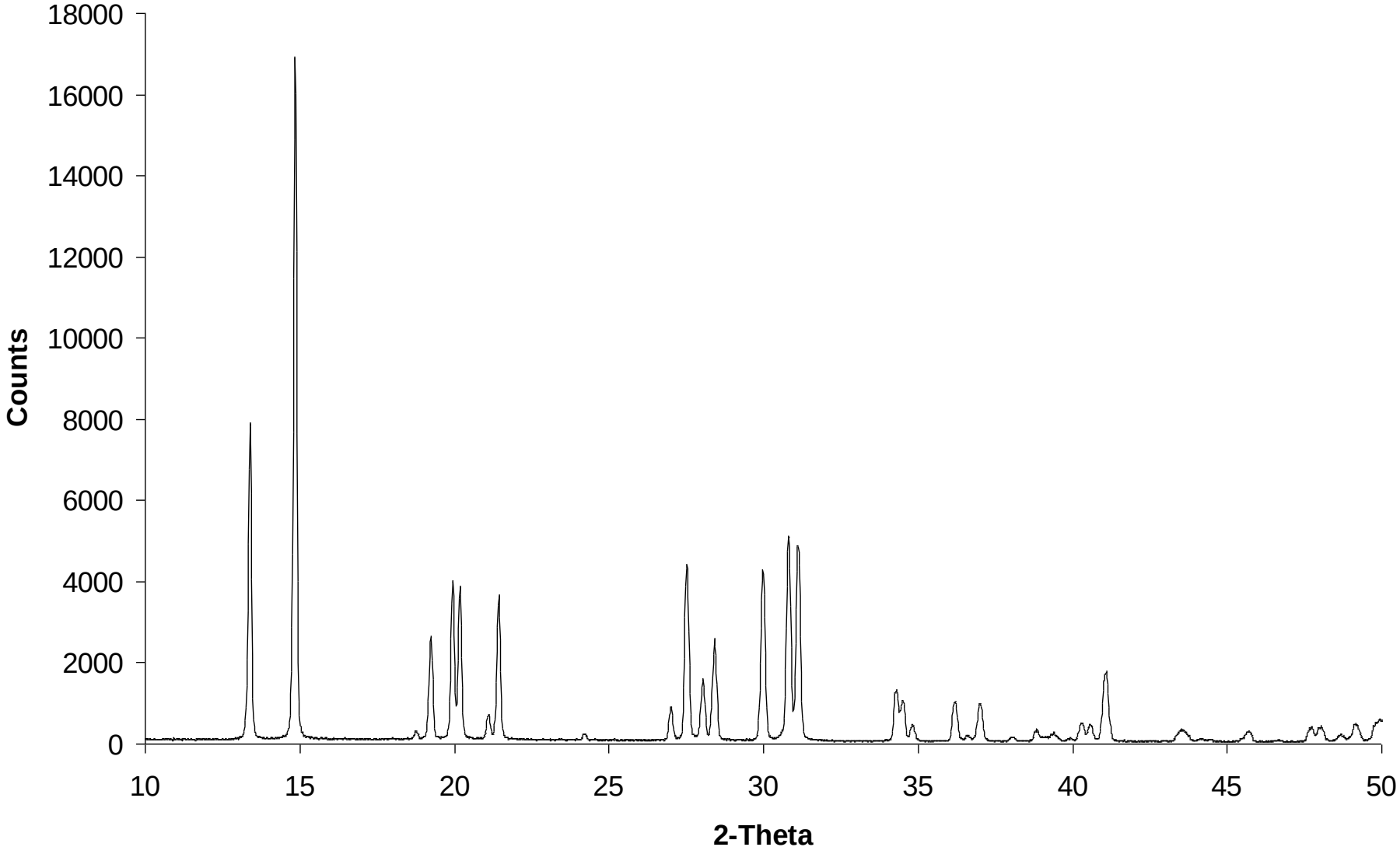

Figure 3: Powder XRD pattern of orthorhombic Na-GaSi-NAT (GLL41).

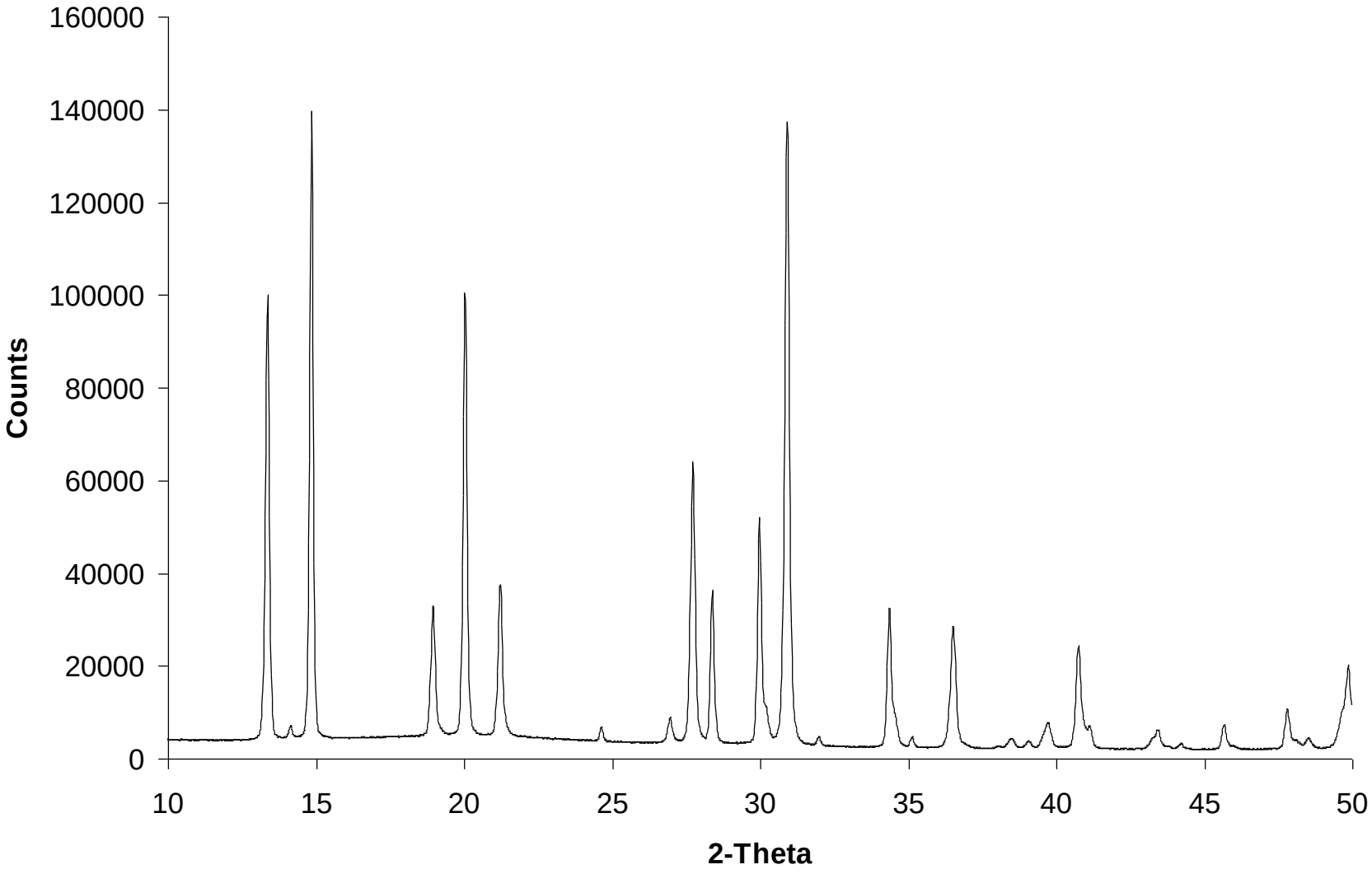

Figure 4: Powder XRD pattern of tetragonal Na-GaSi-NAT (GLL52).

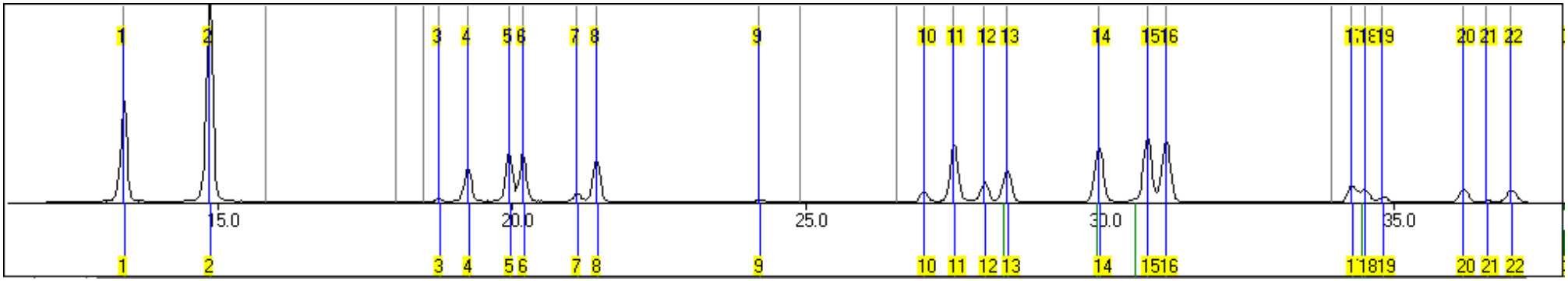

Figure 5: Orthorhombic Na-GaSi-NAT ChekCell diagrammatic refinement output of the observed diffraction pattern with peaks labelled in grey. Numbered peaks (blue), at the bottom of the diagram show matching calculated peaks post refinement.

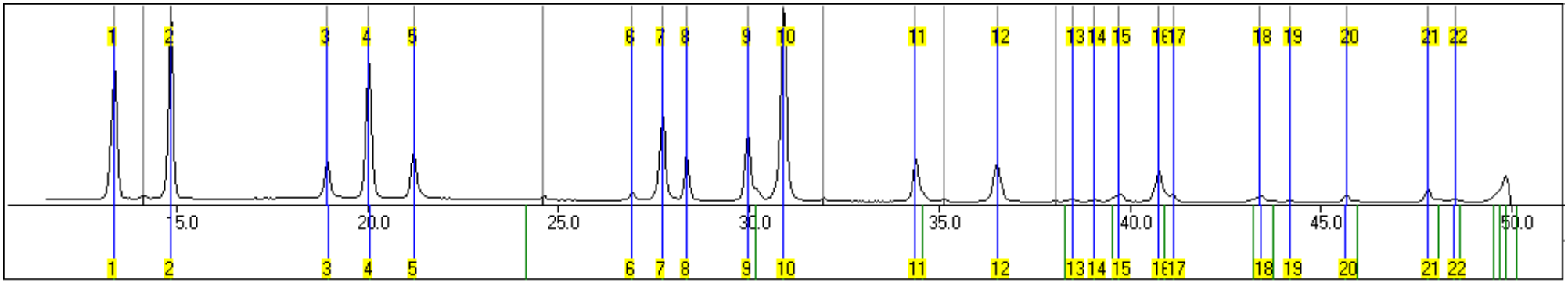

Figure 6: Tetragonal Na-GaSi-NAT ChekCell diagrammatic refinement output with the observed diffraction pattern and peaks labelled in grey. Numbered peaks (blue) at the bottom of the diagram show matching calculated peaks post refinement.

3.2.1 Orthorhombic Na-Ga-NAT

Table 3: Summary of refined unit cell and indexed peaks for orthorhombic Na-GaSi-NAT.

Unit cell	Orthorhombic
Space group	*Fdd2*
a	18.42(4) Å
b	18.91(4) Å
c	6.67(1) Å
α	90°
β	90°
γ	90°
Cell Volume	2325.993(40) $Å^3$

Peak	H	K	L	2Θ(obs)	2Θ(Calc)	diff.
1	2	2	0	13.3926	13.4153	-0.0227
2	1	1	1	14.8496	14.8764	-0.0268
3	0	4	0	18.7528	18.7652	-0.0124
4	4	0	0	19.2404	19.2635	-0.0231
5	1	3	1	19.9379	19.9645	-0.0266
6	3	1	1	20.1779	20.2009	-0.023
7	2	4	0	21.1049	21.1168	-0.0119
8	4	2	0	21.4277	21.4523	-0.0246
9	3	3	1	24.1944	24.2294	-0.035
10	4	4	0	26.9996	27.019	-0.0194
11	1	5	1	27.5145	27.5324	-0.0179
12	5	1	1	28.0366	28.0547	-0.0181
13	2	0	2	28.4199	28.452	-0.0321
14	2	2	2	29.9843	30.0111	-0.0268
15	3	5	1	30.8074	30.8229	-0.0155
16	5	3	1	31.1221	31.1384	-0.0163
17	2	4	2	34.2915	34.3037	-0.0122
18	4	2	2	34.507	34.5192	-0.0122
19	6	4	0	34.8119	34.8281	-0.0162
20	1	7	1	36.1915	36.1945	-0.003
21	5	5	1	36.5837	36.605	-0.0213
22	7	1	1	36.9954	37.0115	-0.0161

3.2.2 Tetragonal Na-Ga-NAT

Table 4: Summary of refined unit cell and indexed peaks for tetragonal Na-GaSi-NAT.

Unit cell	Tetragonal
Space group	*I-42d*
a	13.23(4)
b	13.23(4)
c	6.678(2)
α	90
β	90
γ	90
Cell Volume	1170.505(14)

Peak	H	K	L	2Θ(obs)	2Θ(Calc)	diff.
1	0	2	0	13.3549	13.376	-0.0211
2	1	0	1	14.8411	14.8563	-0.0152
3	2	2	0	18.9407	18.96	-0.0193
4	1	2	1	20.0259	20.0415	-0.0156
5	1	3	0	21.217	21.2225	-0.0055
6	0	4	0	26.9333	26.9388	-0.0055
7	3	2	1	27.7061	27.7251	-0.019
8	1	1	2	28.3634	28.3756	-0.0122
9	2	0	2	29.9759	29.97	0.0059
10	4	1	1	30.8937	30.9003	-0.0066
11	1	3	2	34.3486	34.351	-0.0024
12	3	4	1	36.506	36.5047	0.0013
13	4	4	0	38.4647	38.4656	-0.0009
14	2	5	1	39.0436	39.0423	0.0013
15	3	5	0	39.6901	39.6984	-0.0083
16	2	4	2	40.7419	40.7313	0.0106
17	1	0	3	41.1247	41.1142	0.0105
18	1	2	3	43.3875	43.4251	-0.0376
19	5	1	2	44.1901	44.1855	0.0046
20	3	0	3	45.6591	45.6415	0.0176
21	2	3	3	47.7916	47.7769	0.0147
22	5	3	2	48.5002	48.4838	0.0164

3.3 TGA

Thermogravimetric experiments were performed on both orthorhombic and tetragonal samples of the gallosilicate materials, see Figure 7 and Figure 8. These experiments were performed in order to assess the water content (specifically the intrapore water content), of the samples. These have been interpreted to give an approximate unit cell water content by dissection of the results into surface and structural water content; this was not straightforward for the tetragonal sample as there is not a definitive intrapore water loss step.

We might expect that the loosely bound, intrapore water molecules would show a distinct step starting at ≥100°C. This is not the case. Both results show a gradual and small weight decrease starting at temperatures <100°C. This, we could assume, was the evaporation of surface water molecules as the sample is heated. In an effort to explore the nature of this gradual weight loss, TGA traces were performed where the temperature was oscillated (in the region before a distinct and clear weight loss step). Oscillation of evaporation temperatures should also show oscillation in the weight of sample, as water is evaporated and condensed on the surface. In this way the TGA experiments should give some limited distinction between surface water and intrapore water molecules.

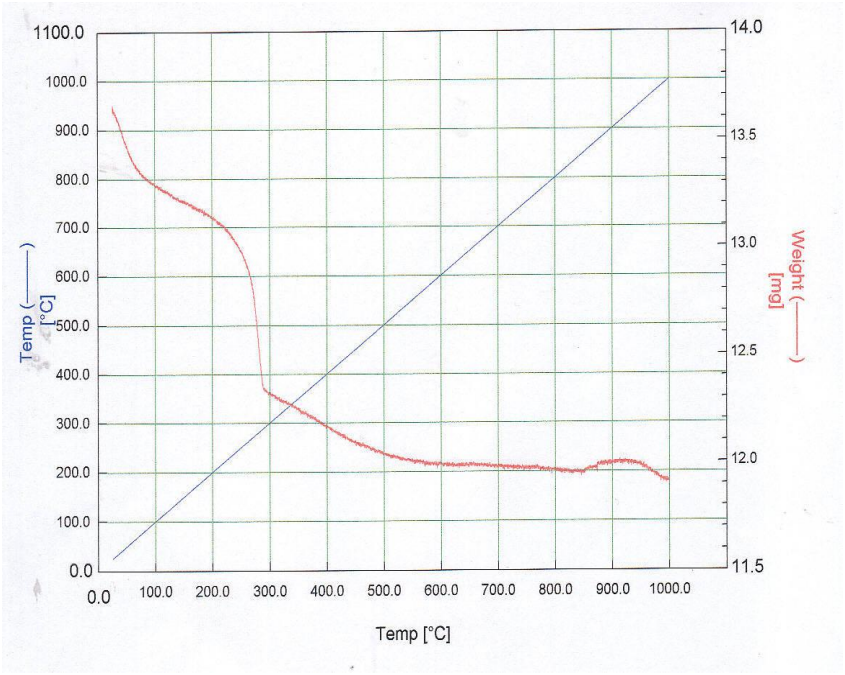

A)

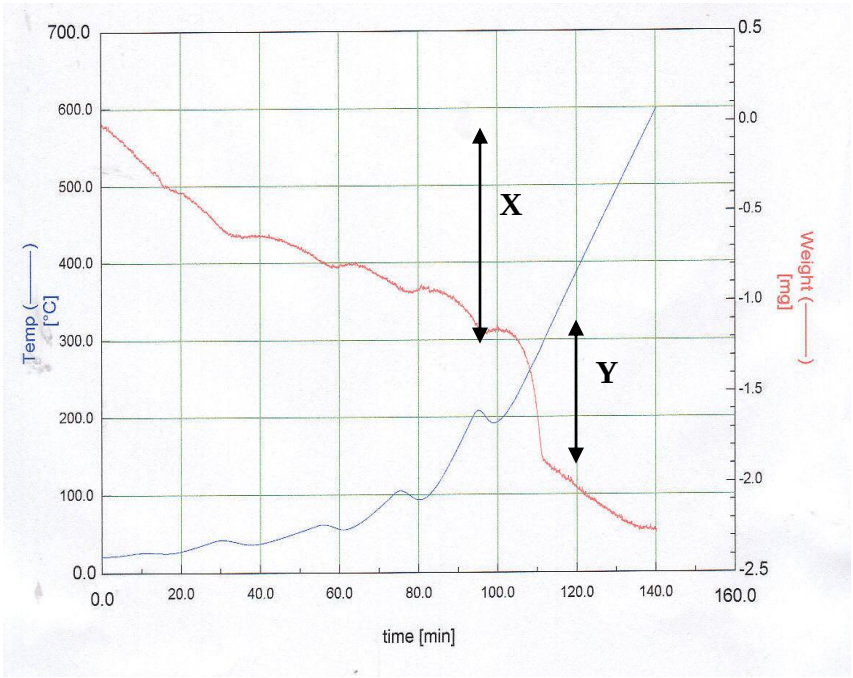

B)

Figure 7: Thermogravimetric analysis of tetragonal Na-GaSi-NAT: a) experiment performed up to 1000°C at a steady rate of heating; b) experiment performed up to 600°C with oscillating heating in the low temperature region to elucidate the surface water content. X is the weight loss due to surface water and Y due to intrapore water molecules.

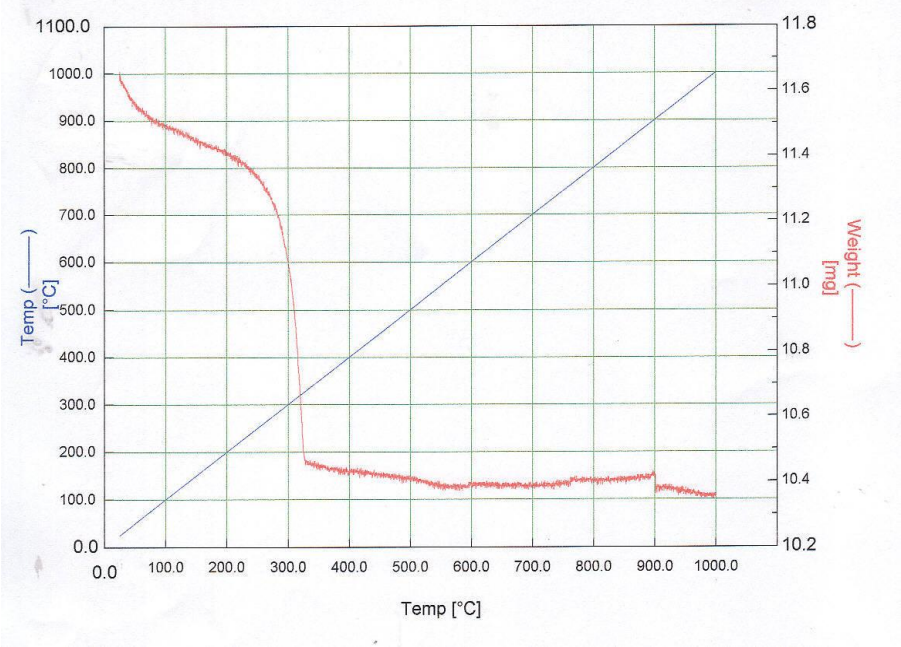

A)

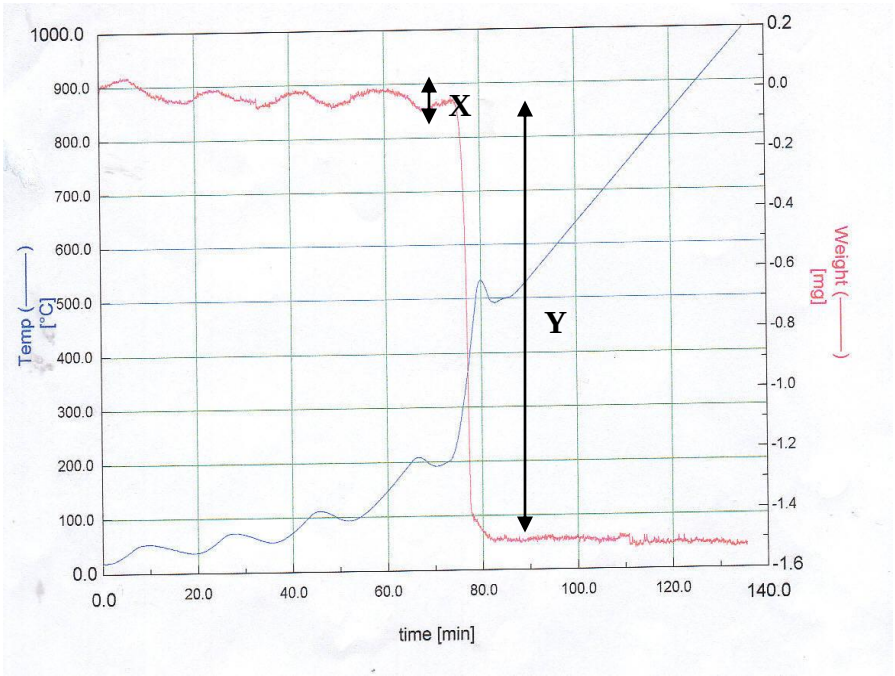

B)

Figure 8: Thermogravimetric analysis of orthorhombic Na-GaSi-NAT: a) experiment performed up to 1000°C at a steady rate of heating; b) experiment performed up to 600°C with oscillating heating in the low temperature region to elucidate the surface water content. X is the weight loss due to surface water and Y due to intrapore water molecules

Table 5 shows the breakdown of TGA data by conversion of percentage weight loss into surface (X) and intrapore water (Y); to give a final unit cell composition of both tetragonal ($Na_8Ga_8Si_{12}O_{40}.8.0H_2O$) and orthorhombic ($Na_{16}Ga_{16}Si_{24}O_{80}.16.7H_2O$) gallosilicates.

The slightly higher temperature range of intrapore water release seen in orthorhombic (225-325°C) compared to tetragonal (200-280°C), suggests that the orthorhombic framework forms slightly stronger bonds to intrapore water molecules. This assumption could be explained by comparison of the T-site ordering seen in both framework types. In orthorhombic Na-GaSi-NAT, we see regular ordering. In comparison the disordering in the tetragonal form produces a much more open, flexible framework. We would expect this flexibility to be reflected in the ease of intrapore water removal from the tetragonal framework, lowering the temperature at which it is lost during TGA analysis.

The tetragonal gallosilicate sample shows a massively increased surface water value compared to that of the corresponding orthorhombic sample (9.6 % versus 0.57%). One possible explanation for this is the difference in particle surface area. A large particle surface area would give increased surface water values. In the following section: SEM EDX analysis; particle morphology pictures show a difference between the two samples (see Figure 9). Tetragonal Na-GaSi-NAT shows much smaller, ‘softer’, almost powder-like particles. Orthorhombic Na-GaSi-NAT show very large (100-200μm) prismatic particles representing a much reduced surface area in comparison.

Table 5: Results from thermogravimetric experiments performed upon orthorhombic and tetragonal Ga-Si-NAT.

		Tetragonal Na-GaSi-NAT (11.445 mg)	Orthorhombic Na-GaSi-NAT (17.497 mg)
Weight loss/mg	X+Y	1.9	1.5
	X	1.1	0.1
	Y	0.8	1.4
Weight Loss/%	X	9.6111	0.5715
	Y	6.9900	8.0014
	X+Y	16.6011	8.5729
Water content/molecules per unit cell	Estimated Surface water content (X)	11.0042	1.1928
	Inter-pore water content (Y)	7.9965	16.6996
	Total (X+Y)	19.0007	17.8924
Temperature range of intrapore water release		200-280°C	225-325°C
Unit Cell		$Na_8Ga_8Si_{12}O_{40}.8.0H_2O$	$Na_{16}Ga_{16}Si_{24}O_{80}.16.7H_2O$
Anhydrous RMM		1718.76	3437.52
Total RMM		1862.82	3738.36

3.4 SEM EDX

SEM EDX analysis was performed in order to assess sample morphology and the elemental composition of each gallosilicate sample. Analysis of the corresponding aluminosilicate sample was also performed for comparison. Specifically, the T atom ratio is of interest (this should be 1.5 for pure samples) as well as the cation content (needed in later ion exchange work). A summary of compositional results are displayed in Figure 9 and Table 6. These results show reasonably pure samples with T atom ratios well within the expected regions. The cation content is very slightly less than the expected unit cell content of 8 and 16 for tetragonal and aluminosilicate orthorhombic samples, but the Na:Al ratio is essentially the expected 1:1. The situation is slightly worse for the orthorhombic gallosilicate, where the Na:Ga ratio is 0.92. This could possibly indicate trace cation impurities, although fluctuations from idea composition could also be attributed to a large error value in results due to small sampling areas (typically 500μm^2). Slight 'dealumination' or 'degallination' could be responsible for the low Al content.

The morphology of the samples shown in Figure 9 clearly varies with composition. The aluminosilicate shows needle-like particles; very different to that seen for the gallosilicate analogues. Orthorhombic Na-GaSi-NAT shows prismatic particles. This agrees well with the findings of Hong[8]; who described them as orthorhombic prisms of approximately 20 μm (although slightly larger in this report). Similarly, Hong describes tetragonal Na-GaSi-NAT as appearing to be a spherical aggregate; again showing good agreement with the morphological findings in this report.

Figure 9: SEM Images and EDX elemental analysis spectra for orthorhombic Na-Ga-NAT, tetragonal Na-Ga-NAT and orthorhombic Na-Al-NAT.

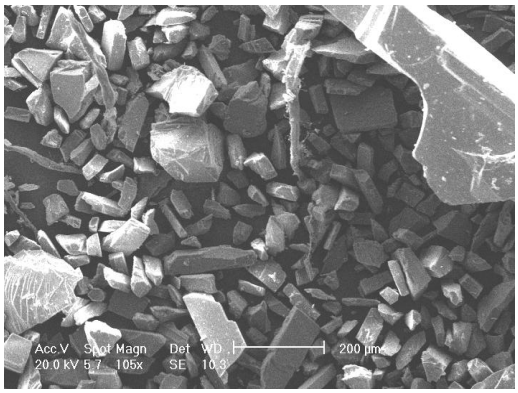

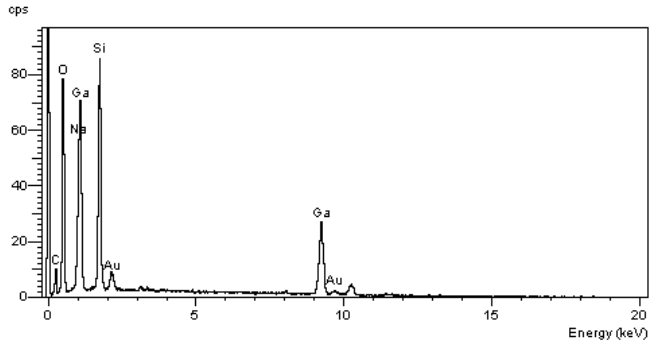

Orthorhombic Ga-NAT

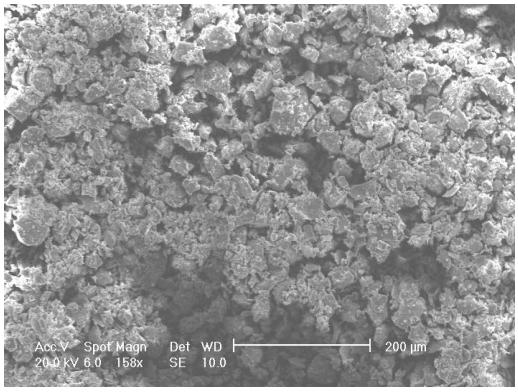

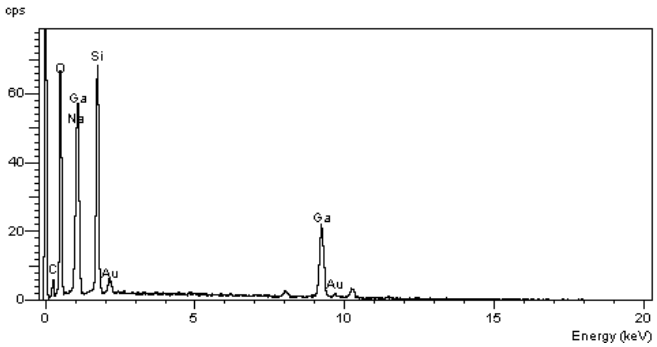

Tetragonal Ga-NAT

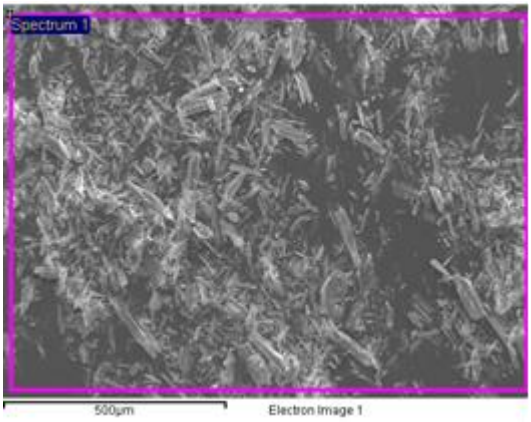

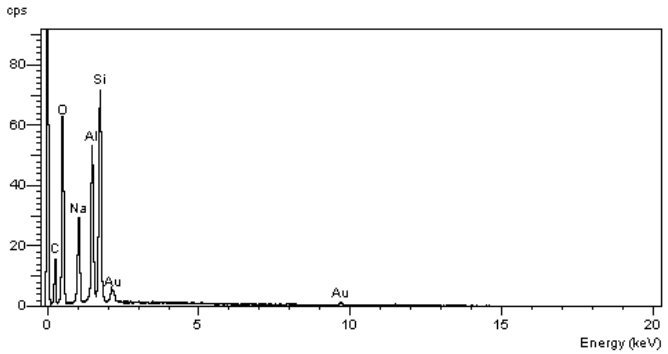

Orthorhombic Al-NAT

Table 6: SEM EDX data for tetragonal Ga-NAT, orthorhombic Ga-NAT and orthorhombic Al-NAT.

Tetragonal Ga-NAT

Scan	Si/Ga	SEM EDX Atomic %				X	Unit Cell Contents			
		O*	Na	Si	Ga		Na	Si	Ga	O*
1	1.58	66.21	9.35	14.95	9.49	0.80	7.51	12.00	7.62	39.23
2	1.60	66.56	9.43	14.77	9.24	0.81	7.66	12.00	7.51	39.01
3	1.60	65.97	9.35	15.18	9.50	0.79	7.39	12.00	7.51	39.02
4	1.57	66.56	9.29	14.77	9.38	0.81	7.55	12.00	7.62	39.24
5	1.59	66.18	9.21	15.11	9.49	0.79	7.31	12.00	7.54	39.07
6	1.61	66.68	9.11	14.95	9.27	0.80	7.31	12.00	7.44	38.88
7	1.59	66.60	9.10	14.90	9.40	0.81	7.33	12.00	7.57	39.14
8	1.58	66.50	9.19	14.88	9.42	0.81	7.41	12.00	7.60	39.19
9	1.59	67.35	9.03	14.49	9.14	0.83	7.48	12.00	7.57	39.14
10	1.52	69.20	8.85	13.23	8.72	0.91	8.03	12.00	7.91	39.82
Average	1.58						7.50	12.00	7.59	39.18

Orthorhombic Ga-NAT

Scan	Si/Ga	SEM EDX Atomic %				X	Unit Cell Contents			
		O*	Na	Si	Ga		Na	Si	Ga	O*
1	1.56	66.16	8.76	15.28	9.80	1.57	13.76	24.00	15.39	78.79
2	1.56	66.35	8.63	15.26	9.77	1.57	13.57	24.00	15.37	78.73
3	1.55	66.85	8.65	14.91	9.60	1.61	13.92	24.00	15.45	78.91
4	1.56	67.06	8.86	14.65	9.42	1.64	14.51	24.00	15.43	78.86
5	1.59	65.90	9.15	15.30	9.65	1.57	14.35	24.00	15.14	78.27
6	1.57	66.02	8.99	15.27	9.72	1.57	14.13	24.00	15.28	78.55
7	1.55	66.40	9.02	14.94	9.65	1.61	14.49	24.00	15.50	79.00
8	1.55	66.24	8.89	15.12	9.74	1.59	14.11	24.00	15.46	78.92
9	1.56	66.21	9.32	14.92	9.55	1.61	14.99	24.00	15.36	78.72
10	1.54	66.22	8.75	15.20	9.84	1.58	13.82	24.00	15.54	79.07
Average	1.56						14.17	24.00	15.39	78.78

Orthorhombic Al-NAT

Scan	Si/Al	SEM EDX Atomic %				X	Unit Cell Contents			
		O*	Na	Si	Al		Na	Si	Al	O*
1	1.65	63.93	7.23	17.97	10.88	1.34	9.66	24.00	14.53	77.06
2	1.56	65.63	9.57	15.13	9.67	1.59	15.18	24.00	15.34	78.68
3	1.60	65.21	9.57	15.52	9.71	1.55	14.80	24.00	15.02	78.03
4	1.61	65.08	9.55	15.66	9.72	1.53	14.64	24.00	14.90	77.79
5	1.60	65.37	9.56	15.43	9.64	1.56	14.87	24.00	14.99	77.99
6	1.64	65.61	9.32	15.40	9.38	1.56	14.52	24.00	14.62	77.24
7	1.59	65.54	9.47	15.34	9.65	1.56	14.82	24.00	15.10	78.20
8	1.63	65.49	9.59	15.43	9.49	1.56	14.92	24.00	14.76	77.52
9	1.57	65.46	9.51	15.30	9.73	1.57	14.92	24.00	15.26	78.53
10	1.58	66.15	9.33	15.02	9.49	1.60	14.91	24.00	15.16	78.33
Average	1.60						14.32	24.00	14.97	77.94

* SEM EDX atomic % figures are inaccurate as a method of determining O content within the unit cell as the O signal is of low energy and hard to measure accurately. The framework oxygen content is estimated as double the total T atom content. X is the multiplier to convert atomic % results into stoichiometric unit cell values.

3.5 MAS NMR

^{29}Si and ^{71}Ga MAS NMR data were collected on both the tetragonal and orthorhombic samples to assist in the structural elucidation of the gallosilicate framework, specifically to provide supporting evidence for the order/disorder of the T sites. For experimental details see chapter 2. Results are displayed in Table 7, with spectra shown in Figure 10 and Figure 11.

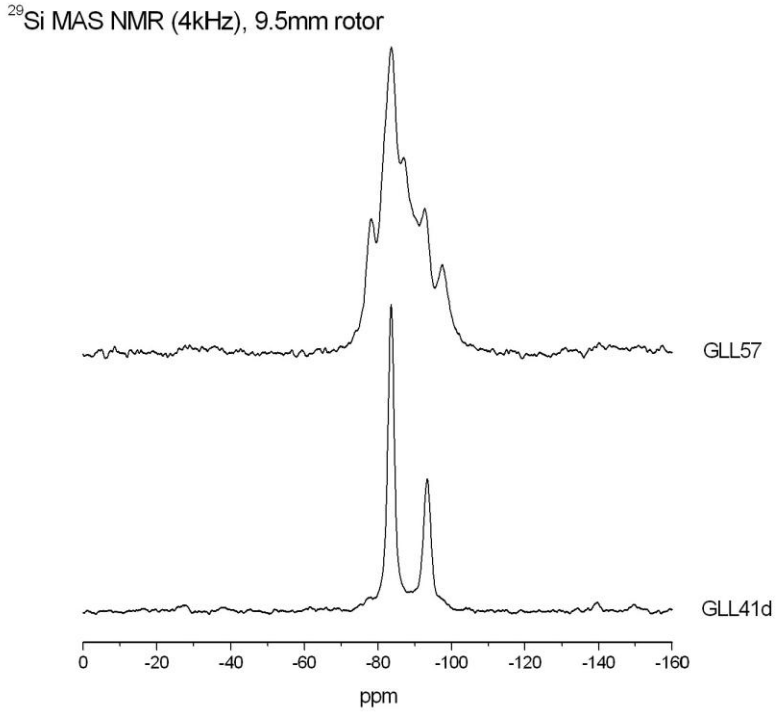

Figure 10: ^{29}Si NMR spectra for tetragonal and orthorhombic Ga-NAT (GLL57 and GLL41d, respectively). Peak positions are 1 to 5 from left to right.

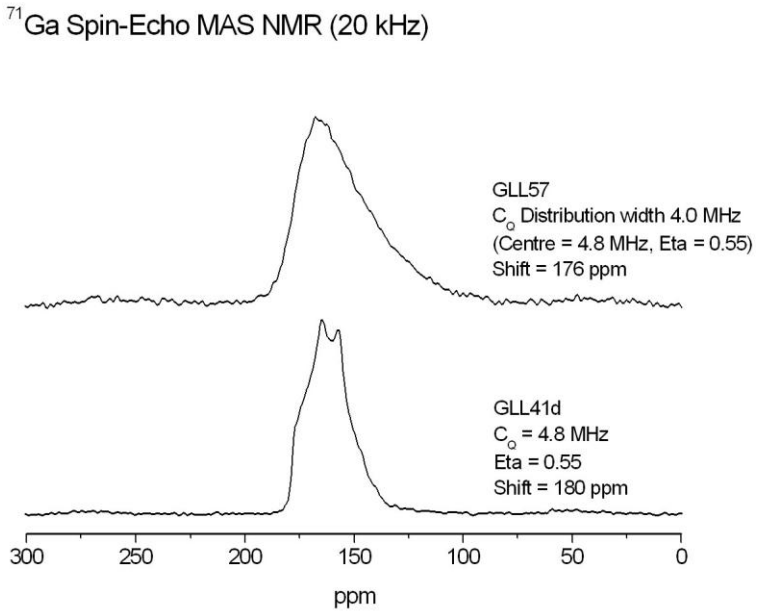

Figure 11: ^{71}Ga NMR spectra for tetragonal and orthorhombic Ga-NAT (GLL57 and GLL41d, respectively).

Table 7: Tabulation of ^{29}Si NMR data for tetragonal and orthorhombic Ga-NAT.

Tetragonal Ga-NAT			
peak	δ, ppm	Width, Hz	Intensity, %
5	-97.75	218	7.24
4	-92.38	291	16.04
3	-87.66	301	17.95
2	-83.37	341	51.80
1	-78.07	156	6.97
Orthorhombic Ga-NAT			
peak	δ, ppm	Width, Hz	Intensity, %
4	-93.39	160	34.02
2	-83.58	131	65.98

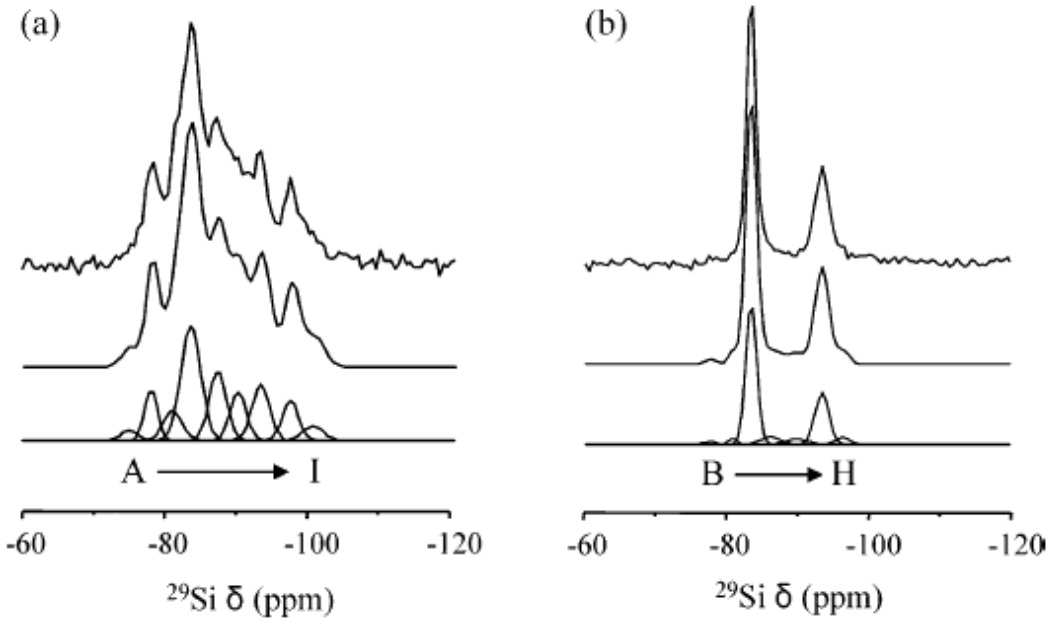

Figure 12: ^{29}Si NMR spectra as reported by Hong et. al.[9]
a) Tetragonal Ga-NAT and b) orthorhombic Ga-NAT. Observed spectra (top), simulated (middle) and deconvoluted (bottom). The deconvoluted components are denoted from left to right as A-I and B-H respectively.

Hong et. al.[1] have reported both observed and simulated ^{29}Si NMR data based the expected chemical shifts for the average T-O-T angles and the Si/Ga ratio (from elemental analysis). A comparison of Hong's data to that presented in this report can be seen in Table 8 and Table 9. From this comparison we see excellent agreement. The tetragonal form shows a difference in chemical shift ($\Delta\delta$), from a minimum of 0.07ppm to a maximum of 0.72ppm across the 5 peaks. Similarly the orthorhombic form agrees well with Hong's report, giving a $\Delta\delta$ of 0.12ppm and 0.21ppm for the two peaks.

Table 8: Comparison of ^{29}Si NMR data collected for tetragonal Ga-NAT, to that analysed by Hong et. al.[1]

Si Site	Multiplicity	Structural unit	δ, ppm				Peak label	
			Calc[a]	Obs				
				a	b	c	a	b
Si_2	4	Si_2(4Ga)	-75.0	-74.9			A	
		Si_2(3Ga)	-81.7	-81.0			C	
		Si_2(2Ga)	-88.4	-87.2	-87.66	0.46	E	3
		Si_2(1Ga)	-95.1	-93.1	-92.38	-0.72	G	4
		Si_2(0Ga)	-101.8	-100.3			I	
Si_1	16	Si_1(4Ga)	-78.6	-78.0	-78.07	0.07	B	1
		Si_1(3Ga)	-85.3	-83.5	-83.37	-0.13	D	2
		Si_1(2Ga)	-92.0	-90.0			F	
		Si_1(1Ga)	-98.7	-97.2	-97.75	0.55	H	5
		Si_1(0Ga)	-105.4					

a) Results from Hong et. al.[1], b) results from this report, c) a-b.

Table 9: Comparison of ^{29}Si NMR data collected for orthorhombic Ga-NAT, to that analysed by Hong et. al.[1]

Si Site	Multiplicity	Structural unit	δ, ppm				Peak label	
			Calc[a]	Obs				
				a	b	c	a	b
Si_2	8	Si_2(4Ga)	-78.8	-81.1			C	
		Si_2(3Ga)	-85.5	-86.4			E	
		Si_2(2Ga)	-92.2	-93.6	-93.39	-0.21	G	4
		Si_2(1Ga)	-98.9					
		Si_2(0Ga)	-105.6					
Si_1	16	Si_1(4Ga)	-75.4	-78.0			B	
		Si_1(3Ga)	-82.1	-83.7	-83.58	-0.12	D	2
		Si_1(2Ga)	-88.8	-90.1			F	
		Si_1(1Ga)	-95.5	-96.5			H	
		Si_1(0Ga)	-102.2					

a) Results from Hong et. al.[1] b) results from this report, c) a-b.

Si/Ga ratio calculation:

$$Si/Ga = \frac{\sum_n I_n}{\sum_n \left(\frac{n}{4}\right) I_n}$$

Using the results obtained from the ^{29}Si NMR spectra, the T atom ratio was calculated for both gallosilicate forms, using the above equation, (where n is the number of Ga neighbours for the peak with intensity I_n). These ratios are compared to those obtained via SEM EDX elemental analysis in Table 10. From this comparison, we see good agreement between the two methods and further confirmation of good phase purity.

Table 10: Comparison of the T atom ratios calculated using ^{29}SiNMR peak information and SEM EDX analysis, for both tetragonal and orthorhombic Ga-NAT.

	Si/Ga ratio		diff
	NMR	SEM EDX	
Orthorhombic	1.50	1.56	-0.06
Tetragonal	1.65	1.58	0.07

The two peaks observed in the ^{29}Si NMR spectra of orthorhombic Ga-NAT, at an intensity ratio of 2:1, have been reported many times in relation to well ordered aluminosilicate natrolite materials; with specific assignment to the Si2(2Al) and the Si1(3Al) structural units.[9,10,11,12] This corresponds strongly to the conclusions drawn here, and supported by neutron diffraction results presented later in the chapter, for an ordered orthorhombic gallosilicate framework. In the case of tetragonal Ga-NAT, the presence of a number of peaks associated with different structural units means that, in-order to agree with an approximate 1.5 Si/Ga ratio, the T atom sites must be completely disordered.

3.6 Preparation for Neutron Diffraction Studies-Sample Deuteration

In order to conduct powder neutron diffraction experiments upon the gallosilicate samples, replacement of all hydrogen atoms within the structure with deuterium is required. Structural hydrogen is replaced with deuterium atoms via D_2O/H_2O exchange. Deuteration of theses samples was investigated using two methods: vacuum dehydration followed by reaction with D_2O and hydrothermal exchange in D_2O (see section 2.4.2 in chapter 2 for experimental details). Using these two methods it was clear very early on that the vacuum dehydration technique was causing deformation and/or collapse of the framework. This can be seen when comparing the PXRD patterns of samples used in the two techniques; the sample undergoing vacuum dehydration shows reduced crystallinity (see Figure 13).

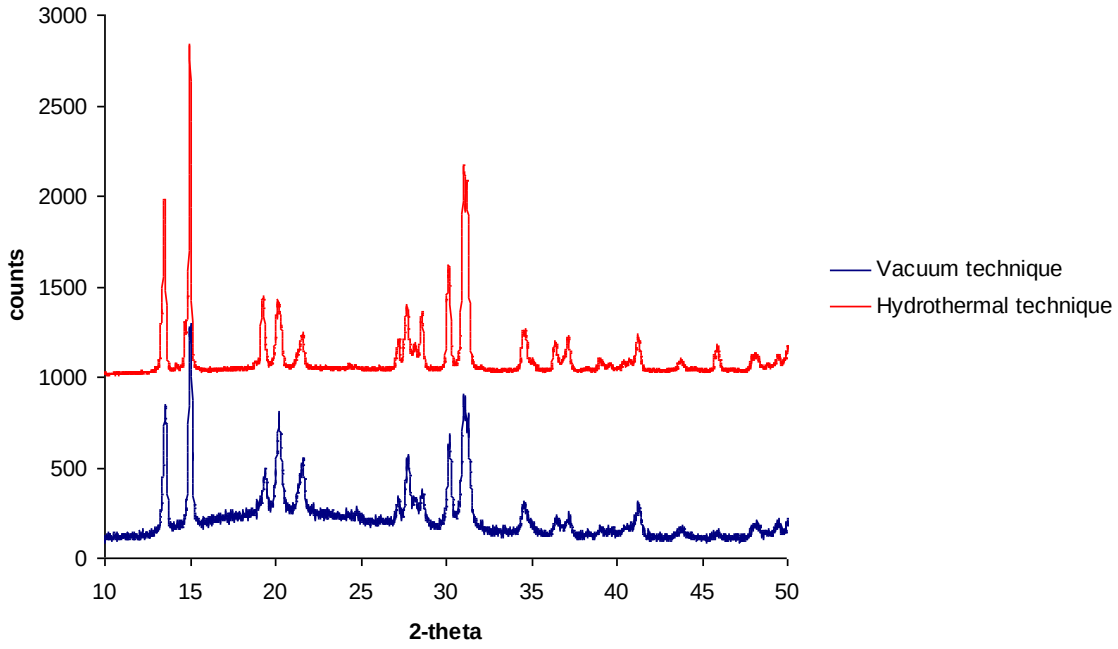

Figure 13: PXRD patterns of tetragonal Na-GaSi-NAT samples used in both vacuum and hydrothermal deuteration studies.

Hydrothermal D_2O/H_2O exchange proved most successful, although detection of the extent of exchange was difficult due to rapid back exchange with atmospheric H_2O. In

order to prevent back exchange a number of handling and detection methods were implemented:

- Storing/transporting samples in sealed vials
- Handling samples under a dry argon atmosphere (or under a stream of dry nitrogen).
- Using a diamond reflectance insert during FTIR spectroscopy. This means it was possible to record the relative D_2O and H_2O peaks without the need for hydroscopic KBr.

Based on FTIR spectra using an ATR attachment, the results of hydrothermal deuteration show a D_2O peak (Figure 14), which is not seen when using a KBr disc. This deuteration level can be maintained if the sample is stored in a capped vial (see Figure 15), but atmospheric H_2O exchange occurs when the sample is exposed to the atmosphere (see Figure 16).

A mass spectrum analysis of hydrothermally deuterated Na-GaSi-NAT handled under argon was performed and can be seen in Figure 17. This spectrum confirms the presence of a significant amount of D_2O, but still not 100%. Peaks at 17, 18, 19 and 20 are associated with OH, OD/H_2O, DOH and D_2O, respectively.

During both FTIR and mass spectroscopy analysis the deuterated samples were handled in air for a short time, a requirement of the analytical techniques. From the FTIR studies performed after 1 hour exposure to the atmosphere it can be assumed that some atmospheric exchange occurs even within a few minutes of exposure. Therefore when neutron diffraction studies were performed, all deuterated samples were carefully sealed in a closed vial under argon and loaded quickly into sample cells under a stream of nitrogen. Results from neutron diffraction experiments (discussed in this chapter and chapter 4), show that avoiding any atmospheric exposure maintained deuteration close to 100 % for the orthorhombic form. However the tetragonal form showed some hydrogen presence in high pressure neutron diffraction experiments, indicated by a high signal to noise ratio.

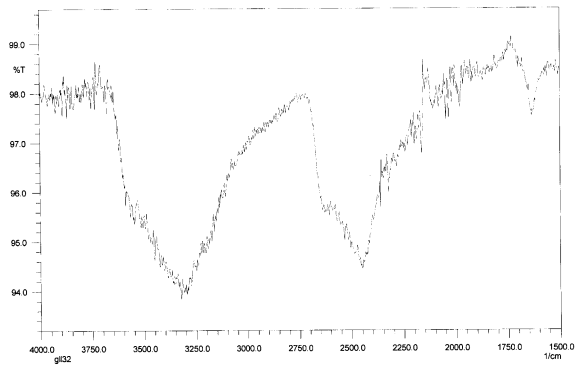

Figure 14: FT-IR spectrum of tetragonal Na-Ga-NAT heated in D_2O at 100°C for 24hrs.

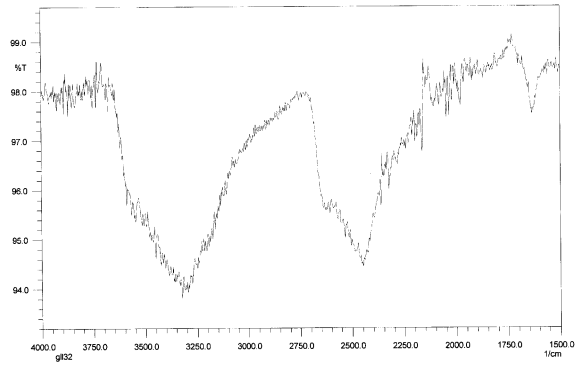

Figure 15: FT-IR spectrum of tetragonal Na-Ga-NAT heated in D_2O at 100°C for 24hrs, then stored in a capped vial for 24hrs.

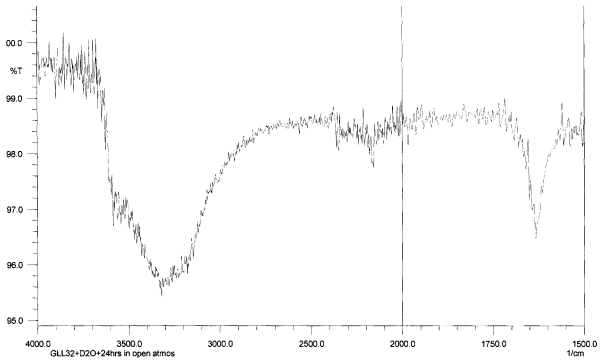

Figure 16: FT-IR spectrum of tetragonal Na-Ga-NAT heated in D_2O at 100°C for 24hrs, then exposed to atmospheric moisture for 1 hr.

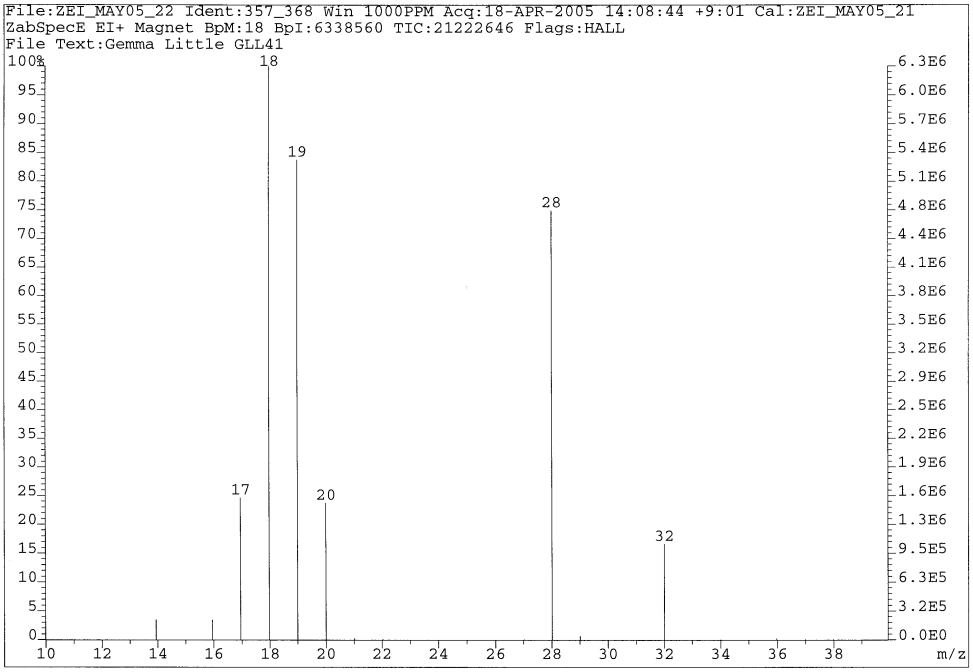

Figure 17: Mass spectrum of deuterated Na-GaSi-NAT handled under an argon atmosphere.

3.7 High Resolution Neutron Powder Diffraction

Samples of both tetragonal and orthorhombic gallosilicate natrolite were taken to the HRPD beamline at ISIS, Rutherford Appleton Laboratory, and loaded into thin-walled vanadium cans. Neutron diffraction experiments were performed followed by Rietveld refinement. These experiments were performed with the expectation that the high resolution would allow for the structural determination of both forms with a specific emphasis on the water content. For details of the experimental set up see Chapter 2. For each sample, data were collected from three banks: 168, 90 and 30 degrees. In each experiment the data collected using the 30 degrees bank gave very few distinguishable peaks and was therefore unusable for crystallographic refinement.

3.7.1 Orthorhombic Ga-NAT

Experiments were performed at room temperature and pressure. Refinable data were collected for the orthorhombic sample with very good criteria of fit when using bank 1 (168 degrees), rather than bank 2 (90 degrees). Refinement of the two banks combined gave averaged criteria of fit values and offered no improvement. The structure of Na-AlSi-NAT, an aluminosilicate analogue of Na-GaSi-NAT, was used as a starting model.[13]

No evidence of a second water position (OW2) was found. Addition of a second set of oxygen and/or deuteriums to the structure based on the positions given by Colligan *et. al.* for superhydrated Na-AlSi-NAT.[6] Addition of OW2 water gave chemically unreasonable results and caused significant divergence of the calculations. Evidence from these diffraction data suggest one of two possibilities 1) there is no OW2 water present in the sample studied 2) that the OW2 site is disordered. The fits are shown in Figures 20 and 21 and summary of the refinement variables can be seen in Table 11.

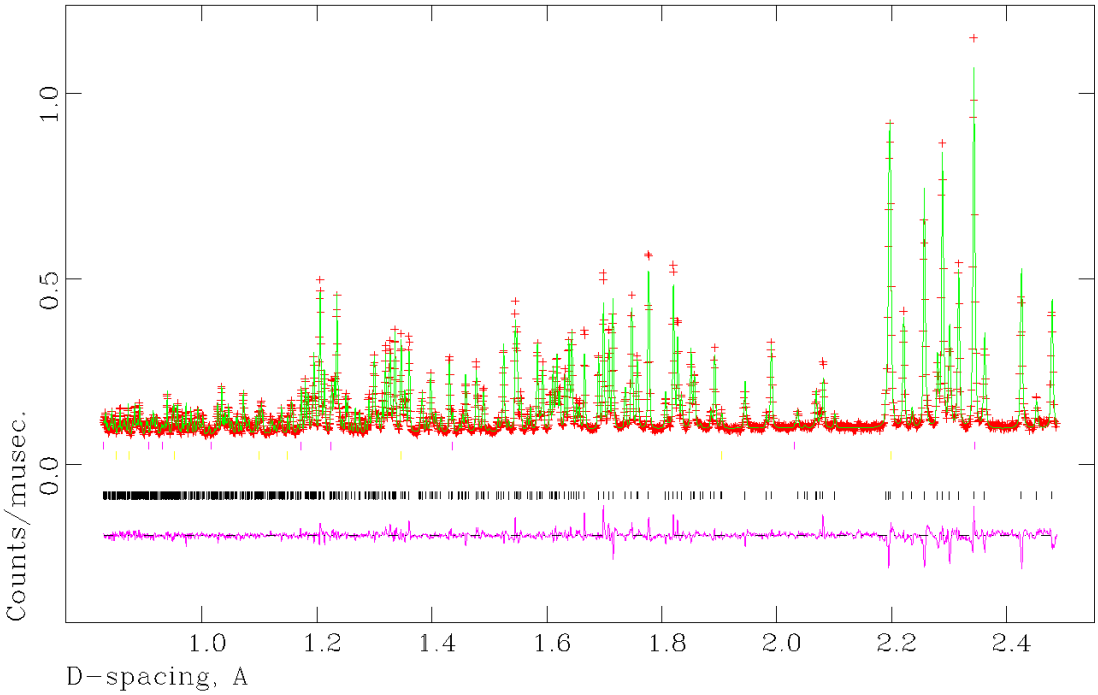

Figure 18: Rietveld refinement of Orthorhombic Ga-NAT (bank 1, 168 degrees).

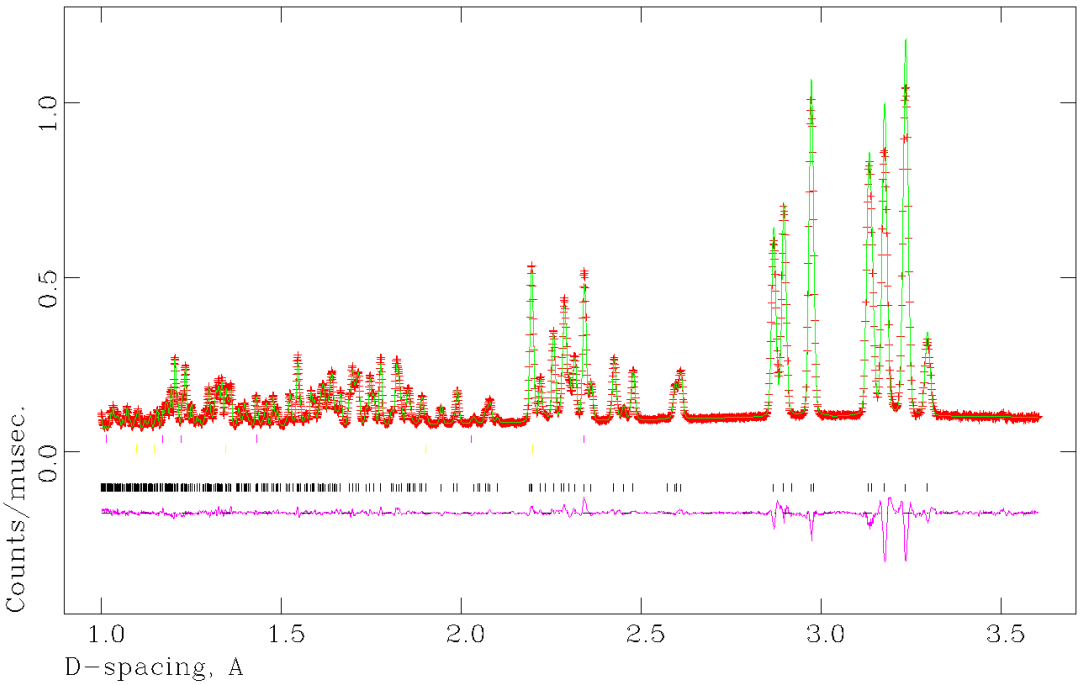

Figure 19: Rietveld refinement orthorhombic Ga-NAT (bank 2, 90 degrees).

Table 11: Final refined atomic coordinates of orthorhombic Ga-NAT.

Bank		168	90
Ref		Orth 168H	1 bank D
χ^2		6.151	101.4
R_{F2}		0.0578	0.0762
R_{wp}		0.0529	0.0374
Rp		0.0470	0.0349
Cell parameters	*a*	18.40081(28)	18.4060(33)
	b	18.88817(28)	18.8867(34)
	c	6.66055(10)	6.6609(12)
volume		2314.93(6)	2315.5(7)
Si1	*x*	0	0
8a	*y*	0	0
	z	0	0
	U_{iso}*100	0.65(5)	0.66(6)
Si2	*x*	0.15189(26)	0.15099(24)
16b	*y*	0.21162(23)	0.20980(23)
	z	0.6174(13)	0.6120(12)
	U_{iso}*100	0.65(5)	0.66(6)
Ga	*x*	0.03608(14)	0.03624(14)
16b	*y*	0.09328(15)	0.09326(13)
	z	0.6134(11)	0.6099(11)
	U_{iso}*100	0.65(5)	0.66(6)
O1	*x*	0.02022(20)	0.01914(19)
16b	*y*	0.06913(19)	0.06857(18)
	z	0.8729(14)	0.8705(12)
	U_{iso}*100	1.68(5)	1.59(5)
O2	*x*	0.06831(19)	0.06764(19)
16b	*y*	0.18431(20)	0.18502(17)
	z	0.6039(14)	0.6022(13)
	U_{iso}*100	1.68(5)	1.59(5)
O3	*x*	0.10100(23)	0.10048(21)
16b	*y*	0.03337(21)	0.03243(17)
	z	0.5007(13)	0.5010(11)
	U_{iso}*100	1.68(5)	1.59(5)

O4 *16b*	*x*	0.20323(21)	0.20322(17)
	y	0.15093(22)	0.15153(19)
	z	0.7157(13)	0.7110(11)
	U_{iso}*100	1.68(5)	1.59(5)
O5 *16b*	*x*	0.18033(20)	0.18196(17)
	y	0.23039(20)	0.22978(18)
	z	0.3917(13)	0.3867(12)
	U_{iso}*100	1.68(5)	1.59(5)
Na *16b*	*x*	0.22110(31)	0.21987(25)
	y	0.03063(30)	0.03053(25)
	z	0.6141(17)	0.6100(15)
	U_{iso}*100	1.65(14)	1.14(15)
OW1 *16b*	*x*	0.05554(29)	0.05679(25)
	y	0.18941(26)	0.18815(24)
	z	0.1101(14)	0.1098(14)
	U_{iso}*100	3.48(12)	3.31(12)
D11 *16b*	*x*	0.05038(28)	0.04940(22)
	y	0.14379(27)	0.14516(22)
	z	0.0362(13)	0.0361(12)
	U_{iso}*100	5.01(11)	4.94(11)
D12 *16b*	*x*	0.10249(30)	0.10197(24)
	y	0.18886(26)	0.18904(21
	z	0.1663(14)	0.1647(12)
	U_{iso}*100	5.01(11)	4.94(11)

3.7.2 Tetragonal Ga-NAT

Experiments performed at room temperature using tetragonal gallosilicate natrolite gave patterns with significantly broadened peaks (see Figure 20 a). The data collected for this sample was unrefinable due to this. HRPD data was also collected at low temperature (20 K) in an effort to reduce this peak broadening; but with little success (see Figure 20 b).

Cooling the sample gave some resolution of peaks, with a clear splitting occurring at 2.9 Å. However, this resolution was not enough to allow for structural refinement; so at this point the crystal structure of tetragonal Ga-NAT remains unresolved (a problem which is addressed in some detail in Chapters 4 and 5).

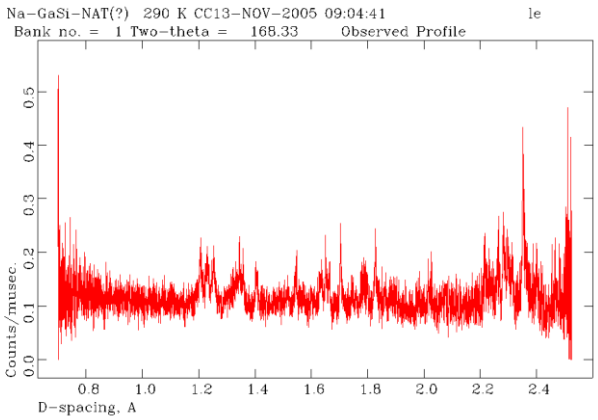

Bank: 168 degrees

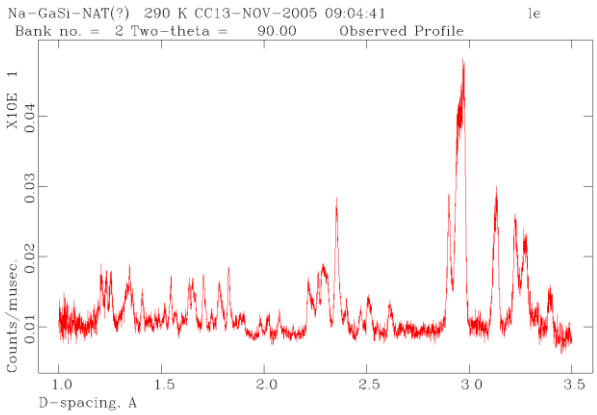

Bank: 90degrees

A)

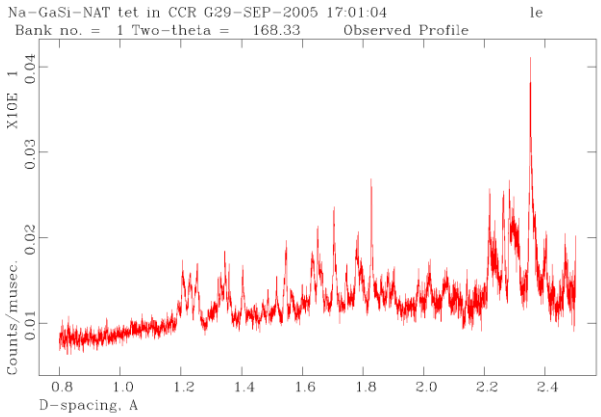

Bank: 168 degrees

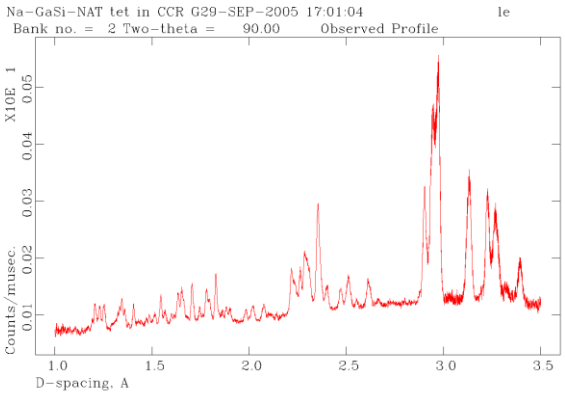

Bank: 90 degrees

B)

Figure 20: Raw plots of HRPD neutron data for tetragonal Ga-NAT, from the 90 ad 168 degree banks. A) data collected at 290 K, B) data collected at 20 K. Plots demonstrate significant peak broadening even with cooling.

3.8 Conclusions

Synthetic gallosilicate analogues of aluminosilicate natrolite can be successfully synthesised according to the method outlined by Hong *et. al.*[4,9] Phase impurities can be minimised by increasing the reaction time to 136 hrs and 96 hrs for orthorhombic and tetragonal gallosilicate natrolite respectively. The resulting gallosilicates can be indexed with space groups *Fdd2* and *I-42d* and cell volumes 2325.993(40) $Å^3$ and 1170.505(14) for orthorhombic and tetragonal gallosilicate natrolite respectively.

SEM EDX analysis and Si NMR were used to investigate Si/Ga ratio. Both show similar values of approximately 1.5for each gallosilicate. SEM EDX gave a chemical composition close to ideal ($Na_{16}Ga_{16}Si_{24}O_{80}$ and $Na_8Ga_8Si_{12}O_{40}$ for orthorhombic and tetragonal respectively). TGA data suggests that it is unlikely that there is any significant OW2 water present at ambient pressure but (for tetragonal in particular) there is a large amount of surface water. TGA data gave unit cell water values close to ideal ($16H_2O$ and $8H_20$ for orthorhombic and tetragonal respectively).

HRPD experiments allowed Rietveld refinement of data collected for orthorhombic gallosilicate. Refinement quality was limited but did confirm that there was no OW2 content at ambient pressure. Data collected for tetragonal gallosilicate gave broad overlapping peaks and was unrefinable. The poor quality of these data could be due to sample impurity, inadequate sample deuteration or structural flexibility/distortions. The nature of the gallosilicate frameworks is discussed in detail in the following chapters (4 and 5).

[1] Hong S. B.; Lee S.-H.; Shin C.-H.; Woo A. J.; Alvarez L. J.; Zicovich-Wilson C. M.; Camblor M. A. 'In Situ Disorder-Order Transformation in Synthetic Gallosilicate Zeolites with the NAT Topology' **2004.** *J. Am. Chem. Soc*. *126*(42). 13742-13751.

[2] Paik W.C.; Camblor M.A.; Hong S.B. 'Microporous gallosilicate TNU materials and their implications for the synthesis of low-silica molecular sieves' **2001.** *Studies in Surface Science and Catalysis*. *135*. 244.

[3] Lee Y.; Hriljac J. A.; Kim S. J.; Hanson J. C.; Vogt T. 'Pressure-induced hydration at 0.6 GPa in a synthetic Gallosilicate zeolite' **2003** *J. Am. Chem. Soc. 125*. 6036-6037.

[4] Hong S. B.; Kim S. H.; Kim Y. G.; Kim Y. C.; Barrett P. A.; Camblor M. A. 'Synthesis of microporous gallosilicates with the CGS topology' **1999.** *J. Mater. Chem. 9*. 2287.

[5] Kim S. H.; Kim S. D.; Kim Y. C.; Kim C. S.; Hong S. B. 'Synthesis and characterization of Ga-substituted MER-type zeolites.' **2001.** *Microporous and Mesoporous Materials*. *42(1)*. 121-129.

[6] Colligan M.; Lee Y.; Vogt T.; Celestian A. J.; Parise J. B.; Marshall W. B.; Hriljac J. A. 'High-pressure neutron diffraction study of superhydrated natrolite' **2005.**
J. Phys. Chem. B. 109. 18223-18225.

[7] Lee Y.; Vogt T.; Parise J. B.; Hriljac J. A. 'Pressure-induced hydration in zeolite Tetranatrolite' **2006**. *American Mineralogist*. *91*. 247-251.

[8] Cho H. H.; Kim S. H.; Kim Y. G.; Kim Y. C.; Koller H.; Camblor M. A.; Hong S. B. 'Synthesis and Characterization of Gallosilicate Molecular Sieves with High Gallium Contents: Examples of Structure Direction Exerted by Gallium' **2000**. *Chem. Mat. 12*. 2292 – 2300.

[9] Hong S. B.; Lee S.-H.; Shin C.-H.; Woo A. J.; Alvarez L. J.; Zicovich-Wilson C. M.; Camblor M. A. 'In Situ Disorder-Order Transformation in Synthetic Gallosilicate Zeolites with the NAT Topology' **2004.** *J. Am. Chem. Soc*. *126(42).* 13742-13751.

[10] Lippmaa E.; Maegi M.; Samoson A.; Tarmak M.; Engelhardt G. 'Investigation of the structure of zeolites by solid-state high-resolution silicon-29 NMR spectroscopy' **1981** *J. Am. Chem. Soc. 103*. 4992 – 4996.

[11] Neuhoff P. S.; Kroeker S.; Du L. S.; Fridriksson T.; Stebbins J. F. 'Order/disorder in natrolite group zeolites: A ^{29}Si and ^{27}Al MAS NMR study' **2002.** *Am. Mineral*. *87*. 1307-1320.

[12] Artioli G.; Smith J. V.; Kvick Å. 'Neutron diffraction study of natrolite, $Na_2Al_2Si_3O_{10}.2H_2O$, at 20 K' **1984.** *Acta Cryst. C40*. 1658-1662.

[13] Artioli G.; Smith J. V.; Kvick Å. 'Neutron diffraction study of natrolite, $Na_2Al_2Si_3O_{10}.2H_2O$, at 20 K' **1984** *Acta. Cryst. C40.* 1658-1662.

CHAPTER FOUR

High Pressure Powder Neutron Diffraction of Gallosilicate Natrolite

4.1 High Pressure Neutron Diffraction Results

To elucidate the ambient pressure models and the high pressure structural changes which occur in both the tetragonal and the orthorhombic gallosilicate natrolite, high pressure neutron diffraction studies were performed. One of the benefits of using neutron diffraction is the detection of hydrogen, consequently these studies should resolve the hydrogen bonding network within the gallosilicate pores.

High pressure neutron diffraction experiments were performed at the ISIS facility, Rutherford Appleton Laboratory; using the PEARL beam line. Powdered samples were deuterated by hydrothermal treatment with D_2O, and successful D/H exchange confirmed by FTIR and mass spectrometery. See chapter 2 for full details of equipment and sample preparation.

Ambient pressure data were collected with the sample in a thin-walled vanadium can (6mm diameter). High pressure experiments were performed using a Paris-Edinburgh cell.[1] Each high pressure diffraction pattern was collected over a 10 hour period. Analysis was performed by the Rietveld method using the EXPGUI GSAS program package.

A water containing pressure medium was required. An optimum mixture of perdeuterated methanol and water 1:1 (v/v). As a consequence of this, we see the emergence of ice phases during high pressure experiments. These phases have been added to refinement fits where appropriate, the occurrence of which is displayed in Table 1.

Table 1: Ice phases present during high pressure experiments.

	Pressure (GPa)		
	0.74	2.26	2.3
Ice IV	X		
Ice VII		X	X

4.1.1 Orthorhombic Gallosilicate Natrolite

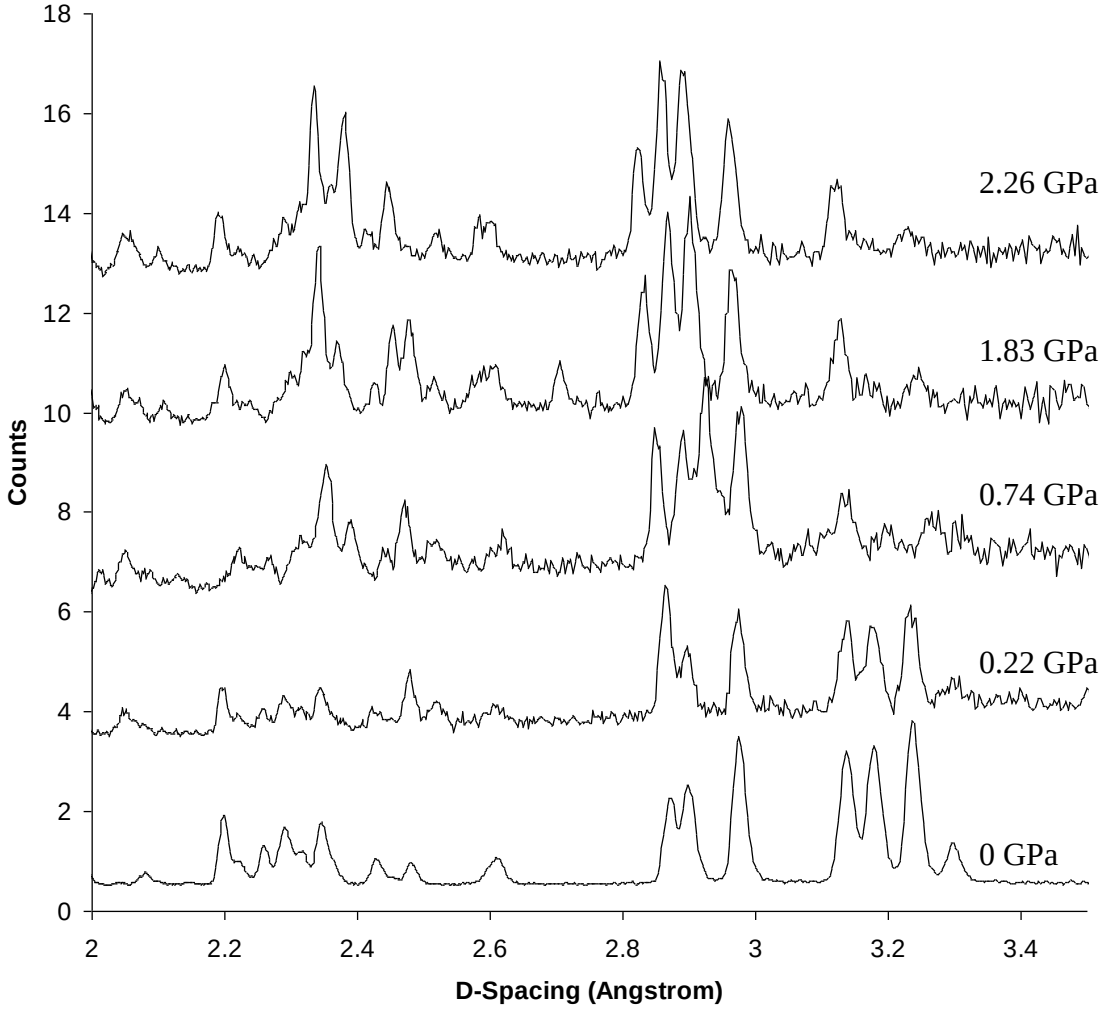

Figure 1: Neutron diffraction patterns recorded for orthorhombic gallosilicate natrolite at ambient and high pressures.

The raw data displayed in Figure 1 were analysed by Rietveld refinement using aluminosilicate natrolite as a starting model[2]. In all refinements (unless otherwise specified), the restraints/constraints listed in Table 2 were applied. These constraints could not be removed without incurring some unreasonable bond distances and angles. The atom positions, isotropic temperature factors, cell parameters and (where applicable)

fractional site occupancy were allowed to vary. Peak shape fitting was by refinement of sig-1 and gam-1 profile parameters.

Table 2: General refinement constraints. *

	Constrained Species	Value
U_{iso}	T atoms	Linked species
	Oxygen (framework)	
	Oxygen (water)	
	Deuterium	
Fractional Occupancy	OW1=D11=D12	1
	OW2=D20=D22	≤1
Bond length (Å)	Ga-O	1.80(2)
	Si-O	1.60(2)
	OW1-D11	1.00(2)
	OW1-D12	1.00(2)
	OW2-D22	1.00(2)
	OW2-D20	1.00(2)
	D11-D12	1.63(2)
	D22-D20	1.63(2)

*Weights in parentheses.

4.1.1.1 Ambient Pressure Refinement

Ambient pressure experiments were performed in a vanadium can, therefore vanadium has been included as a second phase. The sample appears to be fully deuterated. No hydrogen contribution to the deuterium sites was found during refinement modelling, this is supported by the occurrence of low background levels in the powder pattern.

Modelling the Water Content and Bonding at Ambient Pressure

Refinement models (Table 3), assume that the water site OW1 is fully occupied, as this is seen throughout the natrolite family. Thermogravimetric analysis (chapter 3), suggests that we may see partial occupancy of the OW2 site at ambient pressures. A starting model for the atomic coordinates of the OW2, D20 and D22 sites was taken from the superhydrated aluminosilicate structure as reported by Colligan et al.[3]

In model 1 the fractional occupancy of OW2 and associated deuteriums, were refined. This starting model yields negative isotropic displacement factors (U_{iso}), for both deuterium sites D22 & D20. To achieve a chemically sensible model, all Uiso factors should have a reasonable, positive value; thus model 2 shows selected refinement output when these U_{iso} factors are manually set to sensible value (0.01). By allowing unconstrained occupancy refinement of all of the atoms associated with water 2, we can see that all deuterium sites refine to values similar to the associated OW2 occupancy (model 3); suggesting that all D sites are ordered. Based upon these results, model 2 appears to be the most chemically sensible Rietveld fit even though it has a slightly higher χ^2. The final Rietveld profile plot for ambient pressure is shown in Figure 2 and full details are given in Table 4.

Table 3: Modelling order/disorder in deuterium sites.*

Bonding model		1	2	3
Reference		VCH7	VCH8	VCH9
Comment		Ordered D22/D20	Ordered D22/D20 U_{iso} correction	Occupancy of D sites
Fractional occupancy constraints		OW2=D22=D20	OW2=D22=D20	
Uiso constraints		OW2=OW1 D11=D12 D22=D20	OW2=OW1 D11=D12 D22=D20	OW2=OW1 D11=D12 D22=D20
χ^2		2.170	2.191	2.171
R_{F2}		0.0631	0.0651	0.0630
OW1	Occ	1	1	1
	U_{iso} *100	2.192(106)	2.18(11)	2.191(106)
D11	Occ	1	1	1
	U_{iso} *100	4.52(12)	4.51(13)	4.53(12)
D12	Occ	1	1	1
	U_{iso} *100	4.52(12)	4.51(13)	4.53(12)
OW2	Occ	0.041(3)	0.048(4)	0.0413
	U_{iso} *100	2.192(106)	2.18(11)	2.191(106)
D22	Occ	0.041(3)	0.048(4)	0.045(4)
	U_{iso} *100	-1.73(27)	1	-1.69(28)
D20	Occ	0.041(3)	0.048(4)	0.040(6)
	U_{iso} *100	-1.73(27)	1	-1.69(28)

*Weights in parentheses.

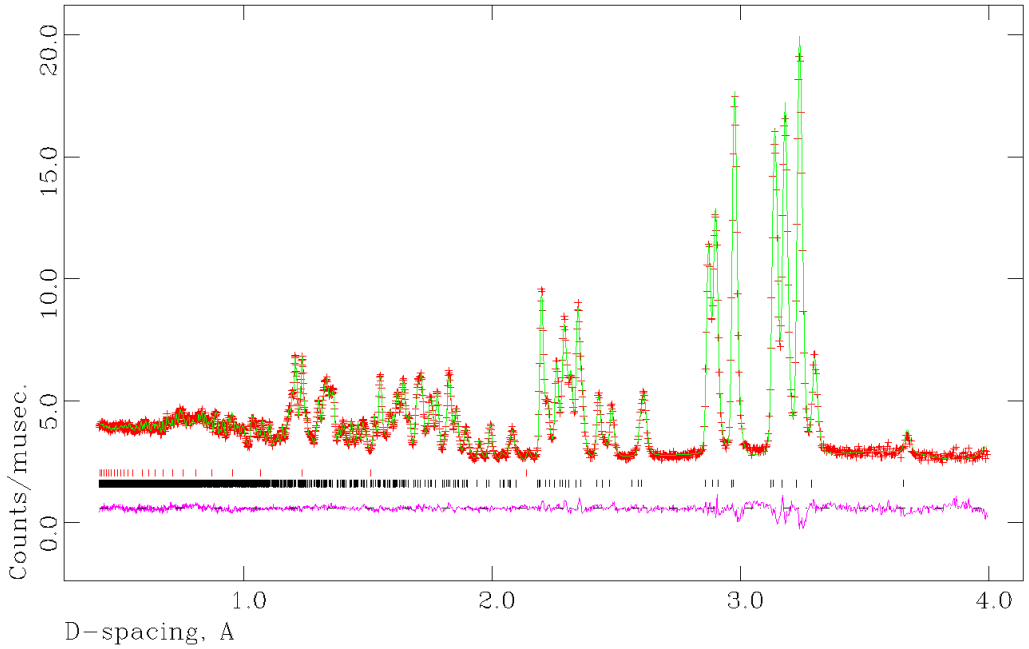

Figure 2: Rietveld refinement of orthorhombic Gallosilicate at ambient pressure. Vertical tick marks indicate allowed reflections for each phase: Ga-NAT (black); Vanadium (red).

4.1.1.2 High Pressure Refinement

High pressure experiments were performed in a Paris-Edinburgh cell, therefore nickel and tungsten carbide phases have been added. Lead was used as a pressure marker (the cell parameters of which determine the pressure inside the sample cavity), and has also been added as a phase. Pressure was applied to the cell via a piston pump, at values of 7, 12, 22 and 26 tonnes, inclusive.

At high pressure we see the formation of ice phases (from the water containing pressure medium). These phases have been added to the refinement where appropriate. Details of the type of ice phases occurring in both the orthorhombic and tetragonal gallosilicate samples, during high pressure runs are listed in Table 1. Relative phase ratios are included in Table 4.

Refinement of neutron data for pressure points, 0.22, 0.74, 1.83 and 2.26 GPa showed good fits. An example of a refinement profile plot is given in Figure 3, all others in the high pressure series are given in appendices 1.1. All have ordered D22 and D20 sites. Any negative U_{iso} factors were corrected to 0.01, although these are a bit higher than the T-site values that successfully refined they are reasonable for a zeotype. A summary of final refined atomic coordinates and criteria of fit values are displayed in Table 4, with selected bond distances and angles given in Table 5.

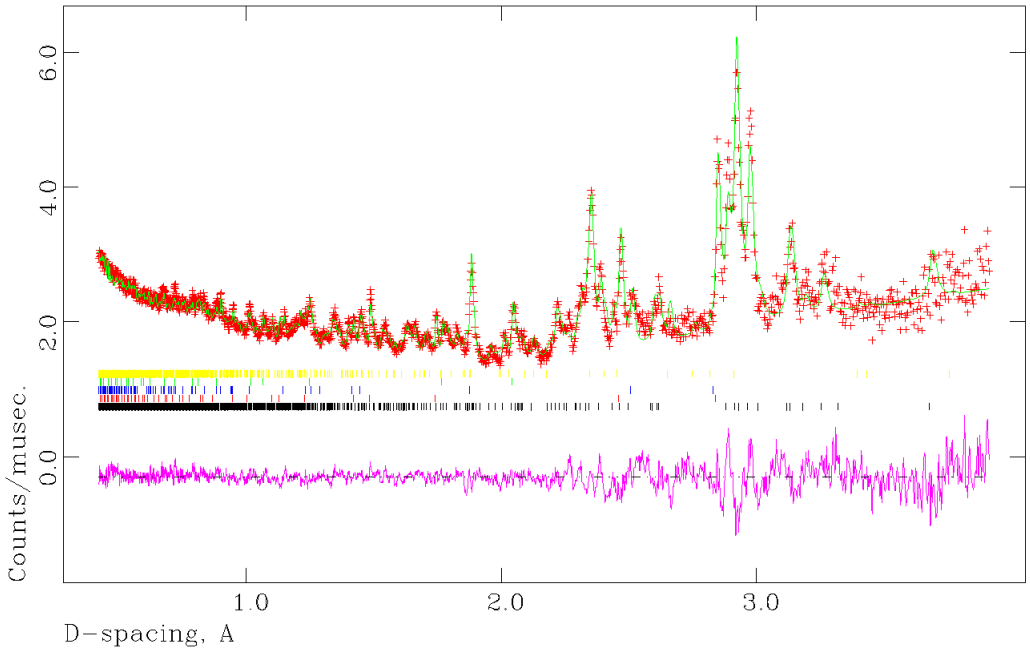

Figure 3: Rietveld refinement of superhydrated orthorhombic gallosilicate at 0.74 GPa. Vertical tick marks indicate allowed reflections for each phase: Ga-NAT (black); Lead (red); Tungsten Carbide (blue); Nickel (green); Ice IV (yellow).

Table 4: Final refinement data and atomic coordinates for orthorhombic Ga-NAT (*Fdd2*) at ambient and high pressures.*

Reference		VCH8	7e2j	12M13	22D6	26e6
applied pressure (tons)		0	7	12	22	26
Internal Pressure (GPa)		0	0.22	0.74	1.83	2.26
Phase ratios	Ga-NAT	1	1	1	1	1
	V	77.63				
	Pb		2.47	2.79	2.71	2.54
	WC		10.34	11.76	12.91	12.94
	Ni		0.75	0.92	0.91	1.01
	Ice IV			0.91		
	Ice VII					4.40
χ^2		2.191	2.226	2.81	2.375	2.503
R_{F2}		0.0651	0.3173	0.0732	0.4223	0.4273
R_{wp}		0.0209	0.0322	0.0378	0.0346	0.034
R_p		0.0228	0.0441	0.0546	0.0464	0.0407
cell parameters	*a*	18.3914(5)	18.3770(26)	18.523(4)	18.3652(23)	18.2965(22)
	b	18.8700(5)	18.8534(26)	19.1124(32)	18.9312(19)	18.8563(20)
	c	6.65548(16)	6.6518(8)	6.6428(12)	6.6242(8)	6.6172(8)
volume		2309.75(11)	2304.6(5)	2351.7(8)	2303.1(5)	2283.0(5)
Si1 *8a*	*x*	0	0	0	0	0
	y	0	0	0	0	0
	z	0	0	0	0	0
	U_{iso}*100	0.12(4)	0.21(15)	1	1	1
Si2 *16b*	*x*	0.15084(29)	0.1443(9)	0.1571(9)	0.1573(8)	0.1578(7)
	y	0.21027(28)	0.2094(9)	0.2052(9)	0.2088(8)	0.2094(7)
	z	0.6124(15)	0.613(4)	0.634(4)	0.640(4)	0.6466(34)
	U_{iso}*100	0.12(4)	0.21(15)	1	1	1
Ga *16b*	*x*	0.03600(17)	0.0302(6)	0.0390(6)	0.0372(5)	0.0392(4)
	y	0.09325(16)	0.0931(6)	0.0888(5)	0.0927(5)	0.0929(4)
	z	0.6097(13)	0.613(4)	0.623(4)	0.6236(33)	0.6255(29)
	U_{iso} *100	0.12(4)	0.21(15)	1	1	1
O1 *16b*	*x*	0.01966(25)	0.0172(10)	0.0498(9)	0.0530(10)	0.0496(10)
	y	0.06952(24)	0.0736(8)	0.0577(9)	0.0569(9)	0.0562(9)
	z	0.8695(15)	0.874(4)	0.879(4)	0.879(4)	0.877(4)
	U_{iso}*100	0.75(4)	1.334(149)	0.16(9)	0.94(11)	1.27(16)
O2 *16b*	*x*	0.06770(22)	0.0615(9)	0.0795(9)	0.0703(8)	0.0709(9)
	y	0.18337(20)	0.1812(8)	0.1779(10)	0.1797(9)	0.1826(9)
	z	0.6020(15)	0.634(5)	0.581(5)	0.640(5)	0.622(5)
	U_{iso}*100	0.75(4)	1.334(149)	0.16(9)	0.94(11)	1.27(16)
O3 *16b*	*x*	0.10009(25)	0.0977(10)	0.0931(11)	0.0959(10)	0.0936(11)
	y	0.03375(22)	0.0325(9)	0.0378(9)	0.0413(8)	0.0402(8)
	z	0.5016(14)	0.518(4)	0.466(5)	0.458(5)	0.460(4)

	U_{iso}*100	0.75(4)	1.334(149)	0.16(9)	0.94(11)	1.27(16)
	x	0.20388(21)	0.1985(9)	0.2015(9)	0.1996(9)	0.2004(9)
O4	*y*	0.15057(24)	0.1492(9)	0.1480(10)	0.1528(9)	0.1503(10)
16b	*z*	0.7146(14)	0.719(5)	0.760(4)	0.760(4)	0.775(4)
	U_{iso}*100	0.75(4)	1.334(149)	0.16(9)	0.94(11)	1.27(16)
	x	0.17961(21)	0.1804(9)	0.1933(9)	0.1959(10)	0.1955(11)
O5	*y*	0.23066(24)	0.2339(9)	0.2200(10)	0.2120(9)	0.2126(10)
16b	*z*	0.3874(15)	0.404(4)	0.416(4)	0.417(4)	0.418(4)
	U_{iso}*100	0.75(4)	1.334(149)	0.16(9)	0.94(11)	1.27(16)
	x	0.2215(4)	0.2300(13)	0.2234(21)	0.2357(20)	0.2239(24)
Na	*y*	0.03125(33)	0.0334(11)	0.0398(15)	0.0279(19)	0.0273(23)
16b	*z*	0.6115(20)	0.610(5)	0.557(7)	0.615(9)	0.601(9)
	U_{iso}*100	1.37(16)	0.2(4)	0.8(8)	3.4(12)	5.1(14)
	x	0.05561(31)	0.0478(5)	0.0546(12)	0.0462(10)	0.0545(10)
OW1	*y*	0.18864(27)	0.1816(4)	0.1822(13)	0.1823(10)	0.1791(10)
16b	*z*	0.1057(17)	0.136(4)	0.105(5)	0.140(5)	0.110(4)
	U_{iso}*100	2.18(11)	1	0.90(25)	1.06(23)	0.84(26)
	x	0.04997(30)	0.0497(9)	0.0518(13)	0.0509(12)	0.0563(12)
D11	*y*	0.14295(31)	0.1422(7)	0.1412(11)	0.1409(10)	0.1401(10)
16b	*z*	0.0307(14)	0.041(4)	0.024(4)	0.049(4)	0.027(4)
	U_{iso}*100	4.51(13)	0.87(19)	2.2(4)	3.36(20)	4.10(50)
	x	0.10133(31)	0.0949(8)	0.1018(12)	0.0920(12)	0.0977(12)
D12	*y*	0.18876(30)	0.1955(7)	0.1974(10)	0.1960(10)	0.1952(11)
16b	*z*	0.1644(15)	0.193(4)	0.119(5)	0.185(5)	0.166(5)
	U_{iso}*100	4.51(13)	0.87(19)	2.2(4)	3.36(20)	4.10(50)
	x	0.13730(435)	0.1442(15)	0.1357(11)	0.1852(9)	0.1839(9)
	y	0.10096(306)	0.0821(18)	0.0844(12)	0.0766(10)	0.0768(10)
OW2	*z*	0.0032(114)	0.013(6)	0.061(5)	0.132(5)	0.127(5)
16b	U_{iso}*100	2.18(11)	1	0.90(25)	1.06(23)	0.84(26)
	Occ	0.048(4)	0.2817	1	1	1
	x	-0.17063(397)	-0.1159(17)	-0.1835(14)	-0.1538(10)	-0.1519(13)
	y	-0.07564(385)	-0.1064(15)	-0.0778(15)	-0.0773(11)	-0.0805(11)
D22	*z*	0.0965(113)	0.127(6)	0.146(5)	0.259(4)	0.245(5)
16b	U_{iso}*100	1	1	4.1(5)	1.71(20)	2.97(34)
	Occ	0.048(4)	0.2817	1	1	1
	x	-0.11084(394)	-0.1100(17)	-0.1540(14)	-0.1435(11)	-0.1452(13)
	y	-0.06491(385)	-0.0562(17)	-0.0756(15)	-0.0789(10)	-0.0723(12)
D20	*z*	-0.0841(92)	-0.077(5)	-0.079(4)	0.032(4)	0.017(5)
16b	U_{iso}*100	1	1	4.1(5)	1.71(20)	2.97(34)
	Occ	0.048(4)	0.2817	1	1	1

* Weights in parenthesis

Table 5: Bond distances and angles of orthorhombic Ga-NAT at ambient and high pressures.*

	Pressure				
	0	0.22	0.74	1.83	2.26
Si Tetrahedra					
Bond Length (Å)					
SI1_O1 × 2	1.615(6)	1.652(14)	1.649(15)	1.658(16)	1.614(15)
SI1_O5 × 2	1.626(6)	1.665(15)	1.626(16)	1.650(16)	1.649(16)
SI2_O2	1.613(6)	1.618(18)	1.569(20)	1.691(19)	1.676(19)
SI2_O3	1.668(6)	1.729(18)	1.671(19)	1.628(17)	1.580(17)
SI2_O4	1.638(6)	1.665(19)	1.605(21)	1.535(18)	1.605(19)
SI2_O5	1.634(7)	1.612(19)	1.622(20)	1.641(18)	1.666(17)
Ga Tetrahedra					
Bond Length (Å)					
GA_O1	1.811(5)	1.792(17)	1.808(18)	1.847(17)	1.813(18)
GA_O2	1.799(4)	1.763(15)	1.882(19)	1.758(16)	1.789(17)
GA_O3	1.780(5)	1.799(16)	1.743(17)	1.819(18)	1.782(18)
GA_O4	1.797(5)	1.787(16)	1.805(16)	1.778(16)	1.760(17)
T-O-T Inter-Chain Bond Angle					
SI2_O2_GA	127.14(31)	127.5(14)	133.4(16)	129.3(11)	126.3(11)
Na Environment					
Bond Length/distances (Å)					
NA_O2	2.477(8)	2.452(32)	2.75(4)	2.52(5)	2.63(5)
NA_O2	2.630(9)	2.559(33)	2.79(4)	2.60(4)	2.48(5)
NA_O3	2.351(8)	2.506(32)	2.49(4)	2.78(4)	2.57(5)
NA_O4	2.376(8)	2.372(27)	2.50(4)	2.64(5)	2.62(6)
NA_NA	3.683(6)	3.632(18)	3.783(32)	3.516(26)	3.59(4)
NA_OW1	2.369(11)	2.049(27)	2.09(4)	2.01(5)	2.32(5)
NA_OW1	2.438(10)	2.707(24)	2.90(4)	2.63(5)	2.58(6)
NA_OW2	3.31(8)	3.24(31)	3.52(6)	2.46(5)	2.59(5)
Selected Bond Angles (°)					
OW1_NA_OW1	141.67(29)	146.7(11)	138.6(16)	153.6(20)	147.1(21)
OW1_NA_OW2				90.5(18)	84.2(17)
OW1_NA_OW2				63.1(11)	62.9(12)
Water Bonding					
Bond Length (Å)					
OW1_D11	1.002(7)	0.978(13)	0.949(19)	0.991(18)	0.918(18)
OW1_D12	0.927(7)	0.981(13)	0.926(21)	0.928(20)	0.923(20)
OW2_D22	0.994(29)	1.028(23)	1.057(19)	1.024(21)	0.980(21)
OW2_D20	1.018(28)	0.997(23)	1.004(20)	1.012(20)	1.019(21)
Bond Angles (°)					

D11_OW1_D12	107.8(7)	115.0(16)	111.6(25)	109.7(23)	118.1(27)
D22_OW2_D20	109.(4)	110.0(29)	101.1(25)	96.5(18)	99.3(19)
Hydrogen Bonding & Related Distances†					
D11…..O1	1.839(8)	1.806(22)	1.867(29)	1.950(26)	1.872(27)
D11…..OW2	1.80(8)	2.083(35)	1.912(33)		
D20…..O1	1.71(7)	1.765(34)	1.980(31)	1.990(26)	2.002(27)
OW1…..D22		1.893(29)			
D12…..OW2	2.08(7)				
D22…..O3				1.824(25)	1.934(29)
D20…..O5	2.29(8)	2.18(4)			
D12…..O5	2.213(7)	2.224(20)			
D20…..O4			1.958(30)		

*Weights in parenthesis

† Grey shading: D…..O distances which have exceeded the hydrogen bonding limit (2.3 Å). Distances over 3.0 Å are not reported.

4.1.1.3 Volume Expansion and Superhydration in Orthorhombic Ga-NAT

With the application of hydrostatic pressure we see a number of structural and compositional changes to Ga-NAT, all of which are reversible upon pressure release. These effects include unit cell volume expansion and superhydration, which are facilitated by changes in the chain rotation angle (Ψ) and T-O-T angles. These changes also affect the occurrence and strength of hydrogen bonding.

Upon application of pressure, orthorhombic Ga-NAT exhibits a cell compression as was previously reported using X-rays.[4] A similar trend is seen in a high pressure X-ray study of the aluminosilicate analogue[5]. Although the cell is undergoing compression (from ambient to 0.22 GPa), a gradual filling of the OW2 position is observed as the occupancy changes from 0.048 to 0.282. The pressure dependence of cell volume and OW2 occupancy are shown in Figure 5.

Compression is followed by a sudden and significant increase in cell volume at 0.74 GPa which is accompanied by super-hydration; the occupancy of OW2 increases to 1. This is characteristic of the pressure-induced hydration (PIH) step. A cell volume expansion of 2.04% is observed (1.82% increase compare to V_0). This increase (from V_0) is greater than that given in reports of orthorhombic Ga-NAT (1.5% total, <1% from V_0) [4] and of Al-NAT (2.5% total, ~1% from V_0). [5]

This expansion is due to an increase in the *a*- and *b*-axes (0.79% and 1.37% respectively), with a slight contraction along the *c*-axis (Figure 4). The mechanism by which this expansion occurs is discussed later in this chapter, where chain rotation, pore dimensions and T-O-T angles are considered.

Following the formation of the superhydrated phase, the unit cell (whilst maintaining full OW2 occupancy), progresses down a compression curve as the pressure is increased. The pressure and volume data obtained from this compression curve can be used to fit an

equation of state to the superhydrated phase. In doing so, both the bulk modulus and an extrapolated 'V_0' can be obtained for the superhydrated phase. A value for V_0 would not be possible to collect experimentally due to the reversibility of the pressure-induced hydration step. Results from EoS fitting are discussed in later sections within this chapter.

a)

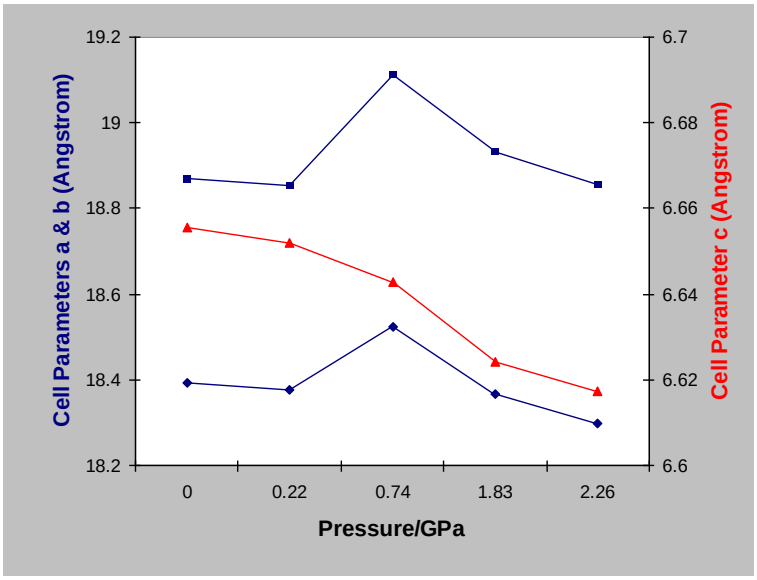

Figure 4: Pressure effect upon unit cell parameters for orthorhombic Ga-NAT.

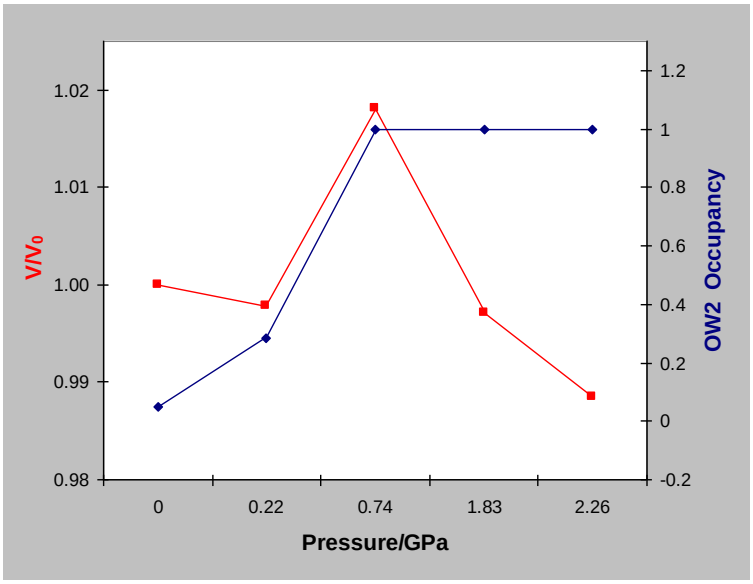

Figure 5: Pressure effect upon normalized volume (V/V_0) and OW2 occupancy for orthorhombic Ga-NAT.

4.1.2 Tetragonal Gallosilicate Natrolite

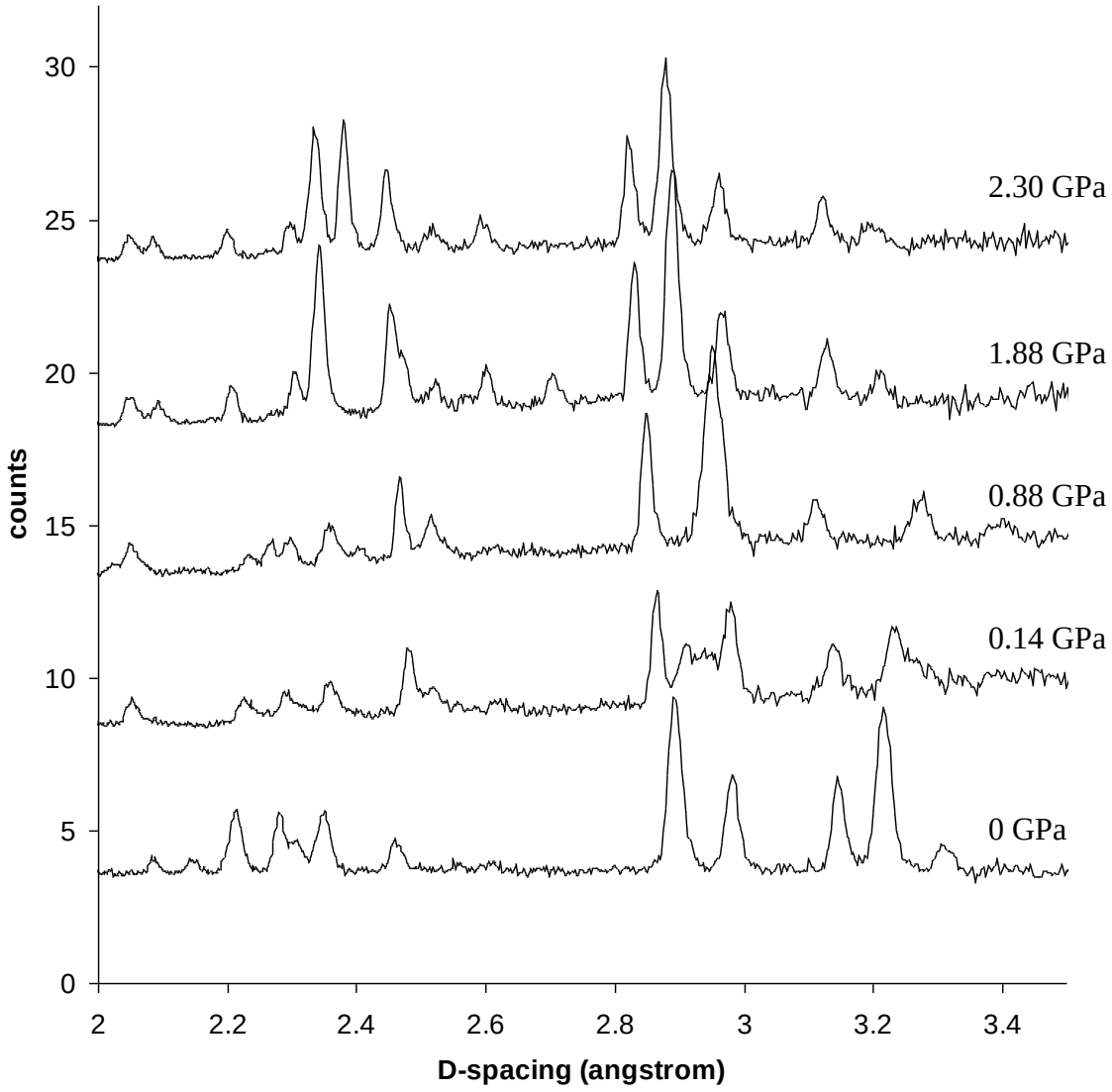

Figure 6: Neutron diffraction patterns recorded for tetragonal gallosilicate natrolite at ambient and high pressures.

The raw data displayed in Figure 6 was analysed by Rietveld refinement using aluminosilicate tetranatrolite as a starting model.[6] The position of D22 was found via Fourier search. In all refinements (unless otherwise specified), the restraints/constraints listed in Table 6 were applied. These constraints could not be removed without incurring

some unreasonable bond distances and angles. The atom positions, isotropic temperature factors, cell parameters and (where applicable) fractional site occupancy were allowed to vary. Peak shape fitting was by refinement of *sig-1* and *gam-1* profile parameters. As the T atom positions are disordered, the occupancy of each was set to match the ideal Si/Ga ratio of 1.5; this ratio was confirmed by compositional analysis using EDX SEM. The Si/Ga disorder over both sites is a key difference in the tetragonal form versus the orthorhombic form.

Table 6: General refinement constraints.*

	Constrained Species	Value
XYZ	T1 atoms	n/a
	T2 atoms	
U_{iso}	T atoms	
	Oxygen (framework)	
	Oxygen (water)	
	Deuterium	
Fractional Occupancy	OW1=D11	1
	OW2=D22	≤1
Bond length (Å)	OW1-D11	1.00(2)
	OW2-D22	1.00(2)
	D11-D12	1.63(2)
	D22-D20	1.63(2)

*Weights in parentheses

4.1.2.1 Ambient Pressure Refinement

The ambient pressure data set was collected with the sample in a vanadium can; therefore vanadium has been included as a second phase. FTIR and mass spectrometry analysis of the sample prior to taking it to ISIS showed complete deuteration of the sample. However, the high background observed in the powder patterns of this sample suggest

that some hydrogen may be present during neutron diffraction experiments. This is likely due to the very fast D/H exchange and could have occurred while loading the sample for the neutron experiments. This will be considered in refinement modelling both at ambient and high pressures.

Modelling the Water Content and Bonding at Ambient Pressure

In the initial refinement (model 1, Table 7) it was assumed that the water site OW1 is fully occupied. Refinement of the occupancy of OW1 gave values slightly above unity; hence this value was set to unity and fixed. It follows that the associated deuterium atoms (D11) must also show full occupancy and this was set to unity. Occupancy of the OW2 site and the associated deuterium atoms (D22) were refined. This starting model yields very high isotropic displacement factors (U_{iso}) for both deuterium sites (D11 and D22).

In model 2, the fractional occupancy constraints are removed, so that the occupancies of D22 do not equal that of OW2 and the occupancies of D11 do not equal that of OW1. This reduces the refined U_{iso}'s, but show deuterium occupancies which are lower than is chemically sensible for water. Evidence from models 1 and 2 combined could suggest that:

a) The sample was not fully deuterated, so the D22 and/or the D11 sites could be partially occupied by hydrogen.
b) The D22 and/or D11 sites are disordered. Unlike the orthorhombic natrolite structure, both D atoms on the same OW atom sit across a mirror plane.

To investigate these possibilities, further bonding models were applied during subsequent Rietveld refinements. Table 8 shows further modelling based upon the assumption that this low deuterium content is indicative of partial hydrogen occupancy at one or both deuterium sites.

Table 7: Modelling water site occupancy and order/disorder*

Bonding model		1	2
File name		VCT1	VCV
Comment		Determination of OW2 and D22 occupancy	Refinement of OW2, D22 and D11 occupancy
U_{iso} constraints		OW1=OW2 D11=D22	OW1=OW2 D11=D22
FRAC constraints		OW2=D22	none
χ^2		1.730	1.823
R_{F2}		0.1297	0.1352
OW1	*Occ*	1	1
	U_{iso} *100	3.12(27)	2.59(27)
D11	*Occ*	1	0.329(37)
	U_{iso} *100	38.1(22)	7.6(19)
OW2	*Occ*	0.210(16)	0.118(22)
	U_{iso} *100	3.12(27)	2.59(27)
D22	*Occ*	0.210(16)	0.092(22)
	U_{iso} *100	38.1(22)	7.6(19)

*Weights in parentheses

Table 8: Modelling partial deuteration at ambient Pressure.* †

Bonding model		3	4
File name		VCN	VCO
Comment		Ordered D22, with partial hydrogen contribution to both D11 and D22 positions	Ordered D22, with partial hydrogen contribution to D11 position only
U_{iso} constraints		OW1=OW2 D11=H11 D22=H22	OW1=OW2 D11=H11
Fractional Occupancy constraints		D11+H11=1 D22+H22=OW2	D11+H11=1 OW2=D22
χ^2		1.623	1.620
R_{F2}		0.1372	0.1340
OW1	*Occ*	1	1
	U_{iso} *100	2.84(27)	2.77(27)
D11	*Occ*	0.561(22)	0.570(23)
	U_{iso} *100	6.9(18)	7.5(18)
H11	*Occ*	0.439(22)	0.430(23)
	U_{iso} *100	6.9(18)	7.5(18)
OW2	*Occ*	0.104(19)	0.121(19)
	U_{iso} *100	2.84(27)	2.77(27)
D22	*Occ*	0.142(23)	0.121(19)
	U_{iso} *100	24.9(130)	13.3(60)
H22	*Occ*	-0.038(43)	
	U_{iso} *100	24.9(130)	

*Weights in parentheses

† XYZU constraints were applied to each H/D site.

From model 3 (Table 8), it is clear that there is no hydrogen contribution to the D22 sites of water 2, since the occupancy of a H22 site is refined to -0.038(43). In this model the D11 site of water 1 shows a considerable hydrogen occupancy (0.439(22)). From these results, model 4 was included with a partial hydrogen occupancy to the D11 site only

(0.430(23)). This model gives a reasonable result but shows very high U_{iso} factors upon the D/H sites. This reflects some disorder due to the poor bonding in the OW2 water molecule, which cannot be localised. Even with high U_{iso} factors model 4 is still deemed the most sensible. The Rietveld profile plot for this model is shown in Figure 7.

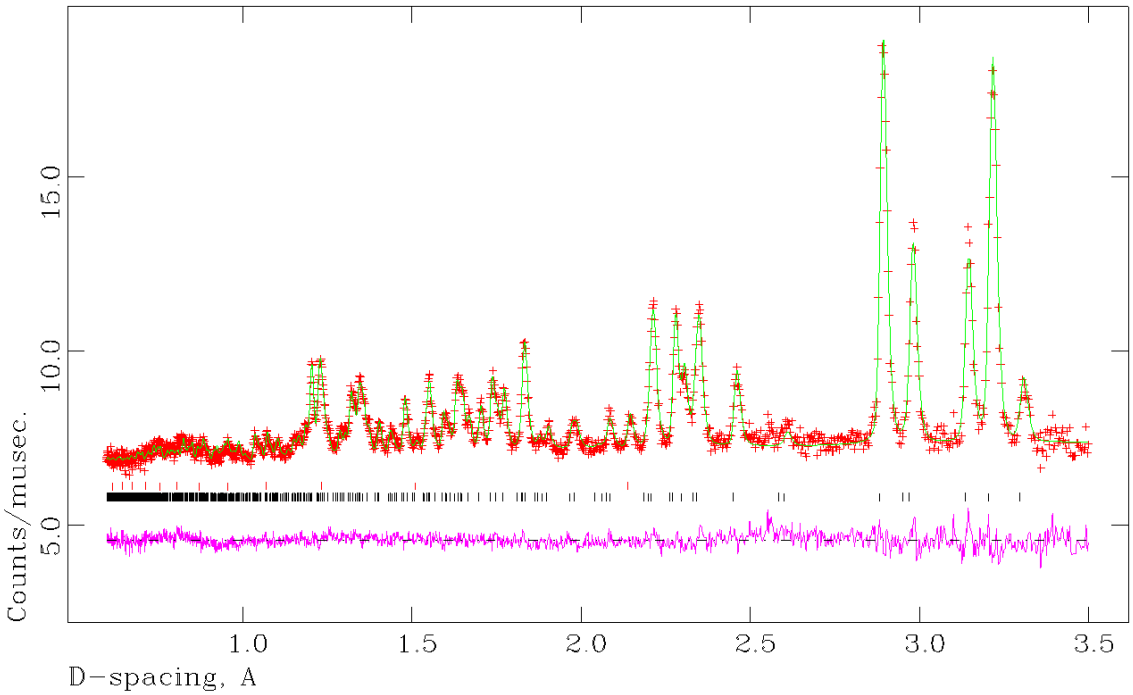

Figure 7: Rietveld refinement of tetragonal gallosilicate at ambient pressure. Vertical tick marks indicate allowed reflections for each phase: Ga-NAT (black); Vanadium (red).

4.1.2.2 High Pressure Refinement

Modelling the Water Content and Bonding at High Pressure

Final Rietveld profile plots for all the pressure points within the high pressure series can be found in appendices 1.1. The profile plot for the superhydrated phase is shown in Figure 8. Refined atomic coordinates and other values are reported in Table 9 with selected bond distances and angles given in Table 10.

At 0.14 GPa we see a broadening of the peaks (Figure 6), as a consequence of this, refinement of these data gave high χ^2 and R_{F2} values. The poor fit and peak broadening we see in the high pressure data collected at 0.14 GPa could be a consequence of slow kinetics during high pressure phase transitions.

As seen in the ambient pressure model, there is hydrogen contribution to the D11 site of water 1; but the occupancy is reduced 0.430(23) to 0.29(5), from ambient pressure to 0.14 GPa. This suggests that there is some water mobility through the structure as some of the H_2O/HOD present at ambient pressure has been exchanged with D_2O from the pressure medium. The high U_{iso} factors observed in the ambient pressure model are reduced at 0.14 GPa indicating increased order in the D/H sites.

At 0.88 GPa superhydration and cell volume expansion is observed and there is no longer a hydrogen contribution to the D11 site of water 1. This evidence supports the idea of increased water mobility at the point of superhydration; as reported for superhydrated aluminosilicate natrolite.[7] The modelling of the 0.88 GPa data gave very high U_{iso} factors for both water sites. A high U_{iso} factor might suggest that bonding is poorer and un-localised at this pressure point, due to increased water mobility. These high U_{iso} factors were set to a reasonable value (0.025).

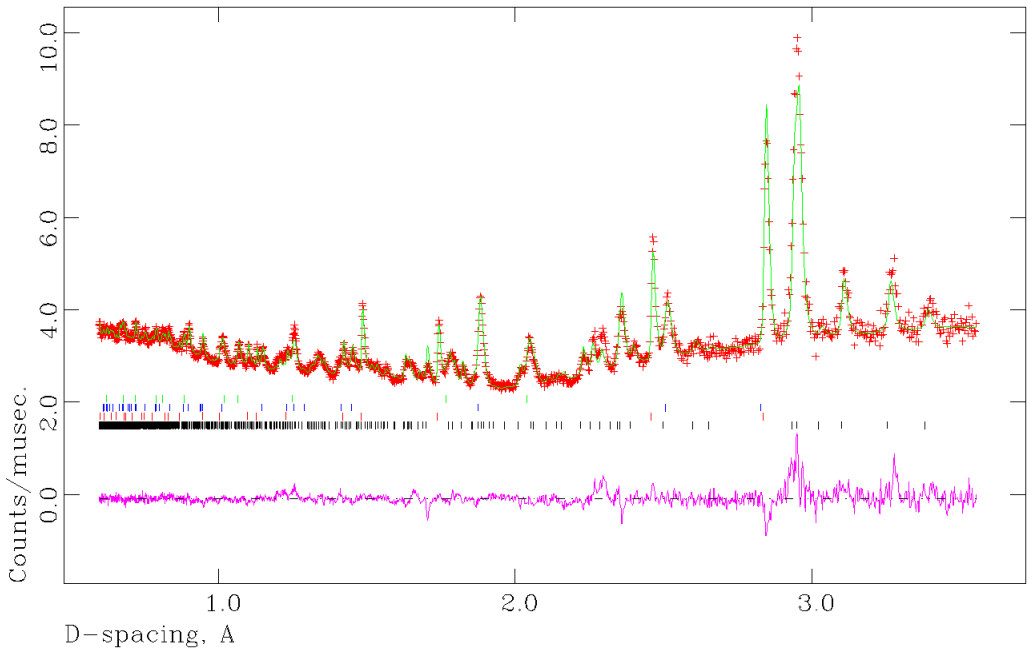

Figure 8: Rietveld refinement of superhydrated tetragonal gallosilicate at 0.88 GPa. Vertical tick marks indicate allowed reflections for each phase: Ga-NAT (black); Lead (red); Tungsten Carbide (blue); Nickel (green).

Refinements of neutron data for pressure points 1.88 and 2.30 GPa showed good fits with no unusually high isotropic temperature factors. All have fully occupied OW2, D11 and D22 positions with no evidence of hydrogen contribution.

Table 9: Final refinement data and atomic coordinates for tetragonal Ga-NAT (I-42d) at ambient and high pressures.*

File name		VCO	7L22	12K17	22D2G	264g
applied pressure (tons)		0	7	12	22	26
Internal pressure (GPa)		0	0.14	0.88	1.88	2.30
Phase ratios	Ga-NAT	1	1	1.00	1.00	1.00
	V	127.250923				
	Pb		1.57340121	3.60	2.57	2.53
	WC		5.27512379	12.64	8.29	8.73
	Ni		0.4925727	1.22	0.63	0.70
	Ice VII					4.51
χ^2		1.619	4.411	2.903	3.833	2.65
R_{F2}		0.1336	0.359	0.1513	0.2933	0.2153
R_{wp}		0.0196	0.0327	0.0267	0.0301	0.0322
R_p		0.0221	0.043	0.0314	0.0371	0.0383
cell parameters	*a*	13.2107(6)	13.3508(33)	13.5606(11)	13.2017(10)	13.1549(11)
	c	6.6683(5)	6.6366(24)	6.5662(8)	6.6231(11)	6.6145(12)
volume		1163.77(12)	1182.9(6)	1207.47(20)	1154.30(23)	1144.66(25)
Si1 *4a*	*x*	0	0	0	0	0
	y	0	0	0	0	0
	z	0	0	0	0	0
	U_{iso}*100	0.22(31)	1	1.69(29)	0.05(20)	1
	Occ	0.6	0.6	0.6	0.6	0.6
Ga1 *4a*	*x*	0	0	0	0	0
	y	0	0	0	0	0
	z	0	0	0	0	0
	U_{iso}*100$_i$	0.22(31)	1	1.69(29)	0.05(20)	1
	Occ	0.4	0.4	0.4	0.4	0.4
Si2 *16e*	*x*	0.0582(6)	0.0557(18)	0.0491(10)	0.0495(11)	0.0481(11)
	y	0.1344(5)	0.1411(14)	0.1285(10)	0.1360(11)	0.1370(12)
	z	0.6240(13)	0.6293(30)	0.6116(21)	0.6157(22)	0.6154(22)
	U_{iso}*100	0.51(14)	1	1.69(29)	0.05(20)	1
	Occ	0.6	0.6	0.6	0.6	0.6
Ga2 *16e*	*x*	0.0582(6)	0.0557(18)	0.0491(10)	0.0495(11)	0.0481(11)
	y	0.1344(5)	0.1411(14)	0.1285(10)	0.1360(11)	0.1370(12)
	z	0.6240(13)	0.6293(30)	0.6116(21)	0.6157(22)	0.6154(22)
	U_{iso}*100	0.51(14)	1	1.69(29)	0.05(20)	1
	occ	0.4	0.4	0.4	0.4	0.4
O1 *8d*	*x*	0.3865(8)	0.3879(11)	0.4122(15)	0.3933(16)	0.3910(18)
	y	0.25	0.25	0.25	0.25	0.25
	z	0.125	0.125	0.125	0.125	0.125
	U_{iso}*100	1.84(10)	4.7(5)	1.83(20)	1.22(18)	1.21(20)

O2 16e	*x*	0.1357(5)	0.1371(11)	0.1287(11)	0.1423(11)	0.1395(12)
	y	0.0601(6)	0.0587(15)	0.0661(10)	0.0556(14)	0.0525(14)
	z	0.4786(9)	0.4829(26)	0.4682(18)	0.5273(22)	0.5261(23)
	U_{iso}*100	1.84(10)	4.7(5)	1.83(20)	1.22(18)	1.21(20)
O3 *16e*	*x*	0.0506(5)	0.0519(11)	0.0483(9)	0.0091(9)	0.0082(10)
	y	0.0931(6)	0.0918(15)	0.0904(10)	0.1072(14)	0.1076(15)
	z	0.8640(10)	0.8683(26)	0.8668(20)	0.8507(23)	0.8516(23)
	U_{iso}*100	1.84(10)	4.7(5)	1.83(20)	1.22(18)	1.21(20)
Na *8d*	*x*	0.6899(17)	0.6927(33)	0.717(4)	0.701(4)	0.707(4)
	y	0.25	0.25	0.25	0.25	0.25
	z	0.125	0.125	0.125	0.125	0.125
	U_{iso}*100	4.7(7)	0.1(10)	7.1(16)	4.3(15)	4.5(16)
OW1 *8d*	*x*	0.1326(9)	0.1212(27)	0.0929(28)	0.1237(24)	0.1246(22)
	y	0.25	0.25	0.25	0.25	0.25
	z	0.125	0.125	0.125	0.125	0.125
	U_{iso}*100	2.76(27)	2.5(7)	2.5	4.37(56)	2.97(45)
D11 *16e*	*x*	0.0885(18)	0.0865(23)	0.1339(23)	0.0898(15)	0.0894(16)
	y	0.2010(13)	0.199(6)	0.1959(13)	0.2014(12)	0.2022(11)
	z	0.0527(33)	0.055(19)	0.071(5)	0.0496(26)	0.0456(24)
	U_{iso}*100	7.5(18)	2.0(13)	2.5	6.7(5)	6.0(5)
	occ	0.570(23)	0.71(5)	1	1	1
H11 *16e*	*x*	0.0885(18)	0.0865(23)			
	y	0.2010(13)	0.199(6)			
	z	0.0527(33)	0.055(19)			
	U_{iso}*100	7.5(18)	2.0(13)			
	occ	0.430(23)	0.29(5)			
OW2 *8d*	*x*	0.8454(70)	0.8455(44)	0.8840(24)	0.8861(21)	0.8876(20)
	y	0.25	0.25	0.25	0.25	0.25
	z	0.125	0.125	0.125	0.125	0.125
	U_{iso}*100	2.76(27)	2.5(7)	2.5	4.37(56)	2.97(45)
	Occ	0.118(19)	0.271(36)	1	1	1
D22 *16e*	*x*	0.2009(67)	0.2020(29)	0.1939(15)	0.2499(18)	0.2436(18)
	y	0.1111(102)	0.111(4)	0.0733(28)	0.0799(15)	0.0794(14)
	z	-0.0654(152)	-0.049(7)	-0.083(7)	-0.0086(21)	-0.0069(19)
	U_{iso}*100	12.1(57)	2.0(13)	2.5	6.7(5)	6.0(5)
	Occ	0.118(19)	0.27(4)	1	1	1

*Weights in parenthesis

Table 10: Bond distance and angles of tetragonal Ga-NAT at ambient and high pressures.*

	Pressure (GPa)				
	0	0.14	0.88	1.88	2.30
T-atom Tetrahedra					
Bond Length (Å)					
T1_O3	1.66838(7)	1.657(16)	1.642(16)	1.730(18)	1.726(19)
T2_O1	1.69254(8)	1.638(19)	1.732(16)	1.685(18)	1.690(19)
T2_O2	1.71895(7)	1.826(25)	1.663(19)	1.723(20)	1.741(20)
T2_O2	1.70591(7)	1.700(29)	1.649(18)	1.682(24)	1.621(22)
T2_O3	1.69385(12)	1.718(25)	1.753(19)	1.689(19)	1.693(20)
T-O-T Inter-Chain Bond Angle					
T2_O1_T2	128.872(0)	125.2(16)	144.7(15)	126.8(15)	123.4(15)
Na Environment					
Bond Length/distances (Å)					
NA_O1	2.58070(11)	2.593(16)	2.781(20)	2.595(17)	2.548(18)
NA_O2	2.38767(10)	2.447(34)	2.69(4)	2.60(4)	2.69(4)
NA_NA	3.69191(23)	3.65(4)	3.405(28)	3.55(4)	3.495(31)
NA_OW1	2.41122(11)	2.509(30)	2.727(33)	2.436(26)	2.403(23)
NA_OW2	2.06385(9)	2.04(8)	2.27(6)	2.44(6)	2.38(6)
Selected Bond Angles (°)					
OW1_NA_OW1	141.612(2)	144.5(19)	161.0(21)	149.3(22)	152.786(3)
OW1_NA_OW2	70.806(1)	72.2(9)	80.5(11)	74.7(11)	76.393(1)
Water Bonding					
Bond Length (Å)					
OW1_D11	0.99453(4)	0.950(19)	0.986(17)	0.928(18)	0.941(16)
OW2_D22	0.97706(4)	1.00(4)	0.995(23)	0.892(18)	0.898(16)
Bond Angle (°)					
D11_OW1_D11	108.486(2)	122.(4)	111.(4)	122.(4)	121.(4)
D22_OW2_D22	104.092(1)	109.(7)	109.(4)	120.(4)	122.(4)
Hydrogen Bonding & Related Distances†					
D22…..O3	2.04446(9)		2.016(29)		
O3…..D11	1.96567(8)	1.944(32)		2.102(19)	2.083(19)
O2…..D22				2.116(23)	2.196(25)

*Weights in parenthesis

† Grey shading: D…..O distances which have exceeded the hydrogen bonding limit (2.3 Å). Distances over 3.0 Å are not reported.

4.1.2.3 Volume Expansion and Superhydration in Tetragonal Ga-NAT.

With the application of hydrostatic pressure we see a number of structural and compositional changes to Ga-NAT, all of which are reversible upon pressure release. These effects include unit cell volume expansion and super-hydration, which are facilitated by changes in the chain rotation angle (Ψ) and T-O-T angles. These changes also affect the occurrence and strength of hydrogen bonding.

Upon application of pressure, tetragonal Ga-NAT exhibits an immediate expansion. This response differs from that of the orthorhombic form, which shows compression until transition to the superhydrated phase. The expansion from ambient to a maximum at 0.88 GPa is accompanied by a gradual filling of the OW2 position from 0.168(20) to a maximum occupancy of 1. The pressure dependence of unit cell volume and OW2 occupancy is shown in Figure 10. The unit cell volume expansion (3.76%) occurs via an increase of 2.65 % in the *a*- and *b*-axis parameters (Figure 9). This expansion is considerably larger than that observed for the orthorhombic form and larger than any other reported cell expansion for the superhydrated phase within the natrolite family.[5] The total volume expansion of tetragonal Ga-NAT is 1.94% larger than orthorhombic Ga-NAT and 2.76% larger than previously reported orthorhombic Ga-NAT values.[4] The mechanism by which this expansion occurs is discussed later in this chapter, where chain rotation, pore dimensions and T-O-T angles are considered.

Following the formation of the superhydrated phase, the unit cell (whilst maintaining full OW2 occupancy), progresses down a compression curve as the applied pressure is increased. The pressure and volume data obtained from this compression curve can be used to fit an equation of state to the superhydrated phase. Both the bulk modulus and an extrapolated 'V_0' can be obtained for the superhydrated phase. Results from EoS fitting are discussed in later sections within this chapter.

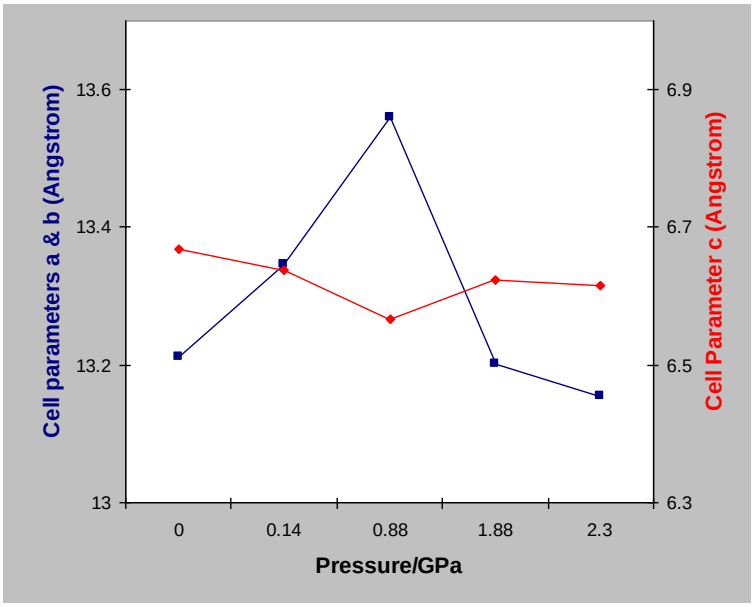

Figure 9: Pressure effect upon cell parameters for tetragonal Ga-NAT.

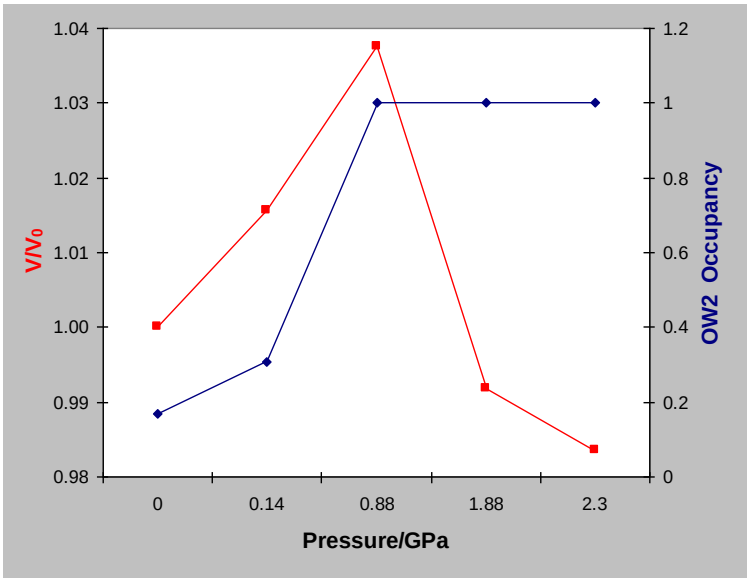

Figure 10: Pressure effect upon normalized volume (V/V_0) and OW2 occupancy for tetragonal Ga-NAT.

4.2 High Pressure Effects upon the Gallosilicate Natrolite Framework

As well as the characteristic unit cell volume expansion observed during PIH, there are a number of other measurements than can be made which reveal details of the response of the gallosilicate natrolite framework to high pressures. These measurements offer details of the mechanism by which unit cell expansion occurs. These measurements include: pore dimensions, chain rotation and T-O-T bond angle flexibility, all of which revert back to ambient pressure values upon pressure release.

4.2.1 Pore Dimensions and Chain Rotation

Pore measurements reported here represent the distances between O2 oxygen atoms in the *a*,*b*-plane for Al-NAT and orthorhombic Ga-NAT or O1 oxygen distances in the same plane for tetragonal Ga-NAT. Figure 11 shows a polyhedral representation of these measurements. Chain rotation angles are calculated as the angle of the fibrous chain from the normal (defined as the *a*- and *b*-axes). For orthorhombic Ga-NAT $\Psi_1 \neq \Psi_2$ and for tetragonal Ga-NAT $\Psi_1 = \Psi_2$ due to the tetragonal symmetry. The rotation angle Ψ is the average between the two values, Ψ_1 and Ψ_2. Results are shown in Table 11 and Figure 12.

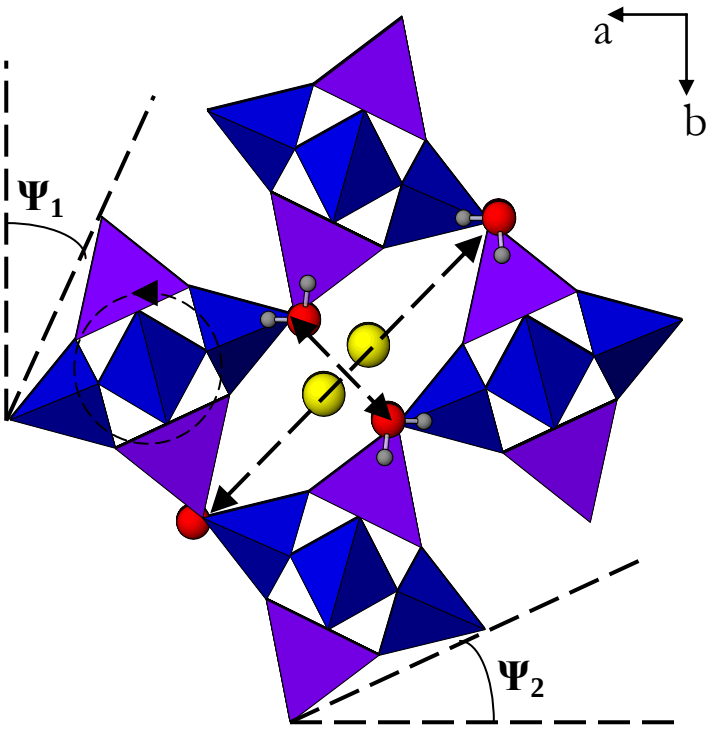

Figure 11: Polyhedral representation illustrating measurements for pore dimensions and chain rotation (Ψ).

Table 11: Pore dimensions and rotation angles of Al-NAT and Ga-NAT.

	Pressure (GPa)	Pore Length (Å)	Pore width (Å)	Ψ(°)
Aluminosilicate Natrolite[3]	0	10.007	4.882	25.000
	1	9.740	5.300	20.500
	1.5	10.020	4.940	23.500
Orthorhombic Ga-NAT	0	10.1946	4.8578	24.825
	0.22	10.2844	4.7846	25.595
	0.74	9.8572	5.2252	21.500
	1.83	10.0400	4.9732	23.615
	2.26	10.0665	4.9126	24.085
Tetragonal Ga-NAT	0	10.1654	4.9123	24.410
	0.14	10.1890	4.9788	23.930
	0.88	9.7331	5.4883	19.360
	1.88	9.9837	5.0278	23.120
	2.30	10.0083	4.9693	23.560

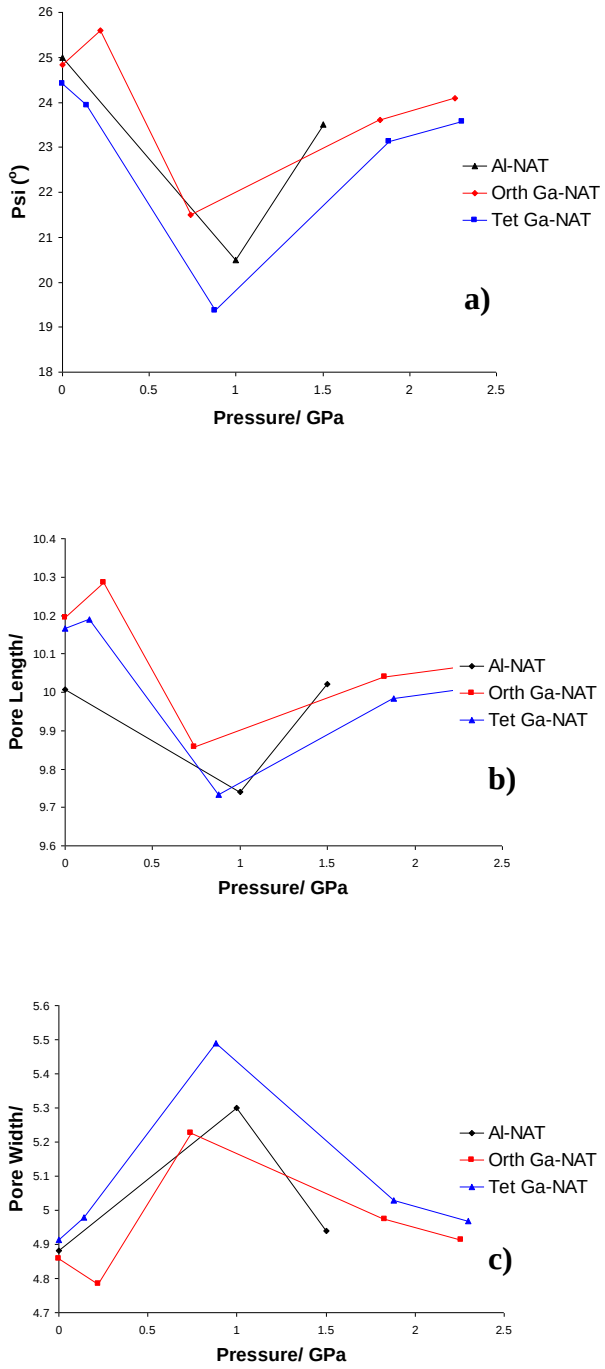

Figure 12: Pressure effects upon pore dimensions and rotation angle (Psi) of Al-NAT and Ga-NAT. a) psi, b) pore length, c) pore width.

Generally, upon cell expansion we see an increase in pore width and a decrease in pore length to give a less elliptical, more open pore shape. This shape change is facilitated by rotation of the fibrous chains, so that the angle Ψ is reduced.

When comparing the three natrolite materials (Figure 12), we see that generally, at ambient pressure and at superhydration, aluminosilicate shows the lowest pore width and highest pore length and Ψ, making the pores more elliptical, and the framework less open when compared to the two gallosilicates. This is reflected in the pressure at which superhydration is observed: 1.5 GPa for Al-NAT verses ~0.8 GPa for both Ga-NAT forms. So the more open, flexible gallosilicates show superhydration at much lower pressures. Also, the aluminosilicate pore length and Ψ increase much more rapidly, post superhydration, with a parallel decrease in pore width. This means compression of the superhydrated phase causes the pore to close down into a more elliptical shape much more rapidly than is seen in the gallosilicates. From these measurements it is clear that substitution of the larger Ga atom for Al yields a more open flexible framework which exhibits similar PIH but with much lower pressure onset values.

By making use of pore dimension measurements and chain rotation angles we can begin to differentiate between the nature of the tetragonal verses the orthorhombic gallosilicate, with respect to framework flexibility and pore elipticity. At ambient pressure tetragonal Ga-NAT appears to be the most open, with the largest pore width (4.9123 Å) and the smallest pore length (10.1654 Å) and Ψ (24.410°); with orthorhombic values at 4.8578 Å, 10.1946 Å and 24.825° respectively. Again, tetragonal Ga-NAT shows a more open, flexible framework at superhydration with the largest pore width (5.4883 Å) and the smallest pore length (9.7331 Å) and Ψ (24.410°); with orthorhombic values at 5.2252 Å, 9.8572 Å and 21.500° respectively. These trends point towards increased flexibility and openness in the tetragonal form of Ga-NAT. From this we can assume that the tetragonal form would: a) Show a greater expansion at PIH and b) Show PIH at lower pressure values; when compared to the orthorhombic analogue.

From these experiments, measurements show tetragonal Ga-NAT does exhibit a larger volume expansion due to superhydration, 3.76% (43.72 $Å^3$) verses the 1.82% (41.95 $Å^3$) seen in orthorhombic Ga-NAT. However, evidence showing whether or not the tetragonal

form shows early onset values of superhydration cannot be given with any certainty. Due to the nature of this experiment, a small number of pressure steps with large increments were necessary. Further investigation, with a larger number of pressure points at small increments around this region, should clarify the differences in PIH onset values between the two forms. Measurements illustrating a low PIH onset value for tetragonal Ga-NAT (compared with orthorhombic), are given in the high pressure experiments discussed in chapter 5.

From the evidence gained from the experiments discussed in this chapter we can only postulate that PIH pressure values should be lower for tetragonal Ga-NAT. One factor giving weight to this idea is the low pressure behaviour of the two forms. Orthorhombic Ga-NAT shows compression, whilst tetragonal Ga-NAT shows expansion from the very first pressure step.

In conclusion, the measurements discussed here have shown that Ga for Al substitution increases the flexibility and 'openness' of the framework. Also, disordered T sites (tetragonal) verses ordered T sites (orthorhombic) further increases flexibility and openness of the framework. So the general trend is:

Tetragonal Ga-NAT>Orthorhombic Ga-NAT>Al-NAT

This trend is reflected in the high pressure behaviour and superhydration points of all the natrolite forms.

4.2.2 T-O-T Angles

Other useful measurements for monitoring the changes in framework geometry under high pressure are the T-O-T bond angles; where T is the central atom within the tetrahedra (Si/Ga) and O is the framework oxygen linking those T atoms. Generally T-O-T angles within the chain will not show any systematic changes. However, T-O-T bonds which bridge the chains in the *a*,*b*-plane are particularly flexible. The flex of this angle is considered a facilitating factor in the cell expansion and contraction under high pressure, as seen across the natrolite family. For the orthorhombic gallosilicate this bond is the Si2-O2-Ga link (Figure 13). Equivalent to this is the T2-O1-T2 link in the tetragonal form (Figure 14).

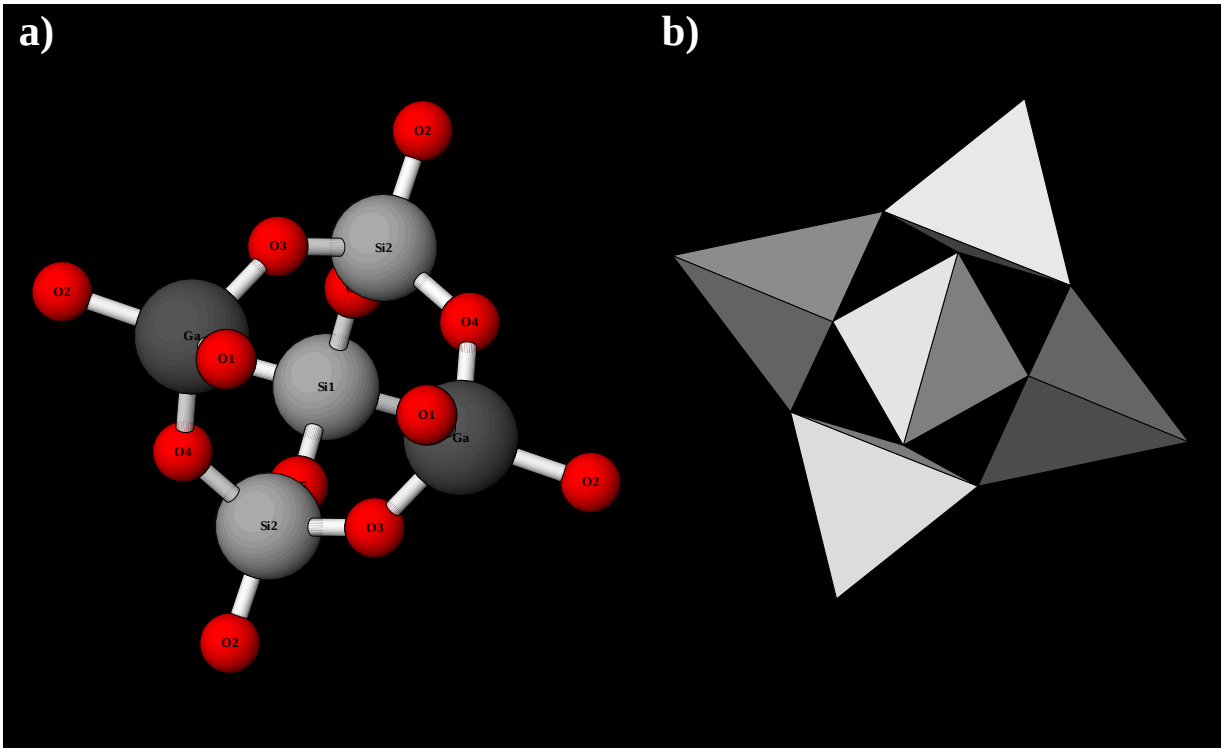

Figure 13: Bonding within the fibrous chain of orthorhombic Ga-NAT, as viewed in the *a*,*b*-plane.
(a) Tetrahedral bonding with labelled T and Oxygen atoms and (b) Solid tetrahedra.

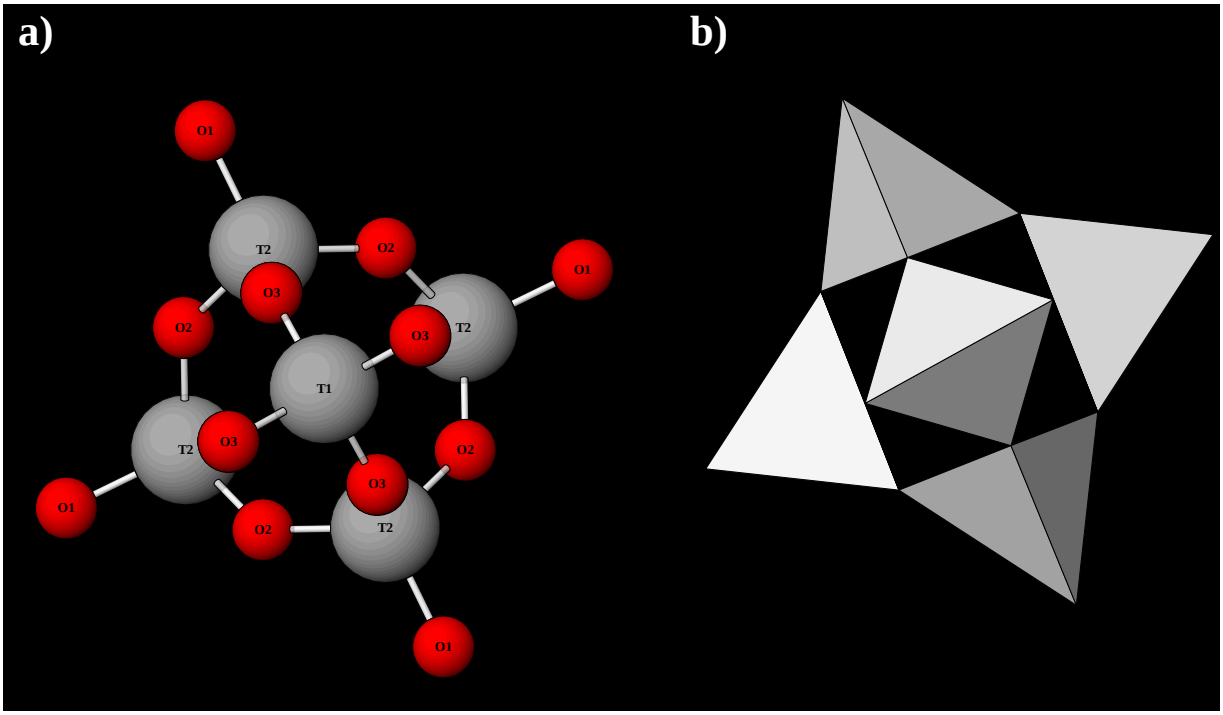

Figure 14: Bonding within the fibrous chain of tetragonal Ga-NAT, as viewed in the *a*,*b*-plane.

(a) Tetrahedral bonding with labelled T and Oxygen atoms and (b) Solid tetrahedra.

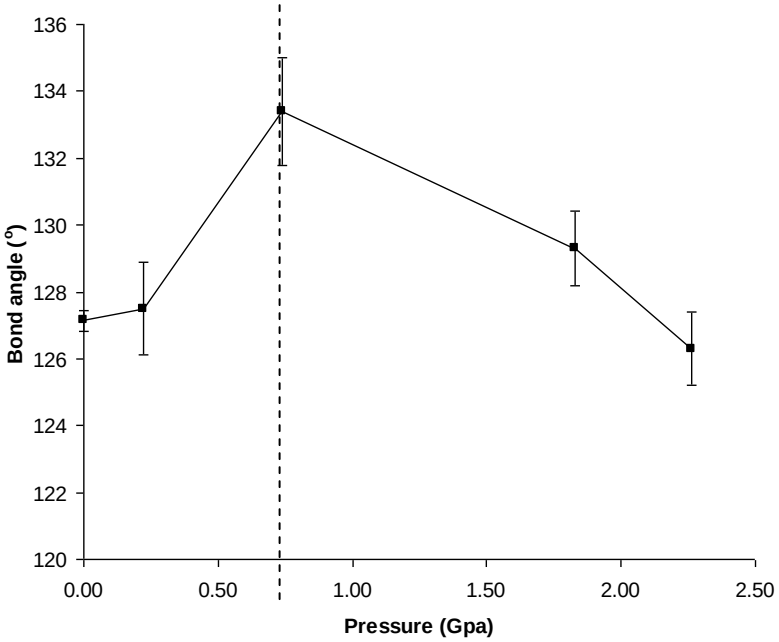

Figure 15: Effect of pressure upon the Si2-O2-Ga inter-chain bond angle for orthorhombic Ga-NAT. The dashed line indicates the pressure at which the superhydrated phase is first observed.

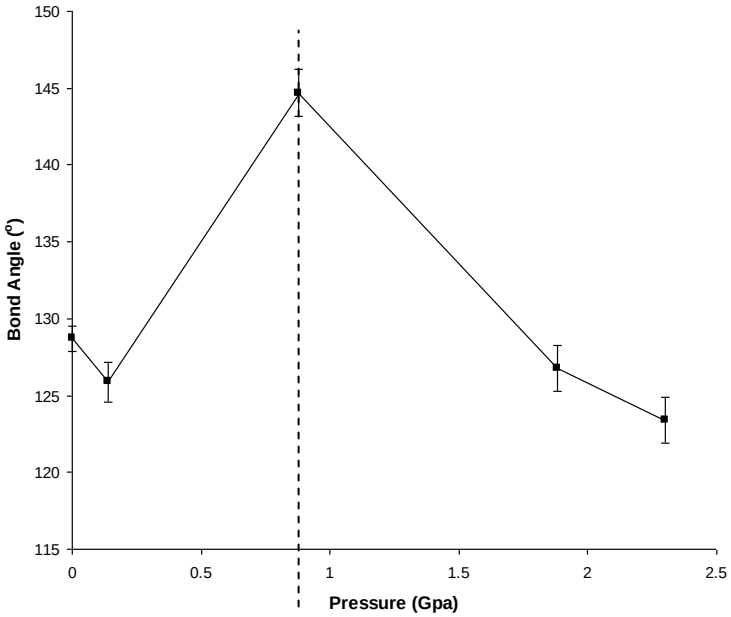

Figure 16: Effect of pressure upon the T2-O1-T2 inter-chain bond angle for tetragonal Ga-NAT. The dashed line indicates the pressure at which the superhydrated phase is first observed.

From ambient pressure up to superhydration, there is an increase in the bridging T-O-T bond angles of both the orthorhombic and the tetragonal gallosilicates. Figure 15 shows the 4.92% (6.26°) increase in the Si2-O2-Ga bond angle, which occurs from ambient to 0.74 GPa for orthorhombic Ga-NAT. Similarly, there is a 12.43% (16.00°) increase in the T2-O1-T2 bond angle from ambient to 0.88 GPa for the tetragonal form (Figure 16). The increase seen in each form reflects a chain rotation about this pivoting bond, with simultaneous opening of the pores. This mechanism facilitates the uptake of water (OW2), to reach superhydration point. Filling of the OW2 site produces a significant increase in unit cell volume, characteristic of PIH.

It is no surprise that the tetragonal form shows the greatest change in T-O-T flex, as prior measurements and discussion reveal a greater degree of flexibility in the tetragonal (verses the orthorhombic) form. This is evidenced in the previous section where pore dimensions and chain rotation were discussed. The only difference between the two gallosilicate forms is the ordering of the T atoms. In orthorhombic natrolites the T sites are ordered, whereas in the tetragonal gallosilicate there is T-atom disorder. The disorder occurring in the tetragonal form must be the reason for the difference in framework flexibility. Disordering across the T sites is likely to have an effect on the nature of the T-O-T bridging bond. We have established that it is this bridging bond which facilities the mechanism of cell volume expansion and hence superhydration. Therefore T atom disorder induces and increase in framework flexibility, which accounts for the greater volume expansion and earlier expansion onset seen in the tetragonal form.

4.2.3 Bonding Changes in Orthorhombic Ga-NAT during High Pressure Studies

Structural changes within the zeotype framework help elucidate details of the mechanism of PIH, as discussed earlier in this chapter. Equally important is understanding what is happening inside the apertures during these framework deformations. The coordination of the atoms within the pores could explain the reversibility of the PIH phenomenon. Structural representations at each pressure increment, including ambient, are shown in Figure 17 to Figure 21. Selected bond distances and angles for each can be found in Table 5.

At ambient pressure each pore contains two sodium atoms, two water molecules at full occupancy (OW1) and two water molecules at an occupancy of 0.048(4). Each sodium cation is coordinated to the framework oxygens, O3 and O4. The two sodium cations are bridged by O2 and OW1. Bridging alternates in a zig-zag formation. Although OW2 is present at ambient pressure, at a distance of 3.31(8) Å it is not bound to the sodium cation. This ambient pressure model of orthorhombic Ga-NAT is very similar to that reported for the aluminosilicate analogue Al-NAT. Artioli[2] reports similar O2 and OW1 bridging between sodium cations, with Na, oxygen coordination to O3 and O4. Artioli also reports a strong OW1-D11…O1 bond, a weak OW1-D12…O5. The main difference between the aluminosilicate and the gallosilicate natrolites (apart from the obvious Al/Ga substitution) is and the presence of OW2 water and consequently an extra OW2-D20…O5 bond. A small amount of OW2 water is present in the orthorhombic gallosilicate but none in the aluminosilicate. The presence of OW2 in the gallosilicate form is due to the increased flexibility and more open framework when compared to the aluminosilicate analogue (as discussed in earlier sections within this chapter).

In a previous report it was postulated that the presence of OW2 into a natrolite framework might produce helical water nanotubes within the pore via direct OW1-OW2-OW1-OW2 hydrogen bonding.[5]A subsequent high pressure neutron study of Al-NAT[3] as well as the high pressure works upon Ga-NAT discussed in this chapter, both show no direct

intrapore hydrogen bonding linking OW1 and OW2. In fact hydrogen bonding occurs across the pore channels (inter-pore bonding). Colligan et al.[3] report that, upon OW2 site occupancy, aluminosilicate natrolite has no direct hydrogen bonding between OW1 and OW2. They report an indirect link via O1 bridge. The study described here shows that Ga-NAT does have the same OW1- H…O1…H-OW2 link as the aluminosilicate form. Ga-NAT also has direct hydrogen bonding (H11…OW2…H12) between the two water molecules, as shown in Figure 17. This link is across the pores and not within the pores, contrary to the predicted intrapore hydrogen bonded nanotubes reported in earlier work.[5] The presence of direct cross-pore hydrogen bonding must be a result of the altered framework by Ga/Al substitution, as it is not present in the reported aluminosilicate analogue (at ambient pressure).

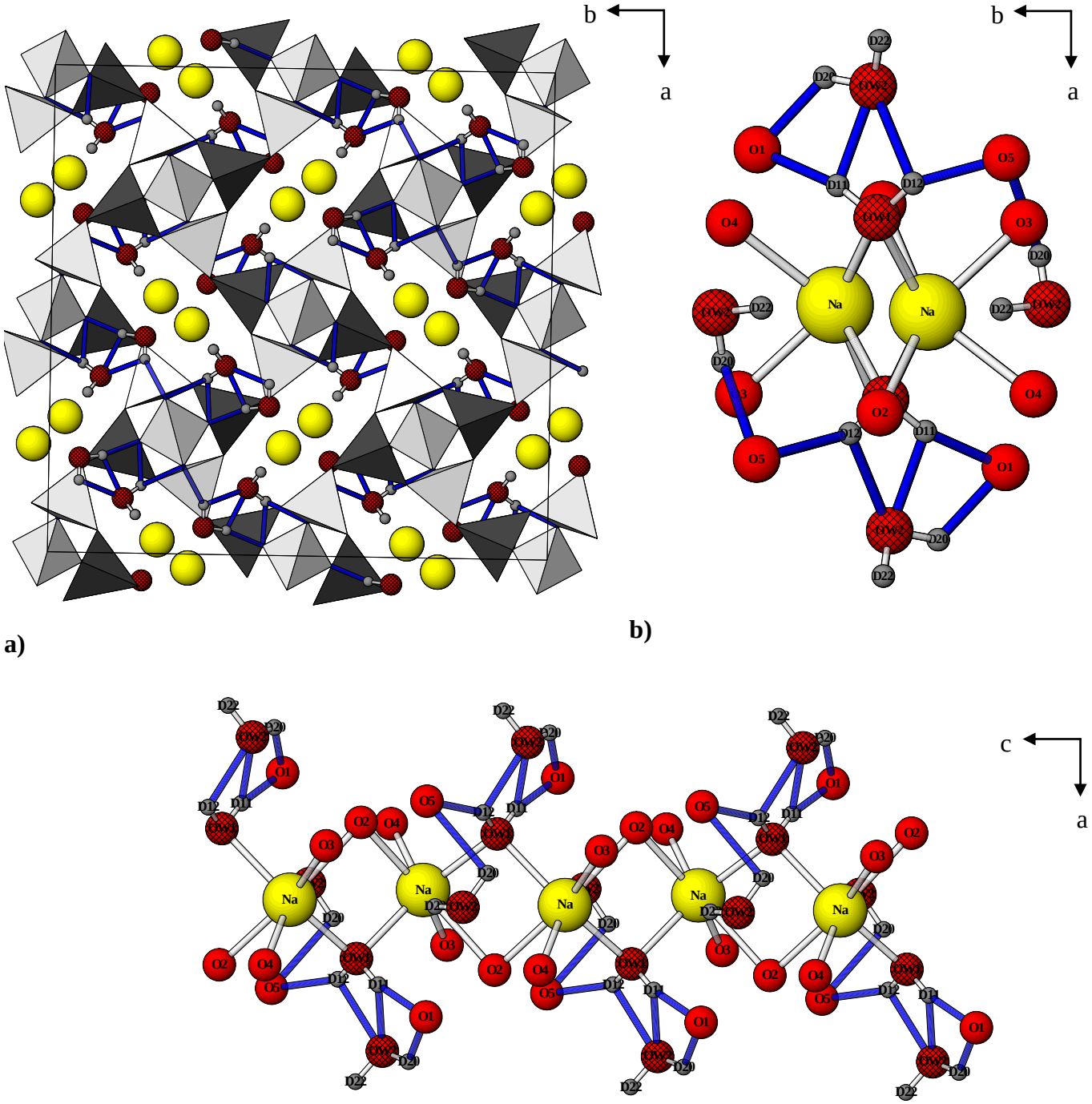

Figure 17: Structural representation of orthorhombic Ga-NAT at ambient pressure. Silicon tetrahedra (white), gallium tetrahedra (Grey), Na^+ (yellow), framework and water oxygen (red and hatched red), deuterium (grey) and hydrogen bonds (blue). a) Unit cell, b) pore species with inter-pore hydrogen bonding, c) Na coordination.

Upon the application of pressure, the OW2 oxygen remains relatively static but there is a dramatic shift in the orientation of the OW2 deuterium atoms. So, at each pressure step reorientation of D20 and D22 alters the hydrogen bonding network. Post PIH, the orientation of the OW2 deuteriums becomes fixed and remain static as the pressure increases. Structural representations of the bonding at 0.22, 0.74, 1.83 and 2.26 GPa, inclusive, are shown in Figure 18 to Figure 21.

Other than at ambient pressure, the OW1-D12…OW2 hydrogen bond exceeds the 2.2 Å limit so that, throughout the high pressure sequence this bond is not present. Upon pressure application (0.22 GPa), the orientation of OW2 deuteriums shift so that a new hydrogen bond is formed (OW2-D22…OW1), but the OW2-D20…O5 remains. Increasing the pressure up to 0.74 GPa induces PIH and cell volume expansion. In this model (Figure 19), there is another reorientation of the OW2 deuteriums D20 and D22 so that the OW2-D20…O5 and the OW2-D22…OW1 bonds are broken and a new OW2-D20…O4 bonds form.

Increasing the pressure further shows another D20, D22 reorientation. The position taken at this pressure step (1.83 GPa), becomes fixed so that it remains at the subsequent and final pressure increment (2.26 GPa). Repositioning of D22 and D20 at 1.83 GPa breaks all previous hydrogen bonding except the D20…O1…D11 (which remains over all pressures), and forms a new D22…O3 bond. By far, the most significant bonding change at 1.83 GPa is the introduction of a Na-OW2 bond. Na-O bonds are very strong so this new coordination stabilises the superhydrated framework under higher pressures. The newly formed bond creates a new, hydrogen bonded bridge between Na atoms (Na-OW2-D22…O3-Na), increasing the stabilisation of this model. See Figure 20 for a structural representation. The bonding seen here at 1.83 GPa is very similar to that described by Colligan et al.[3] for superhydrated Al-NAT. In their description there is no direct hydrogen bonding between water molecules but a hydrogen bonded link via O1, as observed here.

Increasing the pressure further to 2.26 GPa has very little effect upon bonding, presumably the higher pressure value acts to fix the positions of the inner-pore species.

The differences between Na-OW1 and Na-OW2 bonding can be used to explain both the stabilisation of the superhydrated phase and why superhydration is a reversible process. At superhydration OW2 sites are at full occupancy and are bound by reasonably complex hydrogen bonding networks. These hydrogen bonds contribute to the stabilisation of the superhydrated phase as does the subsequent formation of a single Na-OW2 bond. The sum of this bonding energy is not enough to permanently stabilise the strained high pressure, expanded state. So, upon pressure release the OW2 molecule is ejected from the pore. Conversely, the OW1 molecule remains over all pressures. The presence of OW1 must be more energetically favourable due to the two bridging Na-O bonds formed. The sum of these two strong bonds exceed any of the bonding energy contribution from OW2 (1xNa-O plus hydrogen bonding) and therefore remains unejected, inside the pore.

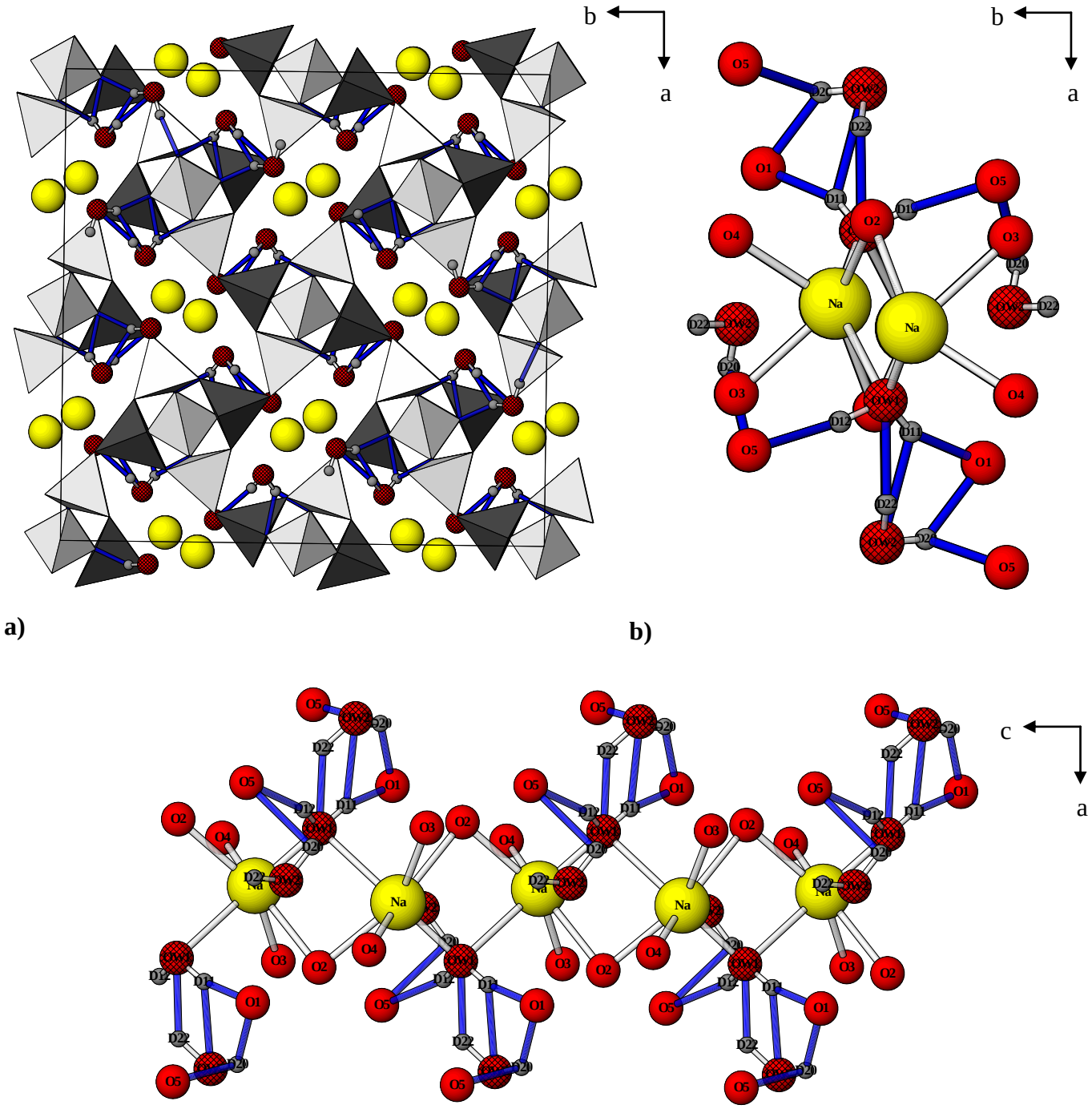

Figure 18: Structural representation of orthorhombic Ga-NAT at 0.22 GPa. Silicon tetrahedra (white), gallium tetrahedra (Grey), Na^+ (yellow), framework and water oxygen (red and hatched red), deuterium (grey) and hydrogen bonds (blue). a) Unit cell, b) pore species with inter-pore hydrogen bonding, c) Na coordination.

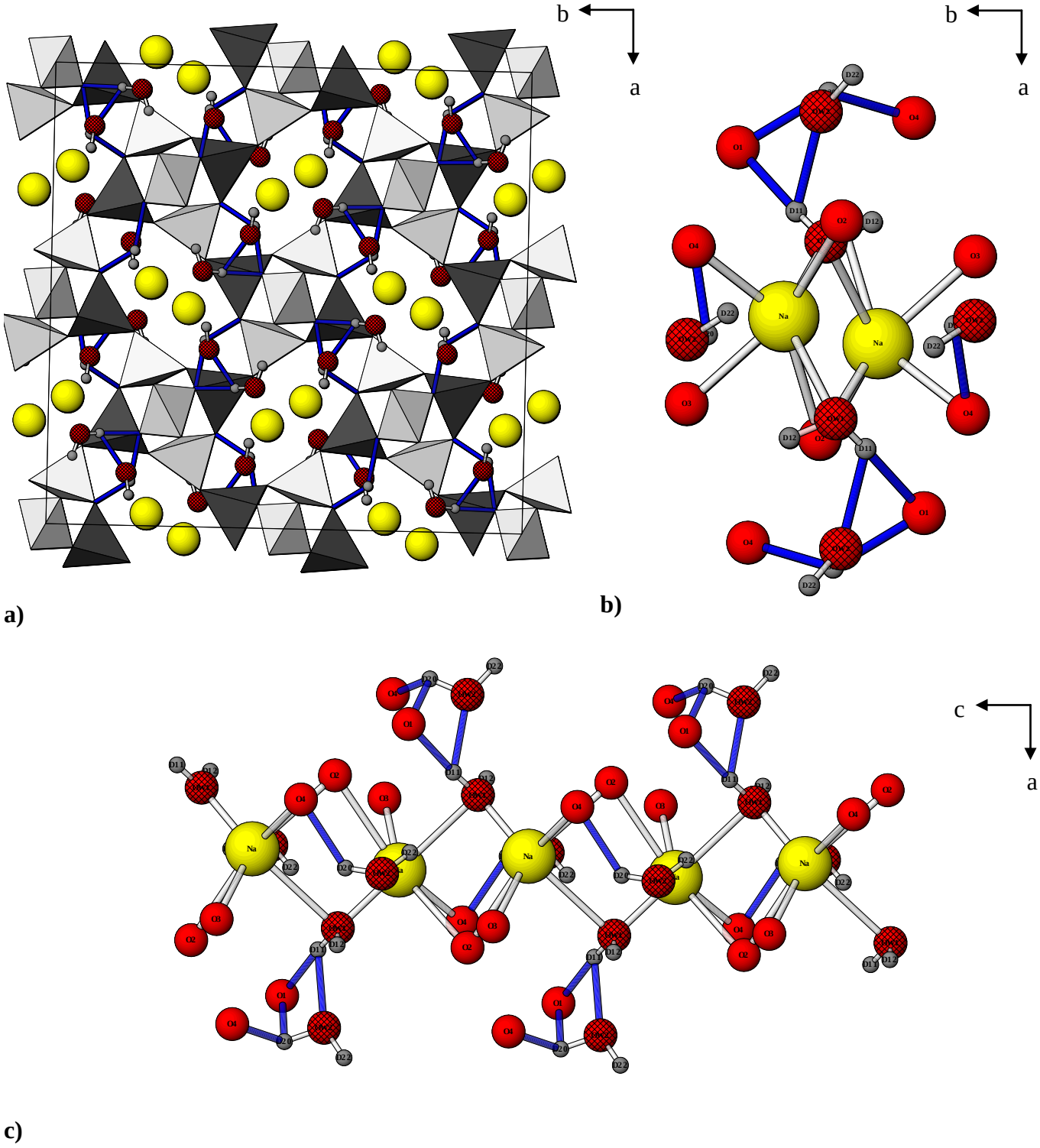

Figure 19: Structural representation of orthorhombic Ga-NAT at 0.74 GPa. Silicon tetrahedra (white), gallium tetrahedra (Grey), Na^+ (yellow), framework and water oxygen (red and hatched red), deuterium (grey) and hydrogen bonds (blue). a) Unit cell, b) pore species with inter-pore hydrogen bonding, c) Na coordination.

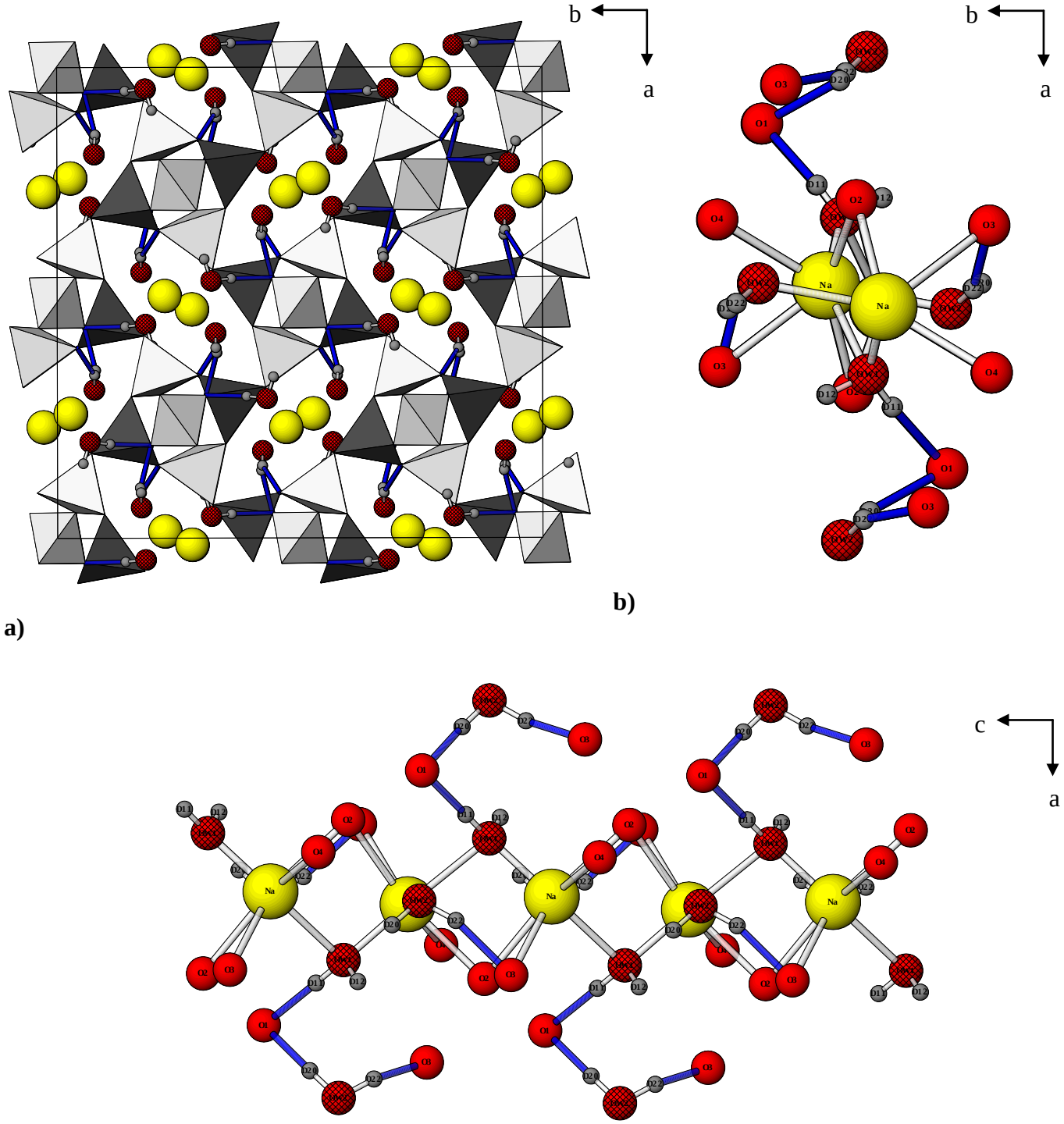

Figure 20: Structural representation of orthorhombic Ga-NAT at 1.83 GPa. Silicon tetrahedra (white), gallium tetrahedra (Grey), Na^+ (yellow), framework and water oxygen (red and hatched red), deuterium (grey) and hydrogen bonds (blue). a) Unit cell, b) pore species with inter-pore hydrogen bonding, c) Na coordination.

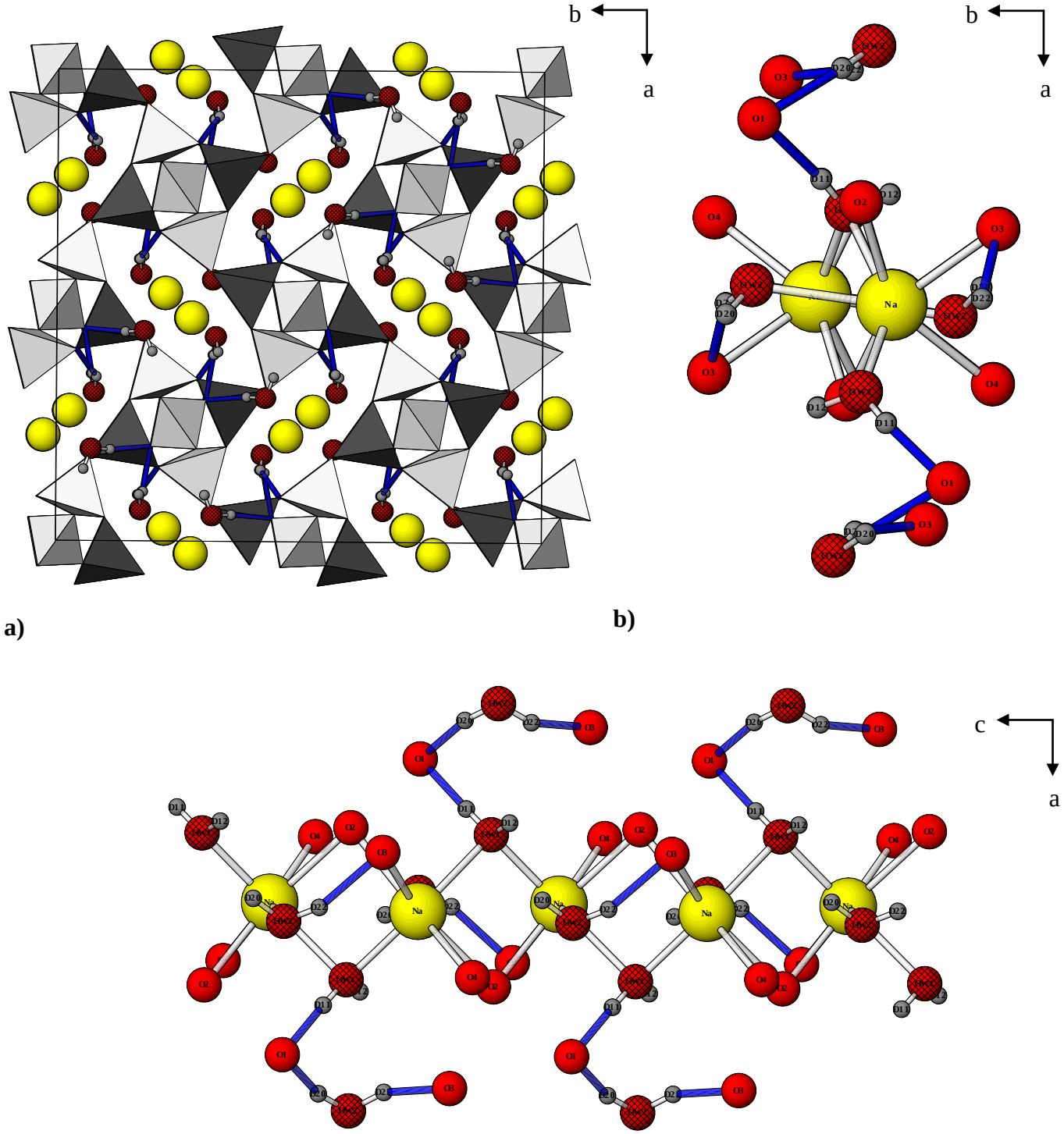

Figure 21: Structural representation of orthorhombic Ga-NAT at 2.26 GPa. Silicon tetrahedra (white), gallium tetrahedra (Grey), Na^+ (yellow), framework and water oxygen (red and hatched red), deuterium (grey) and hydrogen bonds (blue). a) Unit cell, b) pore species with inter-pore hydrogen bonding, c) Na coordination.

4.2.4 Bonding Changes in Tetragonal Ga-NAT During High Pressure Studies

Structural representations at each pressure increment, including ambient, are shown in Figure 22 to Figure 26. Selected bond distances and angles for each can be found in Table 10.

At ambient pressure each pore contains two sodium atoms, two water molecules at full occupancy (OW1=1) and two water molecules at an occupancy of (0.168(20)). Each sodium cation is coordinated to two framework oxygens, both O2 and to water molecule OW2, with bridging between the two sodium cations by coordination to O1 and OW1. Bridging alternates in a zig-zag formation.

There are some distinct differences between tetragonal and orthorhombic gallosilicate natrolite at ambient pressure. Both forms have a small proportion of OW2 present and significant hydrogen bonding networks. At ambient pressure, the two water molecules OW1 and OW2 are linked via a bridging hydrogen bond through framework oxygen O3. In the orthorhombic form there is an equivalent bridge via O1. However, in the orthorhombic form the two water molecules are also directly linked via a (H11…OW2…H12) hydrogen bond; which is not observed in the tetragonal form.

Another key difference is the presence of Na-OW2 bond at ambient pressure. The orthorhombic model contains OW2, which forms hydrogen bonds upon pressure application, but only forms a Na-OW2 bond post superhydration. The presence of this strong bond at ambient pressure is seen only in the tetragonal form. The presence of this bond forces the Na cation to become 7-coordinate rather than 6-coordinate. The tetragonal form also shows an increased ambient pressure water content compared to the orthorhombic model (0.118(19) in tetragonal verses 0.048(4) in orthorhombic) and increased pore dimensions (4.9123 Å for tetragonal and 4.8578 Å for orthorhombic). These differences can be explained by considering the T atom ordering.

The fundamental difference between the two gallosilicates is the ordering of the T atom sites. In the orthorhombic form the sites are completely ordered and in the tetragonal they are disordered. This disordering of the T sites affects the nature of the T-O-T chain-bridging bond causing it to become more flexible. It is this bond which facilitates the chain rotation and pore opening, so the flexibility of this bond dictates the high pressure chemistry of the whole system. If the tetragonal model has greater flex in this bond, the pores could become more open, which in-turn would allow for increased water content even at ambient pressure. This open, more hydrated state is stabilised due to the presence of a strong Na-OW2 bond.

It is important to note that this strong Na-OW2 bond clearly provides stabilisation of the ambient pressure model, but is not enough to stabilise full OW2 occupancy, as superhydration is reversible upon pressure release.

From the ambient pressure model alone, we can surmise that the tetragonal form is more open and flexible than the orthorhombic form and that this is due to the presence of extra OW2 water, stabilised by a Na-OW2 bond.

The Na-OW2 bond can also be used to explain the differences in hydrogen bonding between the two forms. Due to the presence of the Na-OW2 bond, the oxygen of OW2 is much further away from the deuteriums of OW1 (across, not within the pores). For this reason, the equivalent D11...OW2…D11 direct hydrogen bonding that occurs across the channels in the orthorhombic model is not observed in the tetragonal form (compare Figure 17 with Figure 22).

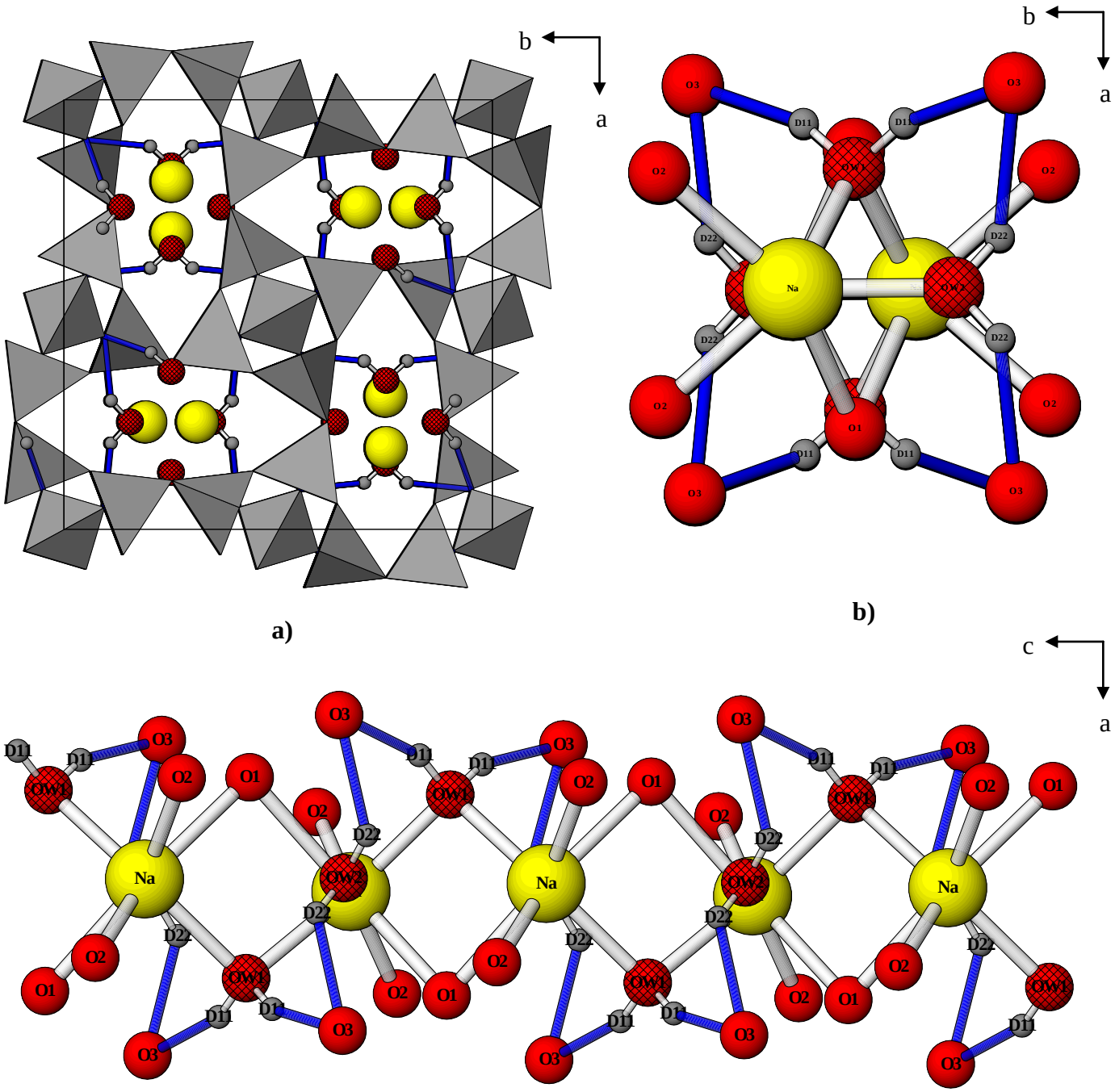

Figure 22: Structural representation of tetragonal Ga-NAT at ambient pressure. Silicon tetrahedra (white), gallium tetrahedra (Grey), Na^+ (yellow), framework and water oxygen (red and hatched red), deuterium (grey) and hydrogen bonds (blue). a) Unit cell, b) pore species with inter-pore hydrogen bonding, c) Na coordination.

Upon initial pressure application, the bonding within the pore remains relatively static, as observed for the orthorhombic form. The hydrogen bonding present at ambient pressure is still evident at 0.14 GPa. However, there is one rather significant change at this pressure. The unit cell has expanded at a very low pressure, rather than contracted. So superhydration begins very early, at lower pressures when compared to the orthorhombic form; another consequence of the increased framework flexibility. The increase in pore size that accompanied volume expansion also comes with an increase in OW2 water content (from 0.118(19) to 0.2020(29)).

Increasing the pressure further, up to 0.88 GPa, causes transition to the superhydrated state. This dramatically affects the bonding within the pores. The pores open significantly. At 0.88 GPa, the hydrogen bonded bridge between the two water molecules (OW2-D22…O3…D11-OW1) is no longer viable as superhydration has caused the deuteriums of OW1 to change orientation by almost 180° (Figure 24).

Increasing the pressure up to 1.88 GPa induces another bonding shift within the pore. The OW1 deuteriums revert back to their previous orientation, so that hydrogen bonding (2x OW1-D11…O3) is restored. The hydrogen bonding associated with the OW2 molecule changes due to slight reorientation of the deuteriums; from bonding to framework oxygen O3, to framework oxygen O2. The bonding arrangement shows very little change as the pressure is increased from 1.88 GPa to 2.30 GPa, presumably the high pressure causes a compression which ‘locks’ the atoms and bonding in place. This is also observed when the orthorhombic form is exposed to pressures within this range.

At no pressure point is there any direct hydrogen bonding between water molecules (as seen in most orthorhombic pressure points). The only evidence of an indirect link is at low pressure (prior to superhydration); where an OW2-D122…O3…D11-OW1 bridge is observed. Conversely, the equivalent framework oxygen bridged hydrogen bond (OW1-D11…O1…D20-OW2), is present over all pressures for the orthorhombic form.

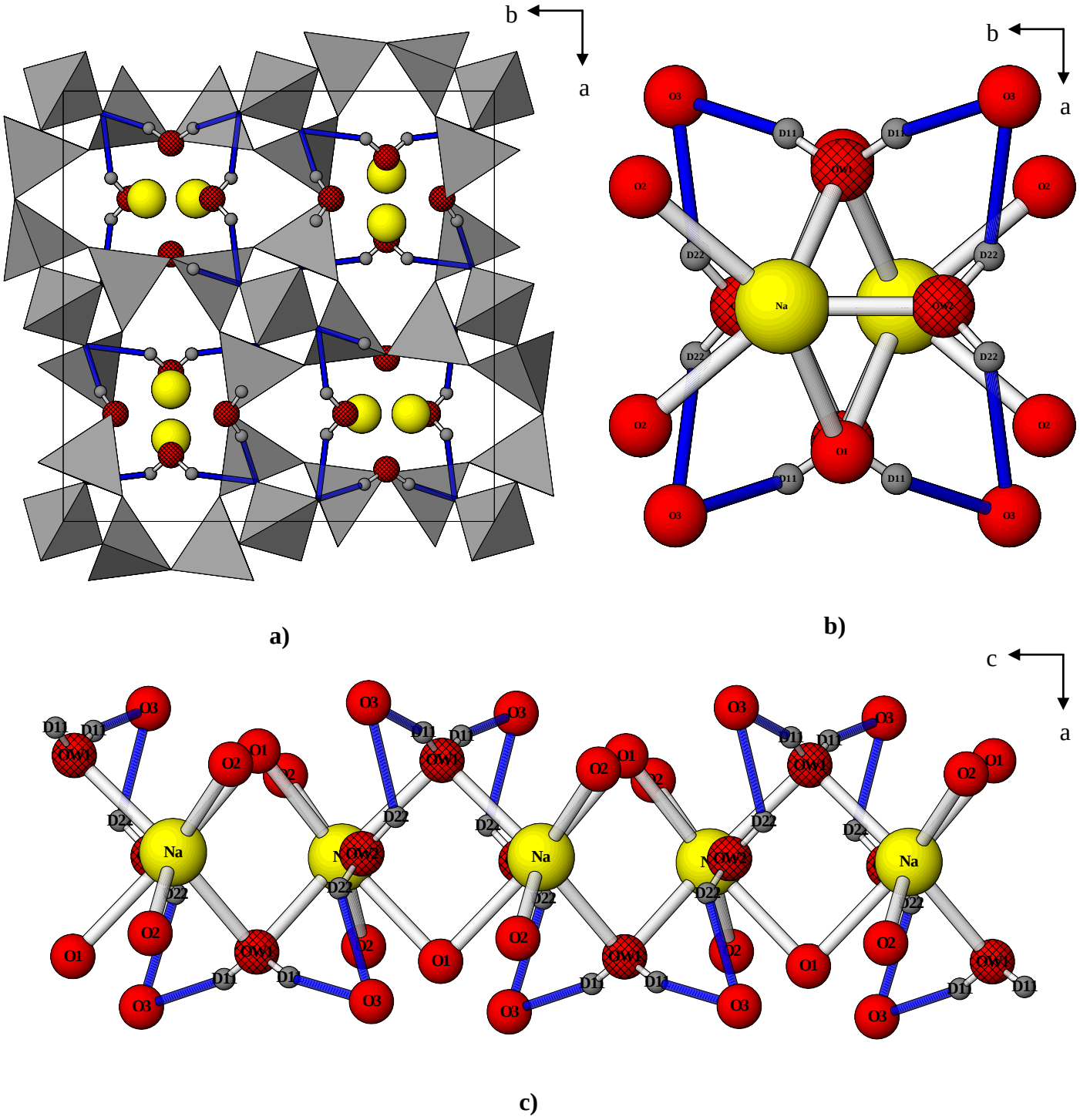

Figure 23: Structural representation of tetragonal Ga-NAT at 0.14 GPa. Silicon tetrahedra (white), gallium tetrahedra (Grey), Na^+ (yellow), framework and water oxygen (red and hatched red), deuterium (grey) and hydrogen bonds (blue). a) Unit cell, b) pore species with inter-pore hydrogen bonding, c) Na coordination.

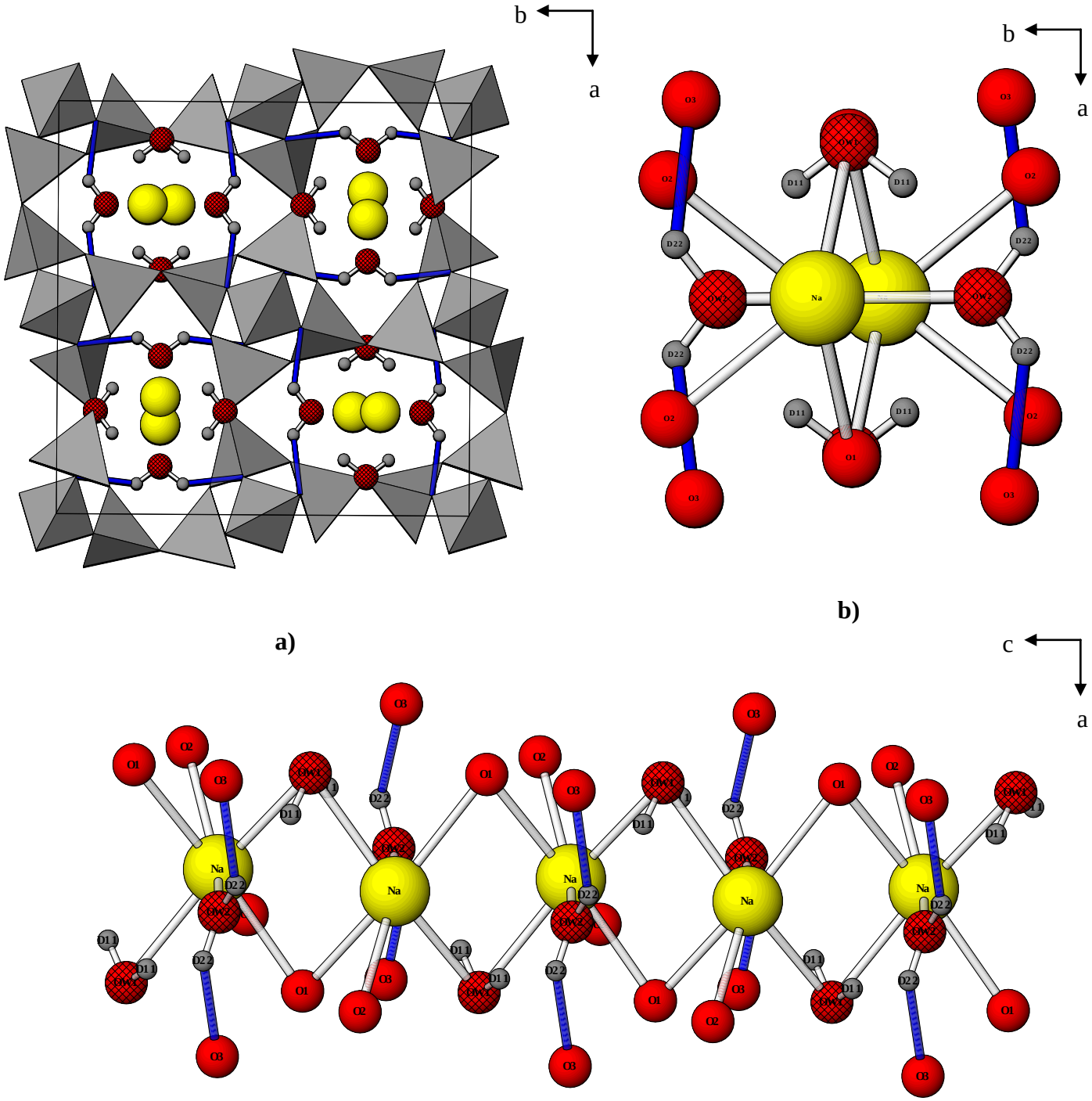

Figure 24: Structural representation of tetragonal Ga-NAT at 0.88 GPa. Silicon tetrahedra (white), gallium tetrahedra (Grey), Na^+ (yellow), framework and water oxygen (red and hatched red), deuterium (grey) and hydrogen bonds (blue). a) Unit cell, b) pore species with inter-pore hydrogen bonding, c) Na coordination.

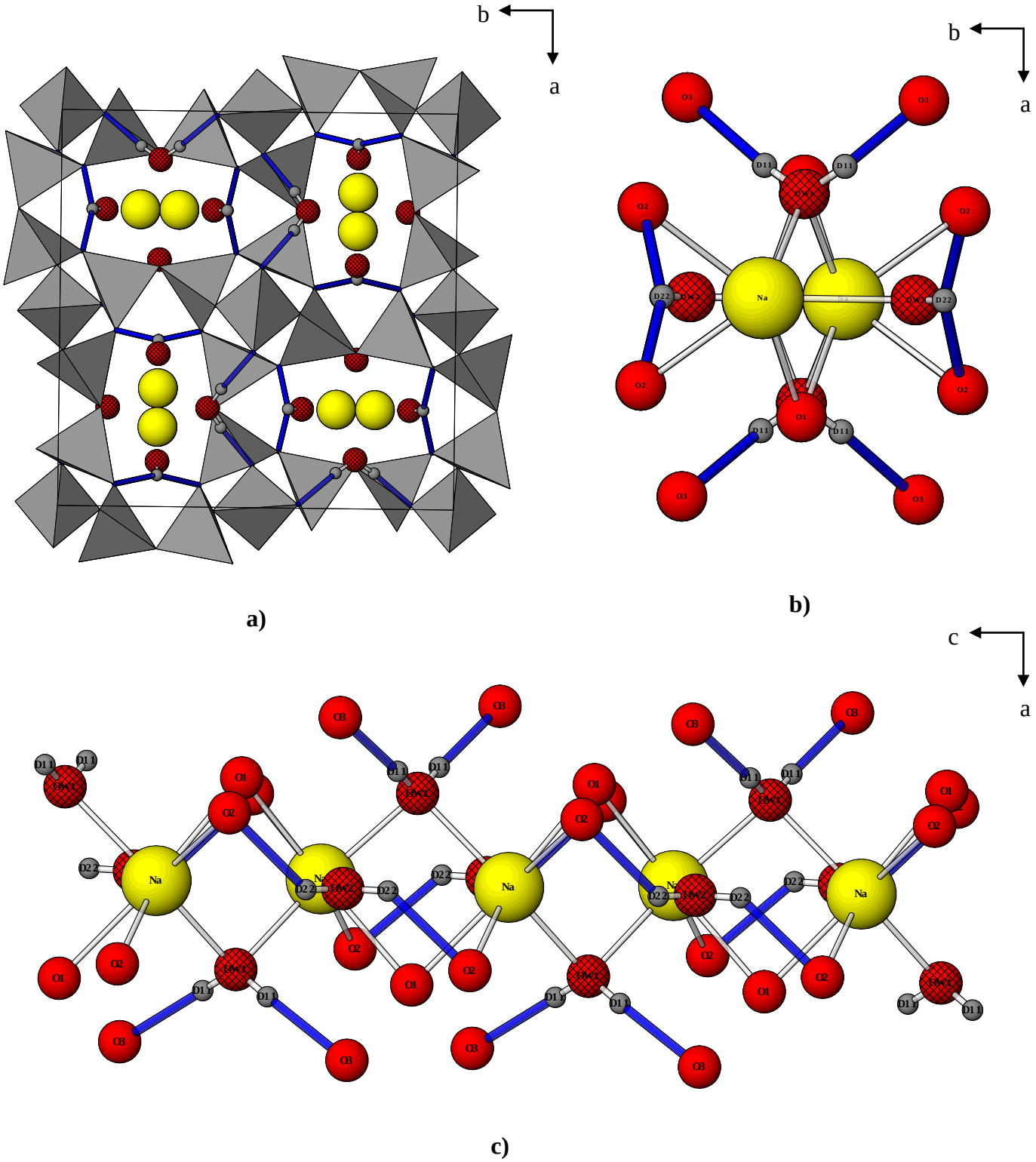

Figure 25: Structural representation of tetragonal Ga-NAT at 1.88 GPa. Silicon tetrahedra (white), gallium tetrahedra (Grey), Na^+ (yellow), framework and water oxygen (red and hatched red), deuterium (grey) and hydrogen bonds (blue). a) Unit cell, b) pore species with inter-pore hydrogen bonding, c) Na coordination.

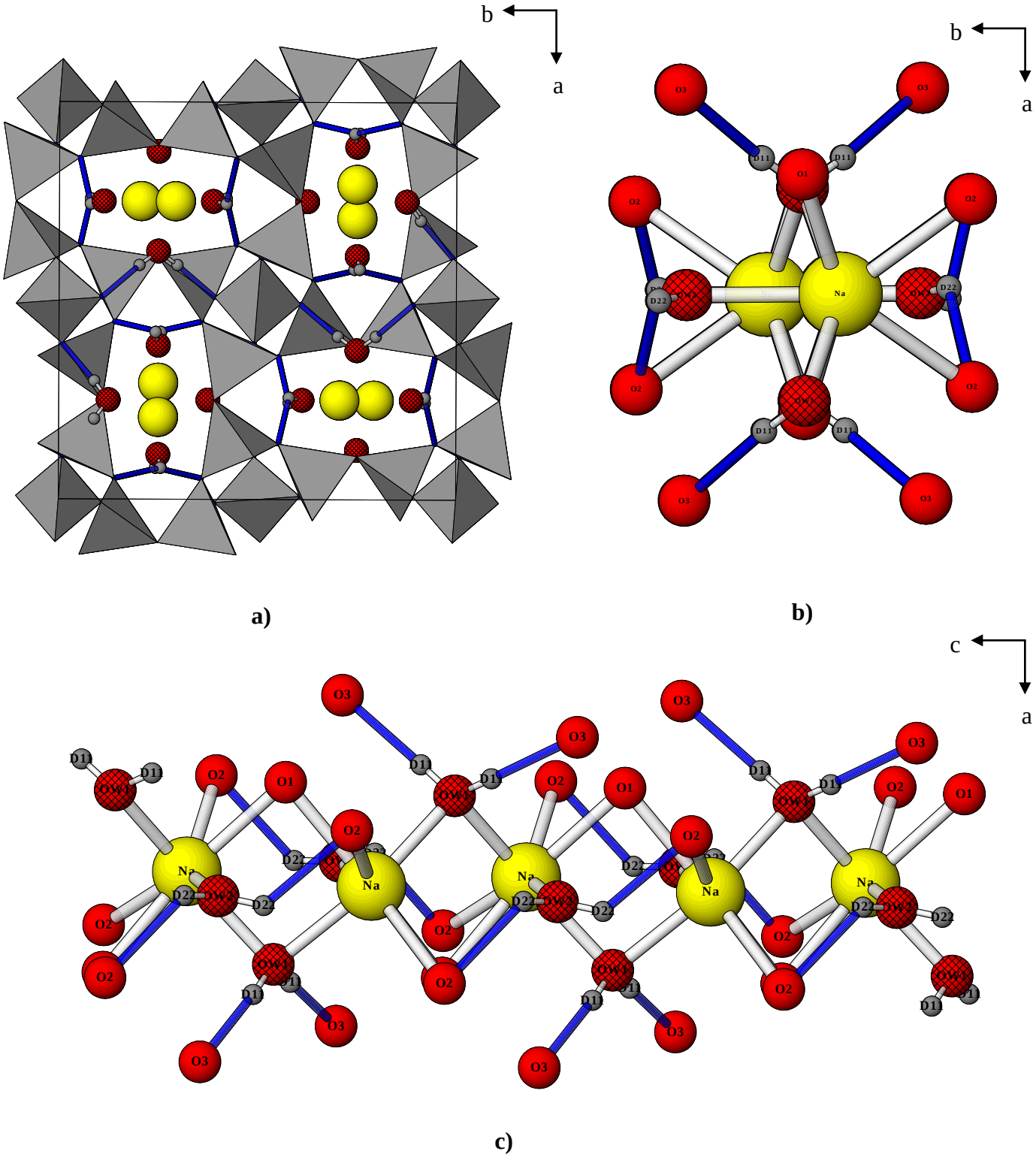

Figure 26: Structural representation of tetragonal Ga-NAT at 2.30 GPa. Silicon tetrahedra (white), gallium tetrahedra (Grey), Na^+ (yellow), framework and water oxygen (red and hatched red), deuterium (grey) and hydrogen bonds (blue). a) Unit cell, b) pore species with inter-pore hydrogen bonding, c) Na coordination.

4.3 Bond Valence

One of the most significant differences between the intrapore bonding seen in the orthorhombic compared to the tetragonal gallosilicate is the Na-OW2 bond. In the orthorhombic form, OW2 water is present within the pores but is not coordinated to sodium until after superhydration has been established. Until this point is reached, the coordination around each sodium cation is bipyramidal; with four Na-O coordinations to framework oxygens and two to OW1 water oxygens. Addition of a Na-OW2 bond increases Na coordination from 6 to 7. See Figure 27 for a graphical representation of the sodium environment. Bond valence sums carried out as outlined by Brown *et.al.*[8] show an increase in V_i (the bond valence summation or oxidation state of the sodium cation) as coordination is increased from 6 to 7 (0.97(11) to 1.28(18) respectively). Equation 1 and Equation 2 were used to calculate bond valence (*s*) for each Na-O bond, these were summed to give V_i; these are tabulated in Table 12.

$$s = EXP\left(\frac{r_0 - r}{B}\right)$$

s=bond valence

r_0=calculated (ideal) bond length when the cation has a bond valence of exactly 1 (r_0= 1.803(3) for Na-O).

r=observed bond length.

B=empirical parameter (0.37)

Equation 1: The relationship between bond length (*r*) and bond valence (*s*).

$$V_i = \sum_j s_{ij} = \sum_j EXP\left(\frac{r_0 - r_{ij}}{B}\right)$$

V_i=oxidation sate of cation I (bond valence summation)

s_{ij}=bond valence of bond between cation I and anion j.

r_0=calculated (ideal) bond length when the cation has a bond valence of exactly 1 (r0= 1.803(3) for Na-O).

r_{ij}=observed bond length between cation i and anion j

B=empirical parameter (0.37)

Equation 2: The relationship between the oxidation state (*Vi*) of cation *i* and the valence of the bond between cation *i* and anion *j* (s_{ij}).

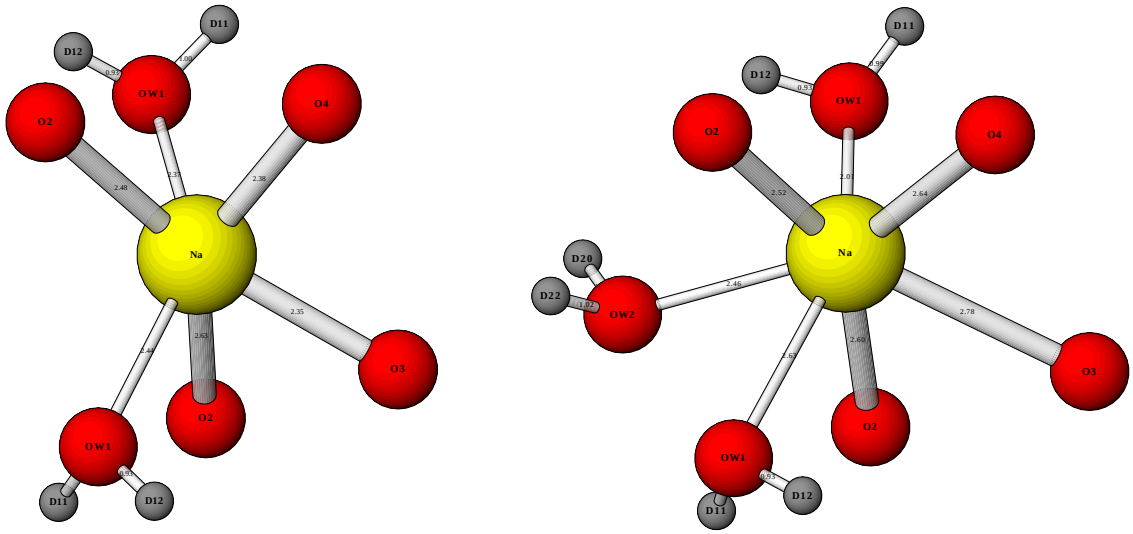

a) b)

Figure 27: Sodium coordination environment in orthorhombic gallosilicate natrolite at a) ambient pressure and b) post superhydration.

Table 12: Bond valance calculations of Na-O bonds at 0-2.26 GPa for orthorhombic gallosilicate natrolite. *r*=observed bond length, *s*=bond valence and *Vi*=bond valence summation (oxidation state of sodium).

		Pressure/GPa				
		0	0.22	0.74	1.83	2.26
NA_O2	*r* (Å)	2.477(8)	2.452(32)	2.75(4)	2.52(5)	2.63(5)
	s	0.1618(49)	0.173(15)	0.0773(88)	0.144(20)	0.107(15)
NA_O2	*r* (Å)	2.630(9)	2.559(33)	2.79(4)	2.60(4)	2.48(5)
	s	0.1070(35)	0.130(12)	0.0694(79)	0.116(13)	0.160(23)
NA_O3	*r* (Å)	2.351(8)	2.506(32)	2.49(4)	2.78(4)	2.57(5)
	s	0.2274(69)	0.150(14)	0.156(18)	0.0713(81)	0.126(18)
NA_O4	*r* (Å)	2.376(8)	2.372(27)	2.50(4)	2.64(5)	2.62(6)
	s	0.2125(64)	0.215(16)	0.152(17)	0.104(15)	0.110(19)
NA_OW1	*r* (Å)	2.369(11)	2.049(27)	2.09(4)	2.01(5)	2.32(5)
	s	0.2166(84)	0.514(39)	0.460(53)	0.572(82)	0.247(36)
NA_OW1	*r* (Å)	2.438(10)	2.707(24)	2.90(4)	2.63(5)	2.58(6)
	s	0.1797(64)	0.0869(58)	0.0516(59)	0.107(16)	0.123(22)
NA_OW2	*r* (Å)				2.46(5)	2.59(5)
	s				0.169(26)	0.119(17)
V_i		1.105(37)	1.27(10)	0.97(11)	1.28(18)	0.99(15)

Unlike the orthorhombic form, tetragonal gallosilicate natrolite shows a Na-OW2 coordination at ambient and over all high pressures. At ambient pressure, comparison of the calculated V_i (oxidation state) values for the sodium cation reflects this difference. A higher oxidation state is seen in the tetragonal verses the orthorhombic form (1.537(13) and 1.105(37) respectively), corresponding to a higher sodium cation coordination number. Figure 28 displays the sodium environment in tetragonal gallosilicate natrolite. Bond valence sums are tabulated in Table 13, calculated from Equation 2.

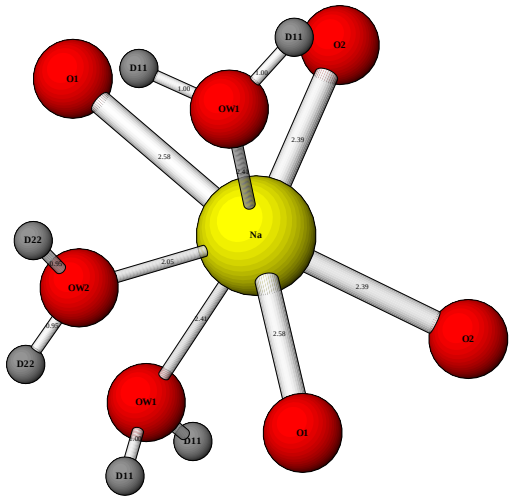

Figure 28: Sodium coordination environment in tetragonal gallosilicate natrolite

Table 13: Bond valance calculations of Na-O bonds at 0-2.3 GPa for tetragonal gallosilicate natrolite.

***r*=observed bond length, *s*=bond valence and *Vi*=bond valence summation (oxidation state of sodium).**

		Pressure/GPa				
		0	0.14	0.88	1.88	2.3
NA_O1 (x2)	*r* (Å)	2.58070(11)	2.593(16)	2.781(20)	2.595(17)	2.548(18)
	s	0.1222(10)	0.1182(62)	0.0711(46)	0.1176(46)	0.1335(78)
NA_O2 (x2)	*r* (Å)	2.38767(10)	2.447(34)	2.69(4)	2.60(4)	2.69(4)
	s	0.2059(17)	0.175(18)	0.090(11)	0.116(14)	0.090(11)
NA_OW1 (x2)	*r* (Å)	2.41122(11)	2.509(30)	2.727(33)	2.436(26)	2.403(23)
	s	0.1932(16)	0.148(14)	0.0823(84)	0.181(15)	0.198(14)
NA_OW2	*r* (Å)	2.06385(9)	2.04(8)	2.27(6)	2.44(6)	2.38(6)
	s	0.4941(41)	0.53(13)	0.283(52)	0.179(33)	0.210(39)
V_i		1.537(13)	1.41(21)	0.77(10)	1.01(10)	1.05(11)

4.4 Equation of State

The pressure and volume data obtained from the compression of superhydrated Ga-NAT (tetragonal and orthorhombic), can be used to fit an equation of state. From this the bulk modulus and an extrapolated 'V_0' can be obtained. This is particularly valuable as a value for V_0 of the superhydrated phase would not be possible to collect experimentally due to the reversibility of the pressure-induced hydration step. This was done using EoSFIT version 5.2.[9] A Murnaghan equation of state was used where V_0 and K_0 were treated as variables with K' fixed at 4. Other methods were tried including a 2nd order Birch-Murnaghan equation of state (which gave a similar result, but is mathematically more complex) and attempts to refine K' in a Murnaghan equation gave ill fitting results.

For superhydrated orthorhombic Ga-NAT (Figure 29), the refined V_0 value was 2389(4) Å^3. This is a difference of 79.62 Å^3, 3.45% larger than that of the normal, ambient condition phase (as collected experimentally). This is similar, but a little larger, than the refined value given in a report by Lee et al.[10] of 2365.(4) Å^3, 58 Å^3 larger than the normal state. For the first time, an equation of state has been fitted to superhydrated tetragonal Ga-NAT (Figure 30). The refined V_0 value was 1258(15) Å^3. This is a huge difference of 94.65Å^3, 8.13% larger than that of the normal, ambient phase. The difference in V_0 values between the two phases (ambient and superhydrated), is an estimation of the extra space needed to incorporate OW2 water into the pores. The increase in V_0 for tetragonal Ga-NAT is much greater than that observed for the orthorhombic gallosilicate analogue, as the tetragonal framework in more open and flexible. Tetragonal Ga-NAT undergoes a greater amount of cell expansion during PIH, although no more water is present.[*] This is reflected in the bulk moduli of the two forms. tetragonal Ga-NAT shows much greater compressibility (due to greater void volume, as evidenced by pore dimensions), than orthorhombic Ga-NAT. This is represented by the lower bulk modulus value 23(3) GPa, verses 49(3) GPa for orthorhombic Ga-NAT.

[*] A Fourier search was performed upon the tetragonal Ga-NAT neutron diffraction data, in order to locate any other possible water sites within the framework of the superhydrated form. No chemically sensible sites were found.

The trend in framework flexibility can be demonstrated by comparing the bulk moduli of Al-NAT, orthorhombic Ga-NAT and tetragonal Ga-NAT (53(1), 49(3) and 23(3) respectively).[5,10] The aluminosilicate has a higher bulk modulus than both the gallosilicates, indicating that the framework is less compressible. Upon Al/Ga substitution the framework becomes more open and flexible so the bulk moduli are lower. Similarly, a change in the T atom ordering changes the bulk modulus. Disorder across the T atom sites (tetragonal Ga-NAT), increases framework flexibility and therefore gives a lower bulk modulus.

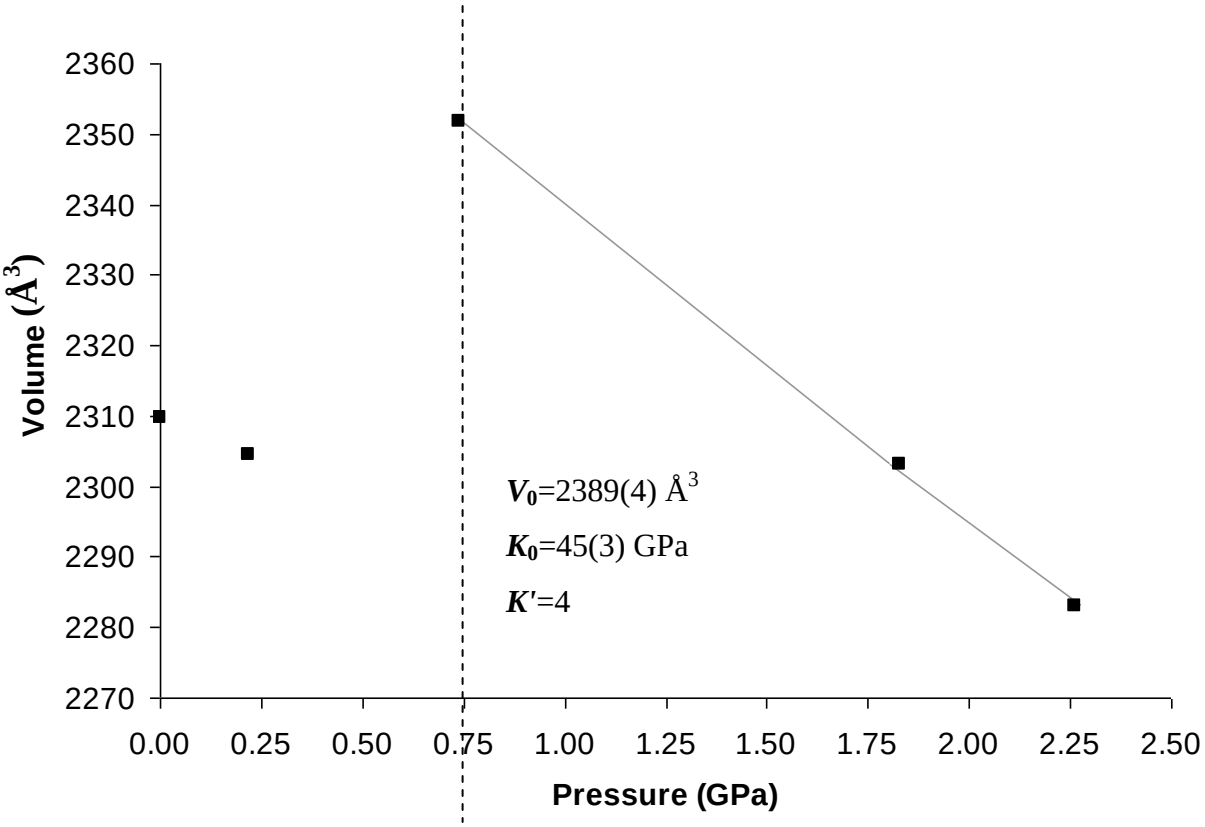

Figure 29: Pressure dependence of the unit cell volume of orthorhombic Ga-NAT and the equation of state fit (solid grey line), for the high pressure superhydrated form. The dashed black line indicates the transition to the expanded/superhydrated form.

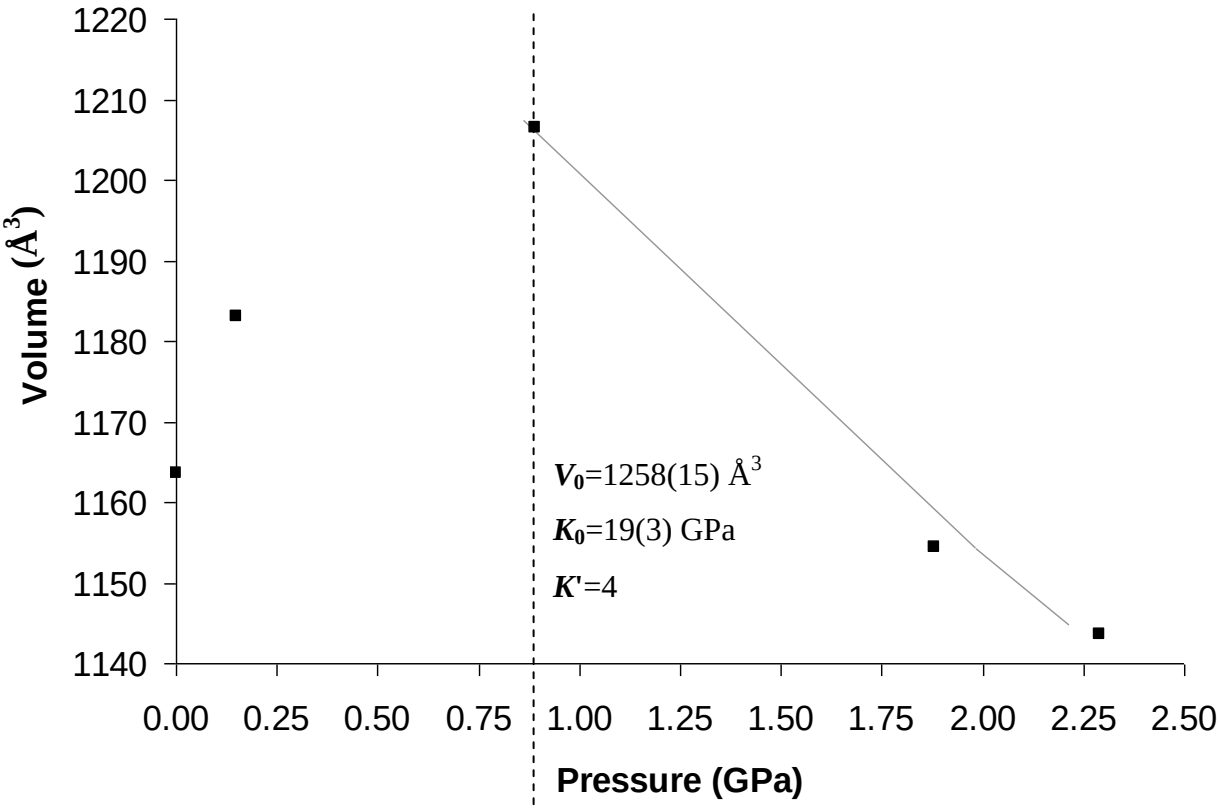

Figure 30: Pressure dependence of the unit cell volume of tetragonal Ga-NAT and the equation of state fit (solid grey line), for the high pressure superhydrated form. The dashed black line indicates the transition to the expanded/superhydrated form.

4.5 Conclusion

In this chapter a high pressure neutron diffraction study has elucidated the hydrogen positioning and bonding within the pores of orthorhombic and tetragonal gallosilicate natrolite over a number of pressures. The hydrogen bonding network revealed a very different pattern to that expected. A report by Lee *et. al.*[5] measured the distances between the water oxygens and postulated that the intrapore waters were hydrogen bonded to each other forming water nanotubes which extend through the pore along the *c* axis. The neutron diffraction study carried out in this thesis shows that the water molecules form extensive hydrogen bonds with framework oxygens and some direct hydrogen bonds between water molecules. However, these direct hydrogen bonds occur only across the channels and not within them, and so do not show the proposed water nanotube formation postulated by Lee *et. al*.[5]

A number of differences between the orthorhombic and the tetragonal gallosilicate natrolites have been identified from the data collected in this study. The most significant differences in the tetragonal verses the orthorhombic form include: a greater cell volume expansion; earlier onset of pressure-induced superhydration; larger pore dimensions and more flexible T-O-T bonds; a sodium coordination number of 7 over all pressures (orthorhombic has a sodium coordination number of 6 prior to superhydration) as evidenced by bond valence calculations; lower bulk modulus values for the superhydrated phase. These differences demonstrate the increased framework flexibility of the tetragonal verses the orthorhombic form due to disordering of the T atom sites.

[1] John Loveday, University of Edinburgh, School of Physics and Astronomy. http://www2.ph.ed.ac.uk/~jsl/

[2] Artioli G.; Smith J. V.; Kvick Å. 'Neutron diffraction study of natrolite, $Na_2Al_2Si_3O_{10}.2H_2O$, at 20 K' **1984** *Acta. Cryst. C40.* 1658-1662.

[3] Colligan M.; Lee Y.; Vogt T.; Celestian A. J.; Parise J. B.; Marshall W. B.; Hriljac J. A. 'High-pressure neutron diffraction study of superhydrated natrolite' **2005**. *J. Phys. Chem. B. 109.* 18223-18225.

[4] Lee Y.; Hriljac J. A.; Kim S. J.; Vogt T.; Hanson, J. C. 'Pressure-induced hydration at 0.6 GPa in a synthetic gallosilicate zeolite' **2003**. *J. Am. Chem. Soc. 125*. 6036-6037.

[5] Lee Y.; Hriljac J. A.; Kim S. J.; Vogt T.; Parise J. B.; Artioli G. 'Pressure-induced volume expansion of zeolites in the Natrolite family' **2002**. *J. Am. Chem. Soc. 124*. 5466-5475.

[6] Lee Y.; Hriljac J. A.; Parise J. B.; Vogt T. 'Pressure-induced hydration in zeolite tetranatrolite' **2006**. *J. Am. Chem. Soc. 91*. 247-251.

[7] Moroz N. K.; Kholopov E. V.; Belitsky I. A.; Fursenko B. A. 'Pressure-enhanced molecular self-diffusion in microporous solids' **2001.** *Microporous and Mesoporous Materials. 42*. 113-119.

[8] Brown I. D.; Altermatt D. 'Bond-valence parameters obtained from a systematic analysis of the inorganic crystal structure database' **1985** *Acta. Cryst. B41* 244-247.

[9] Angel R. J. 'Equations of State, High-Pressure, High-Temperature Crystal Chemistry' **2000**. *Reviews in Minerology and Geochemistry. 41*.

[10] Lee Y.; Hriljac J. A.; Parise J. B.; Artioli G.; Vogt T. 'First structural investigation of a super-hydrated zeolite' **2001**. *J. Am. Chem. Soc. 123*: 12732-12733.